Laser Cleaning of Slotted Components

A thesis submitted to

The University of Manchester

For the degree of

Doctor of Philosophy (PhD)

in the Faculty of Engineering and Physical Sciences

2012

Liyang Yue

School of Mechanical, Aerospace and Civil Engineering

Table of Contents

Table of Contents **2**

List of Figures and Tables **7**

List of Publications **11**

Abstract **12**

Declaration **13**

Copyright statement **14**

Acknowledgements **15**

Chapter 1. Introduction **16**

1.1 Research motivation and rationale 16

1.2 Aim and objectives 17

1.2.1 Aim 17

1.2.2 Objectives 18

1.3 Thesis outline 19

Chapter 2. Literature review **21**

2.1 Introduction 21

2.2 Laser processing and industrial application 21

2.3 Lasers used for cleaning 22

2.3.1 Carbon dioxide laser 24

2.3.2 Nd: YAG Laser 26

2.3.3 KrF excimer Laser 28

2.4 History and development of laser cleaning 30

2.5 Mechanism of laser cleaning 33

2.5.1 Ablation 34

2.5.2 Spallation 37

2.5.3 Transient surface heating 37

2.5.4 Evaporation pressure 38

2.5.5 Photon pressure 38

2.5.6 Dry laser cleaning 38

2.5.7 Steam laser cleaning 40

2.6 Cleaning threshold 43

2.7 Adhesion forces 43

2.7.1 Van der Waals force 44

2.7.2 Capillary and liquid bridge force 45

2.7.3 Electrostatic Force 47

2.7.4 Dominant Adhesion Forces 48

2.8 Cleaning force 49

2.8.1 Dry laser cleaning forces 49

2.8.2 Steam laser cleaning force 49

2.9 Plasma shielding effect 52

2.10 Laser shock cleaning 52

2.11 Simulation methods 54

2.11.1 Finite elements method (FEM) 54

2.11.2 Finite difference method (FDM) 56

2.11.3 Finite integration technique (FIT) 56

2.11.4 Computational fluid dynamics (CFD) 58

2.11.5 Modelling boundary conditions 59

2.12 Modelling of laser cleaning 61

2.13 Slot application 62

2.14 Conclusions 65

Chapter 3. Methodology and equipments 68

3.1 Introduction 68

3.2 Materials 68

3.2.1 Silicon wafer 68

3.2.2 Fused silica particle 71

3.2.3 Titanium alloy (Ti6Al4V) and alpha case 73

3.3 Laser systems 75

3.3.1 KrF Excimer laser......75

3.3.2 Nanosecond laser......76

3.3.3 Femtosecond laser......77

3.3.4 Pulsed CO_2 laser......78

3.4 Characterisation equipments......79

3.4.1 Scanning Electron Microscope (SEM)......79

3.4.2 Optical microscope......80

3.4.3 White light interferometer......81

3.4.4 Atomic force microscope......82

3.4.5 Spectrophotometer......83

3.5 Commercial software......84

3.5.1 ANSYS......84

3.5.2 CST 2011......85

3.6 Experimental procedures......86

3.6.1 Beam size measurement......86

3.6.2 Energy measurement......87

3.6.3 Evaluation of cleaning quality and rate......87

3.7 Summary......88

Chapter 4. Laser cleaning of alpha case from Titanium alloy......90

4.1 Introduction......91

4.2 Experimental Procedure......91

4.3 Results......94

4.3.1 Ablation rate......94

4.3.2 Morphology......96

4.4. Discussion......100

4.4.1 Cracks and surface finish......100

4.4.2 Prediction of thickness of alpha case layer......104

4.5 Conclusions......107

Chapter 5. Laser cleaning of tiny particles on slot sidewalls......108

5.1 Introduction......109

5.2 Experimental Procedure 109
5.3 Simulation Process 113
5.3.1 Model description 113
5.3.2 Modelling geometry and materials 113
5.3.3 Laser Source: temporal and spatial profile 114
5.3.4 Boundary conditions 115
5.4 Results 116
5.4.1 Cleaning thresholds 116
5.4.2 Cleaning efficiencies 117
5.4.3 Simulation results 119
5.5 Discussion 121
5.5.1 Effect of slot widths and sidewall 121
5.5.2 Cleaning force 124
5.5.3 Prediction of cleaning thresholds 126
5.6 Conclusions 127
Chapter 6. Multiphysics modelling of dry laser cleaning of micro-slots with particle contaminants 128
6.1 Introduction 129
6.2 Simulation Process 129
6.2.1 Modelling geometry and materials 129
6.2.2 Laser Source: temporal and spatial profile 131
6.2.3 Boundary conditions 132
6.3 Results and Discussion 132
6.3.1 Electromagnetic modelling: intensity fields in micro-slots 132
6.3.2 Electromagnetic modelling: energy flow visualization 139
6.3.3 Electromagnetic to thermal modelling: temperature fields 142
6.3.4 Thermal to mechanical modelling: cleaning thresholds 145
6.4. Conclusions 148
Chapter 7. Modelling of laser cleaning of tapered micro-slots with different temporal pulses 150

7.1 Introduction 151
7.2 Numerical simulation 152
7.2.1 Boundary conditions 152
7.2.2 Modelling geometry and reflectivity 153
7.2.3 Temporal pulse shapes 154
7.2.4 Material properties 155
7.2.5 Mesh element 156
7.2.6 The plasma shielding effect 156
7.3 Results and discussion 157
7.3.1 Mesh size 157
7.3.2 Flat surface model 158
7.3.3 Tapered micro-slot modelling 160
7.4 Conclusions 167
Chapter 8. Conclusions and recommendations for the future **168**
8.1 Conclusions 168
8.1.1 Technical achievement 168
8.1.2 Scientific achievement 169
8.2 Future work 170
8.2.1 Technical exploration 170
8.2.2 Scientific exploration 171
References **172**

Word Count: 36,792

List of Figures and Tables

Figure 2.1 Wavelengths of current laser types……………………….……………….…..**23**

Figure 2.2 The vibration modes of CO_2 molecules (a) symmetric vibration (b) bending vibration (c) asymmetric vibration…………………………………………**25**

Figure 2.3 Nd:YAG rod inside laser…………………………………………………**28**

Figure 2.4 (a) silicon membrane stencil mask contaminated with Al_2O_3-spheres (diameter from 0.3 to 1.5 μm). (b) The same silicon membrane stencil mask after four pulses of KrF excimer laser irradiation…………………………………...............**33**

Figure 2.5 Schematic of the one-dimensional heating model………………………**34**

Figure 2.6 Pulse intensity versus time showing basis for self-limiting effect……..…**36**

Figure 2.7 Mechanisms involved in dry laser cleaning for the removal of small particles from silicon wafer surfaces………………………………………………...**40**

Figure 2.8 Mechanism involved in steam laser cleaning for the removal of small particles from silicon wafer surfaces…………………………………………………**42**

Figure 2.9 Liquid bridge geometry model…………………………………………...**46**

Figure 2.10 Schematic for laser shock cleaning……………………………….......**53**

Figure 2.11 The schematic diagram of elements and boundaries……………………**55**

Figure 2.12 The silicon wafer after fabrication……………………………….......**63**

Figure 2.13 The micro-fabricated surface for anti-growth of protein………………**64**

Figure 2.14 The slots on the water cooling transfer part………………………........**65**

Table 2.1 Milestone of laser cleaning technique……………………………………..**66**

Figure 3.1 The silicon wafer used in this study……………………………………...**71**

Figure 3.2 Fused silica particle used in this study (a) powder (b) SEM picture for the particle with 1.5 μm diameter…………………………………………………………..**73**

Figure 3.3 Ti6Al4V alloy sheets……………………………………………………**75**

Figure 3.4 GSI - Lumonic IPEX800 KrF excimer laser at LPRC…………………..**76**

Figure 3.5 532 nm Laserval Violino laser at LPRC………………………………....**77**

Figure 3.6 Ti Sapphire femto second laser at PSI……………………………….......**78**

Figure 3.7 GSI Lumonics IMPACT 3000 pulsed CO_2 laser……………………........**78**

Figure 3.8 Hitachi High Technologies SEM at PSI…………………………………**80**

Figure 3.9 Optical microscope (Polyvar) at LPRC….………………………………**81**

Figure 3.10 White light interferometer WYKO NT1100 at LPRC…………………**82**

Figure 3.11 Veeco AFM at PSI……………………………………………………**83**

Figure 3.12 Photo spectrometer Ocean optics SD2000……………………….......**83**

Figure 4.1 (a) Ablation rate of alpha case Titanium and Ti6Al4V alloy at various laser fluences (b) Cross sections of the alpha case samples after 900 pulses of laser radiation with a fluence of 6.1 J/cm^2……………………………………...............**95**

Figure 4.2 (a) Structural schematic of cross section of sample after laser irradiation (b) Morphologies of ablation surface of alpha case at multiple depths (1-6)…………………………………………………………………………………...**97**

Figure 4.3 Morphologies of ablation surface of Ti6Al4V alloy at depths (a) 4 μm (b) 70 μm..…………………………………………………………..…………**98**

Figure 4.4 (a) Surface roughness (R_a, R_q) of ablated surface in the alpha case layer as a function of the ablation depth. (b) 3D micrographs of ablation surface captured by white light interferometer at depth f..…………………………...............................**99**

Figure 4.5 Relationship between the hardness of alpha case, crack widths and densities against depth……………………….…………………….......................**100**

Table 4.1 The values of constants…………………………………………………..**106**

Figure 4.6 Function curves of thickness of alpha case layer………………………**106**

Figure 5.1 (a) The schematic of experiment setup (b) The vertical view schematic of silicon slot (c) The outline for the cleaning area on the side wall of 3.5 mm wide slot………………………………………………………………………….……..**111**

Figure 5.2 The geometric sketch of CST modelling…………………….…….....**114**

Table 5.1 Optical and thermal properties of fused silica and silicon……….........**114**

Figure 5.3 (a) The experimental and simulated cleaning thresholds for multiple slot widths. The surface morphologies at the edge of the cleaned area for 60 mJ laser on 6 mm wide slot sidewall with the magnification of (b) 250x and (c)

500x …………………………………………………………………………………...117

Figure 5.4 (a) Cleaning efficiencies of multiple laser pulse numbers for 60 mJ output energy on the side wall of 4, 5 and 6 mm wide slots. (b) The surface morphology of the side wall layered particles for 5 mm wide slot. (c-f) The surface morphologies of the side wall after 5, 10, 20 and 30 pulses……………………………………….**119**

Figure 5.5 (a) Simulated electromagnetic distribution of single particle sitting on the silicon sidewall (b) The temporal temperature rises for the 4, 5 and 6 mm wide slots at the contacting point between the particle and side wall substrate…………………..**120**

Figure 5.6 (a) Vertical view schematic of cleaning front end for different slot widths (b) The experimental effect of falling phenomenon (slot widths 3.5 and 4 mm, paint background)……………………………………………………………......................**122**

Figure 6.1 Geometric sketches of single (a), double (b) and triple (c) particle layouts for 1 μm diameter particle…………………………………………………….….**130**

Table 6.1 Optical and thermal properties of the substrate and the particles……….. **130**

Figure 6.2 (a) Peak intensity on substrate surface beneath 1-um-diameter particles as a function of slot width. (b-g) Corresponding 2D cross-sectional views of the maximum intensity fields in XZ-plane (b,d,f) and XY-plane (c,e,g) for single (P1), double (P2) and triple (P3) layered particles…………………...............................**134**

Figure 6.3 (a) Peak intensity on the substrate surface beneath the 2-um-diameter particles as a function of slot width. (b-g) Corresponding to the 2D cross-sectional views of the maximum intensity fields in XZ-plane (b,d,f) and XY-plane (c,e,g) for single (P1), double (P2) and triple (P3) layered particles…………………………..**138**

Figure 6.4 The energy flow field lines of single 1μm diameter particle in slot (a) at slot width = 1 μm (b) slot width = 1.8 μm (c) slot width = 3.2 μm. The schematic of 3D vortex coupling energy into different planes is shown as inset in (a)…………………………………………………………………………………...**142**

Figure 6.5 (a) Temporal temperature distribution of the substrate surface under single, double and triple particles at optimized slot widths (b), corresponding to spatial temperature distribution of substrate surface at t=10 ns…………………………....**144**

Table 6.2 Cleaning and damage threshold for the 1-um-diameter glass particles in gold micro-slot……………………………………………………………………...**148**

Table 6.3 Cleaning and damage thresholds for the 2-um-diameter glass particles in gold micro-slot……………………………………………………………………...**148**

Figure 7.1 (a) The dimension of micro-slot structure (b) Temporal variation of the intensity for rectangular and Gaussian pulses………………………………………**155**

Table 7.1 Material properties of crystalline silicon………………………………...**156**

Table 7.2 Material properties of oil film……………………………………………**156**

Figure 7.2 (a) Temperature profiles calculated by the analytical solution and numerical solution using FE modelling with multiple mesh sizes (b) Temporal temperature profiles on a flat surface irradiated by the rectangular and Gaussian pulses with the same fluence. Solid and dot lines are calculated by analytical and numerical solution respectively…………………………………………………...**160**

Figure 7.3 Temporal heating profiles of at top surface (L1), side wall (L2) and bottom (L3) with multiple laser fluence for (1-3) rectangular and (4-6) Gaussian pulses. The 3D temperature distribution of 40 mJ/cm^2 for Gaussian shape at 10 ns is illustrated in (7)……………………………………………………...………………………**162**

Figure 7.4 The cleaning depths and temperature distributions on the cross section of oil film at top surface (L1), side wall (L2) and bottom (L3) for (1-3) rectangular and (4-6) Gaussian pulses……………………………………………………….…...**164**

Figure 7.5 The Cleaning depths of the rectangular and Gaussian pulses as a function of laser fluence (20 mJ/cm^2, 30 mJ/cm^2, 40 mJ/cm^2, 50 mJ/cm^2, 60 mJ/cm^2, 70 mJ/cm^2, 80 mJ/cm^2, and 90 mJ/cm^2) at three locations (L1, L2 and L3) …………………………………………………………………………………**165**

Table 7.3 The cleaning thresholds on micro-slot model……………………………**166**

List of Publications

1. Liyang Yue, Zengbo Wang, Wei Guo and Lin Li, *'Axial laser beam cleaning of tiny particles on narrow slot sidewalls'*, Journal of Physics D: Applied Physics, 45 (2012) 365106

2. Liyang Yue, Zengbo Wang and Lin Li, *'Multiphysics modelling and simulation of dry laser cleaning of micro-slots with particle contaminants'*, Journal of Physics D: Applied Physics, 45 (2012) 135401

3. Liyang Yue, Zengbo Wang and Lin Li, *'Material morphological characteristics in laser ablation of alpha case from Titanium alloy'*, Applied Surface Science, 258 (2012) 8065-8071

4. Liyang Yue, Zengbo Wang and Lin Li, *'Modeling and simulation of laser cleaning of tapered micro-slots with different temporal pulses'*, Optics and Laser Technology, 45 (2012) 533-539

5. Liyang Yue, Zengbo Wang, Wei Guo and Lin Li, *'Laser cleaning of vertical slot'*, (submitted), ILAS Conference, Nottingham

Abstract

Laser cleaning is a non contact, highly controllable process for the removal of contaminants from a surface with minimum or no damage to the substrate material. Laser cleaning has been applied mainly on flat and curved surfaces. Little is known on the phenomena and feasibility of laser cleaning of slotted structures. Slots are common structures in engineering, and can be found in many components. In this PhD work, the feasibility of laser cleaning of alpha case on flat titanium alloy surfaces was initially explored, and then an investigation was made on the use of a pulsed laser for the cleaning of micro to macro slots in silicon and metallic materials. The effects of laser processing parameters on the contaminant removal from these slots were experimentally studied. Laser cleaning thresholds and cleanliness was examined. Meanwhile, finite element modelling (FEM) and time domain finite difference modelling techniques were used to simulate the processes involved to aid the understanding of the technique for process optimisation. The experiments were undertaken to verify if such models are able to accurately predict the cleaning thresholds. The surface and sub-surface characteristics before and after laser cleaning were examined using optical microscopy and scanning electron microscopy (SEM). It has been shown that the slot structure and its material properties were not damaged or changed by laser cleaning process.

A novel contribution is that surface morphology after the laser ablation could be used as a diagnostic method to indentify the presence of alpha case and measure its thickness due to the specific characteristics of the surface roughness and generated cracks on the ablated surface after laser irradiation. Besides, it has been found that an axial beam which propagates into the narrow slots can successfully clean the tiny particles on the slot sidewalls whose width ranges from 3.5 mm to 13mm. These phenomena had never been reported before.

Declaration

I hereby declare that no portion of the work referred to in the thesis has been submitted in support of an application for another degree or qualification of this or any other university or other institute of learning.

Copyright statement

- The author of this Thesis (including any appendices and/or schedules to this thesis) owns certain copyright or related rights in it (the "Copyright") and he has given The University of Manchester certain rights to use such Copyright, including for administrative purposes.

- Copies of this thesis, either in full or in extracts and whether in hard or electronic copy, may be made **only** in accordance with the Copyright, Designs and Patents Act 1988 (as amended) and regulations issued under it or, where appropriate, in accordance with licensing agreements which the University has from time to time. This page must form part of any such copies made.

- The ownership of certain Copyright, patents, designs, trade marks and other intellectual property (the "Intellectual Property") and any reproductions of copyright works in the thesis, for example graphs and tables ("Reproductions"), which may be described in this thesis, may not be owned by the author and may be owned by third parties. Such Intellectual Property and Reproductions cannot and must not be made available for use without the prior written permission of the owner(s) of the relevant Intellectual Property and/or Reproductions.

- Further information on the conditions under which disclosure, publication and commercialisation of this thesis, the Copyright and any Intellectual Property and/or Reproductions described in it may take place is available in the university IP Policy (see http://www.campus.manchester.ac.uk/medialibrary/policies/intellectual-property.pdf), in any relevant Thesis restriction declarations deposited in the University Library, The University Library's regulations (see http://www.manchester.ac.uk/library/aboutus/regulations) and in The university's policy on presentation of Theses.

Acknowledgements

I would like to acknowledge my supervisors, Professor Lin Li and Dr Zengbo Wang, who supervised all my work, and provided guidance on my ideas from the outset of the project.

The research has greatly benefited from discussions with all my colleagues in the Laser Processing Research Centre (LPRC), University of Manchester, past and present. I am deeply indebted to the selfless help of my senior colleagues Dr Ashfaq Khan, Dr Ana Pena, Dr Jiao Jiao, Dr Sundar Marimuthu, Dr Yinzhou Yan, Dr Kursad Sezer, and especially Dr Wei Guo.

The laboratory experimental officer, Dr David Whitehead, helped set up complicated experiments and maintenance lasers – this is very important to every student. Dr Zhu Liu offered me the right to use the resource in the Corrosion and Protection Centre (CPC). Meanwhile, the other PhD students in LPRC, Seoungjun Lee, Wei Guo, Juansethi and Ahmed Mosallamy, also provided moral support where necessary. I am very glad to have shared three years with them in Manchester.

Finally, I am thankful to my wife, Jing Xie, whom I married while writing this thesis. She faithfully supports me and understands my personality. She is my gift from god. This thesis is a proof of our love.

Chapter 1. Introduction

1.1 Research motivation and rationale

The term ‘laser’ is an acronym for ‘light amplification by stimulated emission of radiation’ which refers to a method for producing a coherent electromagnetic radiation by the stimulated emission process. From the day that the laser was invented, multiple applications were found by industry for this novel and powerful energy source. Lasers could provide high intensity photon bursts of short pulse durations in a highly directional beam, which inspires many related surface techniques [1]. Modern manufacturing processes for precision devices in microelectronics or data storage industries continue to demand higher resolution, smaller size, low cost and environmentally friendly [2]. There is an ever increasing requirement of development of better techniques to remove particles or other contaminants from a critical surface.

Under these industrial circumstances, the contaminants with submicron size can adhere to a surface with a relatively strong force which is much larger than its gravity [3]. For this reason, a cleaning technique for tiny contaminants should be developed and be safe for the surface so as not to cause surface damage or recontamination onto the surface. Although wet chemical cleaning has been widely applied, they often leave chemical residuals on the cleaned surfaces and many of them are not environmentally friendly. The possibility of using a non-physical contact photon beam to achieve the desired cleaning on a critical surface has become a subject of great interest.

Slots as a common structure can be found on hard discs, DVDs and other electronic devices [4]. Traditionally these structures are cleaned by chemical and ultrasonic cleaning methods relying on a liquid medium. For removal of chemical solutions, the corrosion on material surfaces cannot be ignored, and waste disposal would significantly increase the processing cost for industry. Besides, with ultrasonic cleaning, it is possible to generate and enlarge the tiny cracks on the surface due to strong liquid shock, which could influence the integrity of the substrate.

Therefore, laser cleaning as a potential technique that could be applied on the slot structures and replace these traditionally mechanical and chemical cleaning methods, although this still faces many challenges. Slot sidewalls are relatively difficult to absorb enough laser energy to form a cleaning force without damaging the bottom of the slot, since the sidewalls are parallel to the laser irradiation direction. In this study, several methods and related models are demonstrated to overcome these difficulties.

1.2 Aim and objectives

1.2.1 Aim

The aim of this project is to understand the mechanism of laser cleaning of slots and the related interactions between contaminants and surfaces, by both experiments and theoretical modelling. Such research activities are intended to lead to the establishment of corresponding processing window.

1.2.2 Objectives

The objectives of the research to achieve the aim are:

- To develop a novel method for cleaning the sidewalls of slotted component. It is well known that the sidewalls are parallel with the direction of laser beam propagation, which means that sidewalls absorb little laser energy, while the bottom of the slot may face much higher proportion of laser beam radiation. Hence, design of experiments could be very important to examine the cleaning and damage thresholds on both the side walls and the bottom of the slots.
- To investigate basic phenomena in material interactions in the cleaning process in particular to focus on alpha case removed and angular beam irradiation.
- To investigate the behaviour of tiny particle contaminants in the laser cleaning of slots. Tiny transparent particles presented on the surface of slots, could act as lenses to focus the laser beam, thus they either enhance the cleaning efficiency or cause damage to the surface depending on the focused laser power density. Such phenomenon will be studied by both theoretical modelling and experiments.
- To predict the cleaning effectiveness through theoretical modelling. Finite element method (FEM) and finite integral technique (FIT) have been used for the modelling. These were used to predict the magnitude of the cleaning forces on the substrate surface.

1.3 Thesis outline

An overview of laser cleaning techniques is given in chapter 2. The history and mechanism of laser cleaning are presented and discussed. The principles of typical lasers usually used for cleaning are reviewed. In addition, the previous approach in modelling laser beam interaction with material is included in this chapter. The main purpose of this literature review is to identify state of the art in laser cleaning and knowledge gaps existed.

Chapter 3 describes the materials, equipment, commercial software tools and experimental procedures used in this project. The operating principles of the analytical equipment used in the project are given.

The body of research performed is presented in four parts. The mechanism of the cleaning of alpha case on a flat surface and related morphological characteristics is included in chapter 4. The work shows that such pulsed lasers could provide higher material removal rate and smaller surface roughness on the processing surface compared with the mechanical processing.

Chapter 5 details an attempt to use an axial laser beam to clean tiny particles on narrow slot sidewalls. This is a novel concept compared with the traditional laser cleaning technique and is reported for the first time. The slot structure, especially the sidewalls, could be successfully cleaned using this method. Corresponding

experimental cleaning thresholds and efficiencies for multiple slot widths are presented, and supported by an electromagnetic-thermal-mechanical coupled multiphysics model. The cleaning thresholds were found generally to increase with the growth of slot widths.

Chapter 6 describes a multiphysics model including electromagnetic, thermal and mechanical fields that was established to simulate the dry laser cleaning of particles trapped in a micro-slot. It was found that the magnitudes of field intensity on the substrate in a certain range of slot width could be elevated by about 25% for 1 and 2 μm diameter particles, and their energy distributions on the slot bottom were influenced by particle layouts.

Chapter 7 reports the modelling and simulation of laser cleaning of tapered micro-slots with different temporal pulses (rectangular and Gaussian pulses). The multiple cleaning effects in micro-slots with different temporal pulses were investigated. The micro-slot model indicates that the rectangular pulse has higher cleaning efficiency compared with the Gaussian pulses, and the cleaning depth at side walls is lower than the other locations using the same laser parameters.

Finally, the conclusions of this research and future plans are given in chapter 8. The conclusion is divided into two parts, technical and scientific contributions and discoveries.

Chapter 2. Literature review

2.1 Introduction

This chapter reviews the history and mechanism of laser cleaning techniques. The laser operating principle and modelling of laser beam interaction with material are also included. The review is intended to identify the state of the art in laser cleaning, the knowledge gap existed and the potential challenges in cleaning slots.

2.2 Laser processing and industrial applications

Lasers play a major part in the processing of the materials in the engineering and manufacturing fields. The number of laser processing techniques is sharply increasing over the last 20 years. With this growing trend lasers have become an important processing tool, and more and more unique characteristics and applications have been discovered. The categories of industrial application can be classified into: laser cutting, laser welding, laser drilling, laser marking/engraving, laser surface treatment, additive manufacturing, micro/nano fabrication and laser cleaning [5]. Meanwhile, some related technologies have also developed quickly in industry, such as laser automation and in-process monitoring [6].

Generally, the market for lasers in material processing has been a growth area for several years and is expected to continue at 10-20% per year for some time yet, and the common laser industrial applications concentrate on the cutting and welding fields which take 30% of market revenue [1]. High power continuous wave (CW) lasers are

typically for these applications. The laser has many advantages in these fields compared with the other alternative techniques, such as punch, plasma, nibbling and abrasive fluid jet, which mainly reflect the superior material processing rate, edge quality, kerf width, flexibility and tool wear with a laser [7]. Nevertheless, the laser surface processing techniques, such as cleaning, ablation, and patterning, always demand higher peak power to process the material. For this reason, pulsed lasers have been selected for these applications due to their higher peak powers compared with CW lasers. The high peak power of the laser delivered in short pulses allows the small portion of material that is above boiling point within the pulse duration to evaporate away from the substrate or the generation of a sudden cleaning force underneath the spherical contaminants [8].

2.3 Lasers used for cleaning

Many types of laser have been invented in last 50 years. Their unique characteristics were found and studied by previous researchers. These lasers can be classified by the wavelength of the light emission as shown in figure 2.1 [9]. Depending on the wavelengths four groups of laser, ultraviolet, visible, near-infrared and mid-infrared, are shown in figure 2.1. Several typical lasers used for the cleaning tasks are introduced in this section.

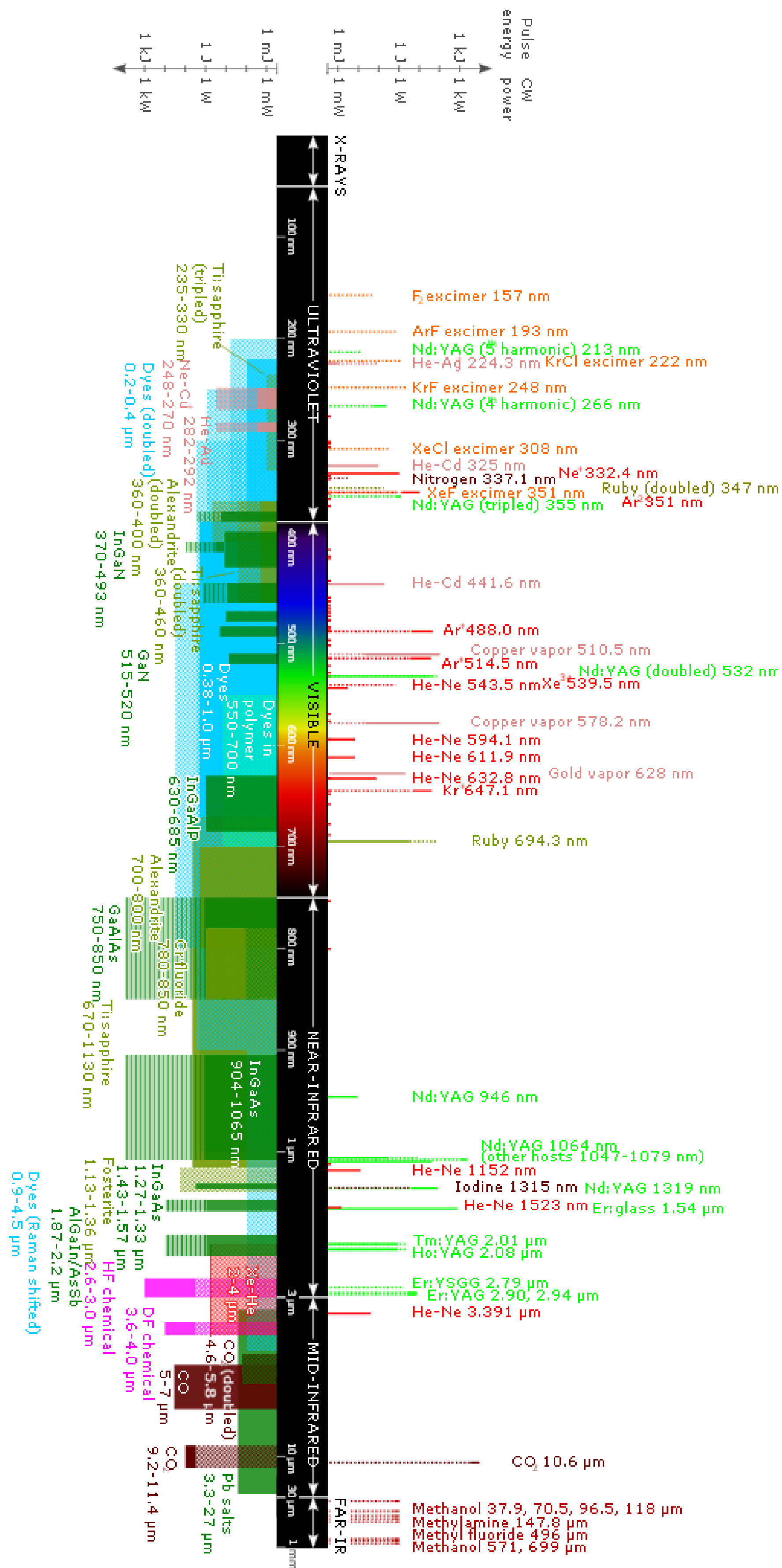

Figure 2.1 Wavelengths of current laser types [9]

2.3.1 Carbon dioxide laser

The carbon dioxide laser is a gas laser, in which an electric current is discharged through a gas mixture to produce coherent light [10,11]. The CO_2 laser is an important type and also one of the earliest gas lasers to be developed. It was invented by Dr. Patel of Bell Labs in 1964 [12]. Presently CO_2 lasers are among the highest power continuous wave (CW) lasers. The ratio of output power to pump power can be up to 15% [13]. The CO_2 laser produces a beam of infrared light with the wavelength ranges from 9.4 to10.6 µm.

The energy storage and interchange in a CO_2 gas has three basic forms, molecular translation, vibration and rotation [14]. In fact, carbon dioxide is a linear, symmetric molecule with the carbon atom balanced against the two oxygen atoms, O-C-O. Three characteristic vibrational modes can simultaneously exist in its molecule structure. The first one is named as symmetric mode, where the two oxygen atoms horizontally vibrate and compress or drag the carbon atom in the middle. The second one is bending mode, where the carbon atom moves out of the molecular axis, thus bending the molecule. The third one is asymmetric mode, where the two oxygen and carbon atoms oscillate against each other [15]. The schematic of these three vibrations is shown in figure 2.2.

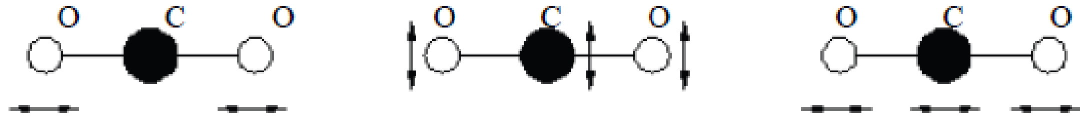

Figure 2.2 The vibration modes of CO_2 molecules (a) symmetric vibration (b) bending vibration (c) asymmetric vibration [15]

Each of these vibrating modes is quantised, and the particular vibrational state of the molecule is named by three integral numbers. The first number is the quantum level or excitation number of the symmetric mode. The second number is the excitation number of the bending mode, and the third number is the excitation number of the asymmetric mode. In addition to the energy levels of the pure modes mixed vibrational modes exist as well [16].

Normally nitrogen and helium are the other filling gases in addition to carbon dioxide in a CO_2 laser. In the process of stimulated emission, electron impact excites vibrational motion of the nitrogen which is metastable and stays for a long time. Corresponding collisional energy between the nitrogen and the carbon dioxide molecule causes asymmetric vibration of the carbon dioxide. The vibrational energy is converted into laser emissions by collisions with helium in the transition from asymmetric vibration to symmetric vibration of carbon dioxide molecule [14,15]. Helium is used to facilitate the heat removal during the thermal radiation process after the lasing action.

The CO_2 laser shows many advantages in laser cleaning. At first, its wavelength is suitable for the cleaning of multiple materials. It is well known that laser cleaning involves interactions between photons and the substrate, which depends on the absorptivity of the material to the laser beam and the penetrability of the laser [17]. These elements both are influenced by the wavelength of the laser. Therefore, the optimum wavelength of the laser for cleaning should be near the absorption peak of the material, which will improve the cleaning efficiency and quality [18]. The common metals used in industry, such as mild steel, stainless steel, titanium alloy, all can absorb mid-infrared light, but much less compared with lasers with shorter wavelengths. The CO_2 laser wavelength is best absorbed by ceramic and organic materials, which constitute most of the contaminants in practical industrial application. From the established literature, it is known that the laser cleaning of multiple materials were successfully performed by previous researchers by using CO_2 lasers [19-21].

2.3.2 Nd: YAG Laser

The full name of Nd:YAG is neodymium-doped yttrium aluminium garnet, $Nd:Y_3Al_5O_{12}$. It is a solid state crystal used as a lasing medium. The triply ionized neodymium, typically replaces yttrium in the crystal structure of the yttrium aluminium garnet (YAG), since the two ions have similar size [22,23]. Solid state lasers use ions suspended in a crystalline matrix to produce laser light. The ions or dopants provide the electrons for excitation, while the crystalline matrix propagates

the energy between ions. The main dopant in the laser medium is neodinium (Nd^{3+}) for Nd:YAG laser [23]. The first Nd:YAG laser was invented by Geusic et al. at Bell Laboratories in 1964 [24].

Nd:YAG lasers are typically pumped using a flashlamp or laser diodes. A krypton or xenon flashlamp is an electric glow discharge lamp designed to produce extremely intense, full-spectrum white light in short durations [25]. A laser diode is made up by a p-n junction and powered by injected electric current. Nd:YAG lasers typically emit light with wavelength of 1064 nm in the near-infrared zone [26]. However, they also have the transitions near 532, 940, 1120, 1320, and 1440 nm, and could be operated in both pulsed and continuous mode [11]. The YAG crystal has a relatively high thermal conductivity, which improves thermal loss in the laser cavity. For this reason, the power of CW Nd:YAG laser is up to a few hundred Watts. However, if applying in a pulsed mode, high pulsing rates can be achieved, and average powers of up to 1 kW is possible. The YAG crystal is transparent and colourless. When doped with approximately 1% Nd, the crystal takes on a light blue colour [26]. An Nd:YAG rod is shown in figure 2.3 [25]. The pulsed Nd:YAG laser is desirable for hole piercing and deep keyhole welding applications. In cleaning applications, the Nd:YAG lasers with Q-switching operating at nanosecond pulses are typically used for cleaning rust on metals and for art work restorations.

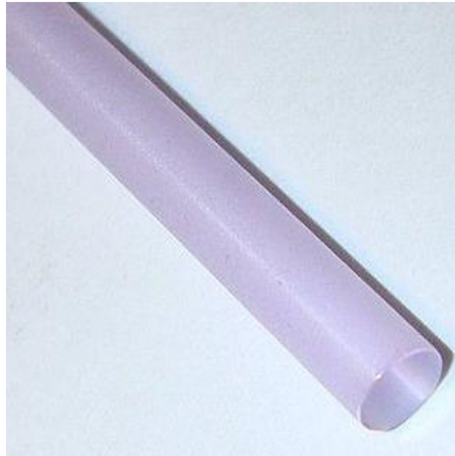

Figure 2.3 Nd:YAG rod inside laser [25]

2.3.3 KrF excimer Laser

The full name of KrF lasers is krypton fluoride laser, and is a particular type of excimer laser. The term excimer is also a shortening for excited dimer. The excimer laser is a form of ultraviolet laser which is commonly used in semiconductor manufacturing and human tissue surgeries [27,28]. It usually uses a combination of an inert gas, such as argon, krypton, or xenon, and a reactive gas, typically fluorine or chlorine. Under the appropriate conditions of electrical stimulation, a pseudo molecule called an excimer is created, which can only exist in an excited state and create laser light in the ultraviolet range [29].

Upon electrical field excitation, the krypton gas will react with the fluorine gas, which produces krypton fluoride. It is a temporary formation in an excited energy state. The reaction formula is given by equation 2.1 [30],

$$2Kr_{(g)} + F_{2(g)} \rightarrow 2KrF_{(g)} \qquad (2.1)$$

This formation of the excited dimer can undergo spontaneous or stimulated emission, which reduces its energy state to a metastable ground state and quickly dissociates into unbound atoms. The reaction is expressed by equation 2.2 [30],

$$2KrF_{(g)} \rightarrow 2Kr_{(g)} + F_{2(g)} + energy \tag{2.2}$$

The result of equation (2.2) is an excimer laser that radiates energy at 248 nm, which lies in the near ultraviolet portion of the spectrum. The laser can be generated by an excimer molecule because it has an associative excited state, but a repulsive dissociative ground state due to the fact that krypton do not usually form chemical compounds. However, in an excited state, they can form temporarily bound molecules with dimers or with complexes, such as fluorine and chlorine. The excited compound can release its energy by stimulated emission [30].

Compared with the CO_2 and Nd:YAG lasers, the KrF eximer laser was the first laser used for cleaning particles by Tam and his team [31]. The excimer laser is good at cleaning of very small features due to its short wavelength [32]. Besides, a plasma zone can be created by this laser easily, which can be utilised in a process called laser plasma cleaning [33]. On the other hand, the KrF excimer laser is a very important manufacturing tool for microlithography, especially for the silicon material [34]. Also it is already known that the energy per photon of an excimer laser (4.9 eV) is some 40 times greater than that of a carbon dioxider laser (0.12 eV), which could significantly restrict the expansion of the heat affected zone on the material surface, and effectively

avoid the corresponding surface damages [35].

2.4 History and development of laser cleaning

Arthur Schawlow, the Nobel Prize winner in 1981 for his work on the laser spectroscopy, developed the fundamental science behind the laser at Bell Laboratories with Charles Townes in 1957-1958. In the 1960s the public thought of a laser was an invention seeking of an application. Schawlow invented a laser eraser and applied a patent for this invention. According his design, a laser eraser could be built into a typewriter. If the operator makes a mistake, he could start the laser eraser to remove where it is typed. The prototype device patented by Schawlow was using a small ruby laser. This is the first documented use of laser cleaning [36-39].

The second documented event in laser cleaning history was to the use of lasers in art conservation. In 1972 the John F Asmus from University of California, San Diego, visited Venice to study laser holography for the recording of the treasures in the city. He found the effect of the interaction of a focused ruby laser with an encrusted stone statue. It was found that the darker encrustations were selectively removed from the surface, and no damage was observed on the substrate of white stone. Asmus returned to the United States and began researching laser cleaning of art works, particularly in the use of pulsed ruby and pulsed Nd:YAG lasers [40]. From then on, more and more buildings and statues were cleaned by this new technique, such as Santa Stephan's Cathedral in Austria, Hero Memorial in Warsaw, Poland [41].

In the 1980s, a group led by Susan Allen of Florida State University, USA, developed techniques for the removal of small submicron debris particles from silicon wafers [37]. Meanwhile IBM further developed this technique to clean their microelectronic devices, which is the first application of laser cleaning in microelectronics industry. Previously lithography worked in parallel with optical and x-ray lithography, as well as on two types of electron-beam lithography, namely direct-write electron beam and masked electron beam lithography [31]. The IBM German Manufacturing Technology Centre - GMTC focused on latter technique. The basic idea was to produce a stencil mask, which contained the pattern to be printed as physical holes. To obtain more accurate results they shadowed this pattern with an electron beam onto the resist wafer. Its mechanism is not like standard direct write electron beam lithography machines. This lithographic technique is called Electron Beam Proximity Printing (EBP). Therefore it combined the high resolution of electron beam and overlay capabilities with high printing speed, and consequently it was ideally suited for high throughput manufacturing of memory chips [31].

The key component of EBP lithography was the stencil mask [42]. This mask was produced from a silicon wafer, the central area of which was wet-etched to form a membrane with 3 μm thickness. The lines on stencil mask pattern were manufactured by the aforementioned method, and its width was 0.3 μm. During the manufacturing process, contaminates were found on the stencil mask in the lithography chamber, which were difficult to remove by traditional cleaning techniques, because they were

strongly adhered on the surface due to Van der Waals, electrostatic, and capillary forces. The adhesion forces of 1 μm sized particles, for example, could be 10^6 times larger than their gravity [43].

Due to the probability of the recontamination happening on the membrane mask when using wet cleaning baths, GMTC developed a laser cleaning technique that could successfully remove the sub-micron size particles from the membrane surface and avoid the risk of substrate damage. Initially, a pulsed KrF excimer laser was used. The first job was to measure the damage threshold of the mask under laser irradiation. It was found that the stencil mask could survive under irradiation at fluencies in excess of 100 mJ/cm^2 [38]. Also particles of different materials, such as SiO_2, Al_2O_3, and polystyrene, with size of 0.3 to 5 μm were successfully removed from the silicon wafer. Their cleaning thresholds were between 300 and 500 mJ/cm^2. This experiment was documented as one of the earliest attempts of laser cleaning in the microelectronics industry. The cleaning effect of this experiment is shown in figure 2.4 [44].

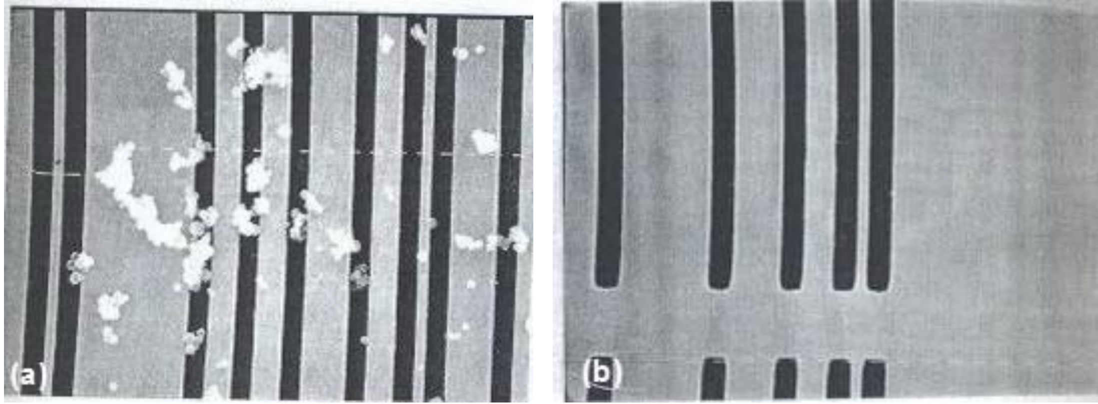

Figure 2.4 (a) silicon membrane stencil mask contaminated with Al_2O_3-spheres (diameter from 0.3 to 1.5 μm). (b) The same silicon membrane stencil mask after four pulses of KrF excimer laser irradiation [44]

2.5 Mechanism of laser cleaning

The established literature shows that contaminants and substrate both can absorb the laser energy depending their absorbtivities at different laser wavelengths [45]. A thin liquid created by brush or steam evaporation on target can improve the cleaning rate [46]. This method is called steam or wet laser cleaning. These small (submicrometre) particles on the surface is difficult to remove by conventional techniques [47,48].

Despite the rising demands and requirements of laser cleaning, there has been insufficient consideration of the mechanisms involved in laser cleaning [48]. Currently, it is known that there are several mechanisms for laser cleaning of contaminants from a substrate surface. These are ablation, spallation, transient surface heating, evaporation pressure, photon pressure, in dry laser cleaning and steam laser cleaning.

2.5.1 Ablation

From the established literature, it is known that the cleaning mechanism for the laser ablation of the contaminant layer on the substrate has been studied [49,50]. At relatively high laser intensity cleaning occurs as a result of the ablation of contaminants. Under this scenario, the absorption coefficient of the contaminant layer should be sufficiently large to lead to a temperature rise for vaporisation, meanwhile the absorption coefficient of the substrate is sufficiently small to restrict the temperature rises to particular values that does not allow the generation of melting or cracks because of differential thermal expansion [48,51]. It was shown that a one dimensional heating model could demonstrate this heating process on the material surface, as shown in figure 2.5 [48].

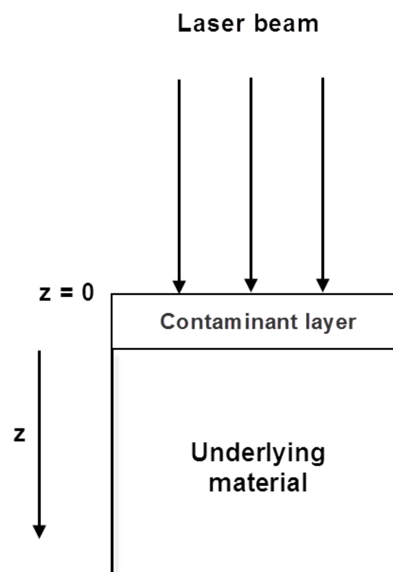

Figure 2.5 Schematic of a one-dimensional heating model

If a constant flux, F_0, is absorbed by the surface (depth, $z = 0$) and there is no phase

change in the material, the solution of the equation for heat flow in one dimension, for a uniform laser beam, is [48],

$$T_{(0,t)} = \frac{2F_0}{k}(\alpha t/\pi)^{1/2} \quad (2.3)$$

where $T_{(0,t)}$ is temperature at the surface after time t, k is thermal conductivity, α is thermal diffusivity, and t is irradiation time.

The following additional assumptions were made [48]:

1. The laser beam is uniform with no transverse variation in intensity;
2. The contaminant layer is uniform and flat;
3. The beam diameter is much larger than the contaminant layer thickness;
4. The beam diameter is much larger than the thermal diffusion distance.
5. The substrate is semi-infinite, i.e. its size is much higher than the thermal diffusion length.

The equation of thermal diffusivity is given by equation 2.4 [48],

$$\alpha = k/\rho C_v \quad (2.4)$$

where ρ is density and C_v is specific heat.

The penetration depth of heat, z, in the material is expressed by [48],

$$z = (\alpha\, t)^{1/2} \quad (2.5)$$

The flux absorbed by material is given by equation 2.6 [48],

$$F_0 = (1 - R)I_0 = \beta I_0 \tag{2.6}$$

where R, β and I_0 are reflectivity, absorptivity and incident flux respectively.

The initial temperature $T_{(0)}$ is given by,

$$T_{(0)} = C_m \; \beta \; I_0 \tag{2.7}$$

where C_m is a constant. If all variables are fixed, the surface temperature achieved by contaminant layer and substrate both depend on the value of β. Its difference could be significant.

Self limiting effect is a typical phenomenon in laser cleaning if a series of pulses is applied to the contaminant layer whose absorptivity is much larger than that for substrate [48]. Initial pulses result in the vaporisation of the contaminant layer. Once the contaminant layer is removed, the temperature rise of the substrate would be much smaller and not reach its melting point due to the large difference of absorptivity between contaminant layer and substrate at laser wavelength. The temperature rise of self limiting effect is shown in figure 2.6 [40].

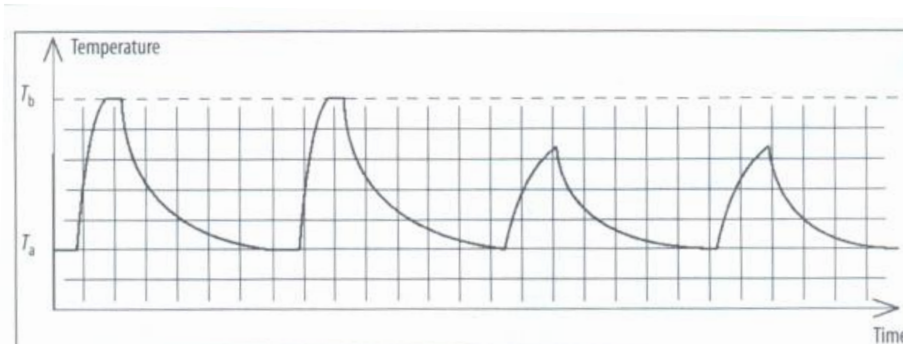

Figure 2.6 Pulse intensity versus time showing basis for self-limiting effect [40]

2.5.2 Spallation

The contaminant layer can absorb sufficient energy to reach the vaporisation temperature at high laser fluence level. High temperatures, typically 10^4-10^5 K, are produced in the vaporised material from the surface, and this vapour becomes partially ionised plasma and absorbs the laser energy strongly. The initial surface vaporisation on the target is shielded from the laser by the plasma cloud. As the pulse continues, the plasma cloud is further heated and high pressures, even 100 kbar in some cases, can be achieved, which results in a shock wave which produces compression of the surface of the target material. When the laser pulses ends, the plasma expands away from the surface. The material surface relaxes and a thin surface layer (1-100 µm) is removed due to spallation [52,53]. Cleaning is more rapid in this case. However, it is easy to damage the substrate beneath the contaminant layer that requires removal.

2.5.3 Transient surface heating

When laser radiation is absorbed by the surface periodically at high heating and cooling rates, the heated layer will generate a oscillating pressure, and related shock waves will travel through the material. If the magnitude of stresses becomes sufficiently large so that the shear stress of the material is exceeded, removal of material may take place by physical fracture [54,55].

2.5.4 Evaporation pressure

Another mechanism which can produce high pressure pulses at an irradiated surface is the evaporation pressure. Under this circumstance, the generation of shock wave induced by the laser is a result of the expansion of vapour away from a metal surface against the ambient gas. There will be a region of compressed air between metal vapour and the ambient air. The shock waves for short laser pulse are produced by the recoil pressure of rapid vaporisation of metal, and the contaminant layer could be removed when the shock wave front encounters with it. This mechanism would not require the absorption of laser energy in a plasma and would arise simply as a result of the high momentum of the evaporating material [56,57].

2.5.5 Photon pressure

When photons arrive to the surface, there will be a small pressure generated. This pressure is proportional to the laser power density. Highly focused lasers are capable of providing a very high flux of photons [48]. The pressure delivered to the surface is small but perhaps capable of moving small surface objects. This mechanism has been considered in the case of removal of submicron particles from microelectronic components. However, it is unlikely that sufficient force would be applied for most laser cleaning purposes [58].

2.5.6 Dry laser cleaning

For dry laser cleaning, two situations are indicated regarding the material

absorptivities. The first one is understood as strong substrate absorption. In this case, the absorptivity of substrate at the laser wavelength is far higher than that for particle (contaminant). Rapid pulsed heating of the dry substrate leads to the ejection of particles (contaminant) due to the sudden thermal expansion of the substrate [59-62]. Although the expansion amplitude is small, strong acceleration could occur on the substrate and particle, because the reaction time is very short [48].

The other situation is called strong particle absorption. In this case, the absorptivity of particle (contaminants) is higher than that for substrate, and the laser energy usually results in the vibration of particle, which also could overcome the adhesion force. Nevertheless, compared with strong substrate absorption, the situation - strong particle absorption always requires the relatively higher laser energy output to achieve same cleaning effect [63-66]. The schematic of two situations for dry laser cleaning is shown in figure 2.7 [44].

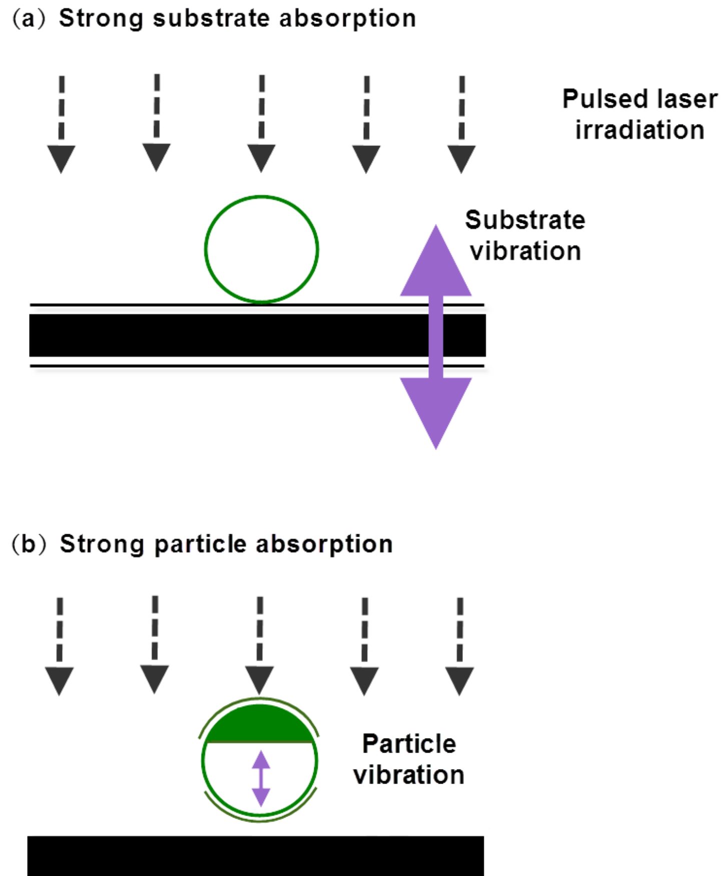

Figure 2.7 Mechanisms involved in dry laser cleaning for the removal of small particles from silicon wafer surfaces [44]

2.5.7 Steam laser cleaning

The mechanism of steam laser cleaning is illustrated in figure 2.8. Three absorption situations may occur [48]. The first one is strong substrate absorption. Hence, the substrate with high absorptivity at laser wavelength covered by a water film could be efficiently heated at the liquid-substrate interface through laser irradiation, as shown in figure 2.8 (a). The superheating and explosive evaporation of the water could provide efficient particle removal [67,68]. The second one is equal liquid and substrate absorption. The liquid and substrate have the similar absorptivities at the

laser wavelength. The water layer could remove the particle. However, it has lower energy efficiency than that for the case of strong substrate absorption [69,70]. The reason is that the absorption depth of laser is larger than the thickness of water layer, and only a portion of the laser energy is absorbed by the water. The remaining energy penetrates to the substrate, which could generate the interface heating, as shown in figure 2.8 (b). Thus, more laser energy is required to create explosive evaporation of the liquid. The third one is strong liquid film absorption. The absorptivity of liquid is obviously higher than that for the substrate. Its cleaning was less effective than the other two cases since the peak temperature was achieved at the top surface of the liquid rather than at the substrate-liquid interface, as shown in figure 2.8 (c) [44]. Tam et al. have concluded that the mechanism of strong substrate absorption provides the most efficient cleaning under the same laser parameters in three mechanisms [2,48].

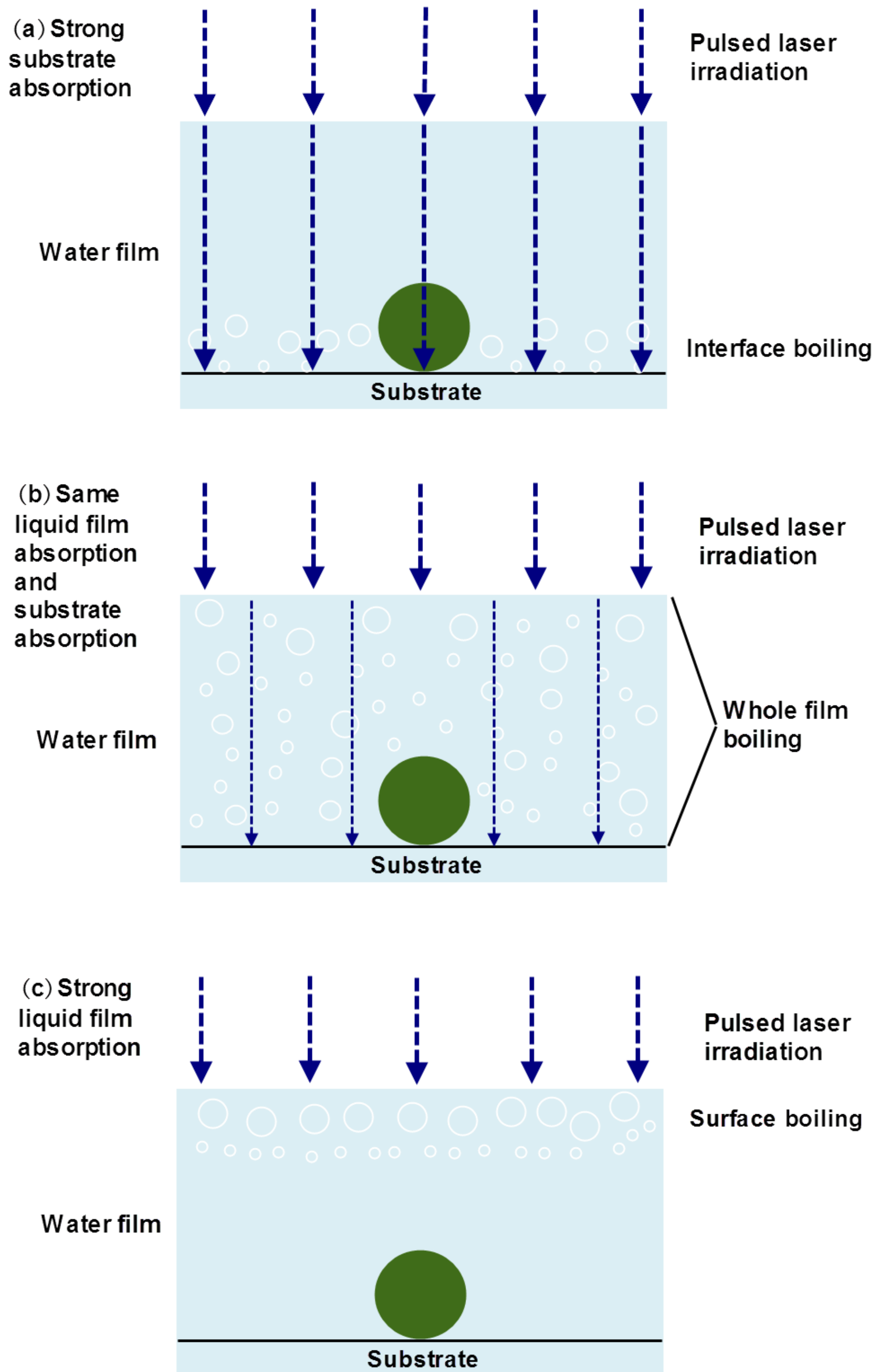

Figure 2.8 Mechanism involved in steam laser cleaning for the removal of small particles from silicon wafer surfaces [44]

2.6 Cleaning threshold

Generally if the cleaning objective is defined, the laser cleaning can remove the contaminations on the surface when the energy density or fluence is above a particular value - I_t. For this reason, this value is called cleaning threshold [71]. Obviously, the parameters about cleaned subject, laser and working environment all can influence this value as well. Thus I_t relies on the laboratory test most of time, is an empirical parameter. In fact, finding one proper cleaning energy density (marked as I_w) is a very important task. To find this value needs to consider several factors, for example cleaning effect, cleaning speed, quality of laser. Many papers have already proved that too high or too low I_w both cannot get the best cleaning result for common contaminants [72]. It is known that I_w must be higher than I_t, but it does not mean that I_w would be higher than it too much [73]. There are two reasons for this conclusion. One is protecting of substrate, the other one is the air or gas breakdown phenomenon which is caused by too high laser power density [74]. When air or gas breakdown occurs, the efficiency of cleaning will drop greatly, because much laser energy would consume on it. In dry air, the threshold of air breakdown is about 10^8-10^9 W/cm^2. But if there are aerosol particles in the air, the threshold value may drop 2 or 3 magnitudes. Therefore, the air surround substrate is easy to be broken [75].

2.7 Adhesion forces

Forces perform on the particles and substrate and result in the strong adhesion between them [37]. These forces are known as Van der Waals force, capillary force,

and electrostatic forces.

2.7.1 Van der Waals force

Van der Waals force is typical and a most important adhesion force for particles less than a few micron in size [37]. It includes forces between molecules processing dipoles and quadrupoles caused by the polarizations of the atoms and molecules in the material [76-78].

In laser cleaning system, one ideal model is used to analyse Van der Waals force. In this system, the particles are all ideal spherical and the solid surface is very flat. So Van der Waals force is given by [76],

$$F_1 = \frac{hr}{8\pi z^2} \tag{2.8}$$

where, r, h and z are the particle radius, the material-dependent Liftshitz - Van der Waals constant and the atomic separation between the particle and surface respectively. A typical value of h range is from a low value of 0.6 eV for polymer and polymer interaction to a large value of 9.0 eV for gold and gold interaction. For Van der Waals-bonded crystals, the atomic separation, z, is approximately 4 angstroms [37].

The Van der Waals force can make most of particles and surfaces deform. The level of deformation depends on the hardness of the particles and surface. Besides, the deformation can also produce additional Van der Waals, F_2, which is a function given

by equation 2.9 [76],

$$F_2 = \frac{h\delta^2}{8\pi z^3} \tag{2.9}$$

where δ is the radius of the adhesion surface area. Therefore, the total Van der Waals force, F_v, between particles and a flat surface is the sum of the Van der Waals force between ideal spherical particles and a flat surface and the additional Van der Waals force caused by deformation, which is given by equation 2.10 [76],

$$F_v = F_1 + F_2 = \frac{hr}{8\pi z^2} + \frac{h\delta^2}{8\pi z^3} \tag{2.10}$$

If there is a large deformation, such as $\frac{\delta}{\gamma} \geq 10\%$, the Van der Waals force between the ideal spherical particle and a flat surface is much lower than the additional Van der Waals force. So it is necessary to calculate the approximate value of the Van der Waals adhesion force per unit area. Its equation is given by equation 2.11 [76],

$$P = \frac{F_v}{\pi\delta^2} \approx \frac{h}{8\pi^2 z^3} \tag{2.11}$$

This function can be used in many non-circle adhesion area scenarios. In these cases, the Van der Waals force per unit area can be given directly by equation 2.12 [76],

$$P = \frac{h}{8\pi^2 z^3} \tag{2.12}$$

2.7.2 Capillary and liquid bridge force

Sometimes the liquid film could be found between particles and surface because of high humidity in the environment. It is formed by capillary force, F_c, which is a function of the particle radius and liquid surface tension. The formula is shown in equation 2.13 [37],

$$F_c = 4\pi\gamma R \tag{2.13}$$

where γ is the liquid surface tension and R is the radius of the particle has liquid bridge [37].

The thickness of liquid film depends on the hydrophilicity of particle surface and humidity of air [79,80]. Their higher values often mean that a thicker liquid film could be formed. When the humidity of air or gas achieves to 65%, the contacts of each particle would form a liquid bridge, which furthermore generates liquid bridge forces [81]. A typical liquid bridge geometry models is shown in figure 2.9.

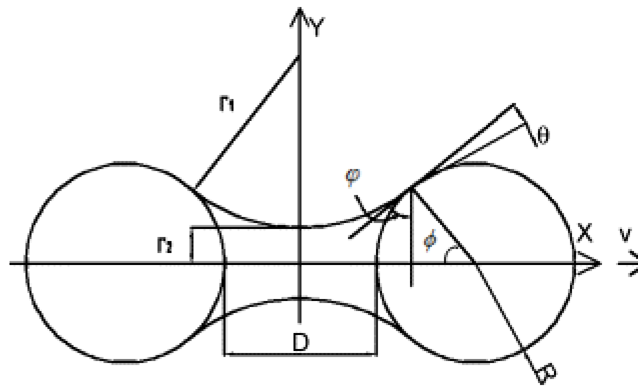

Figure 2.9 Liquid bridge geometry model

The functions of liquid bridge forces are summarised in the established literature. The liquid bridge force, F_L, is calculated by the sum of the capillary press, F_{cp}, and tension, F_t. The equations are [82],

$$F_{cp} = -\pi R^2 \sigma (\frac{1}{r_1} - \frac{1}{r_2}) \sin^2 \phi \tag{2.14}$$

$$F_t = 2\pi R \sigma \sin\varphi \sin(\theta + \varphi) \tag{2.15}$$

Thus, the final equation for liquid bridge force should be [82],

$$F_{\mathrm{L}} = F_{cp} + F_t = -2\pi R\sigma[\sin\varphi \sin(\theta+\varphi) + \frac{R}{2}(\frac{1}{r_1} - \frac{1}{r_2})\sin^2\phi] \qquad (2.16)$$

where σ, θ, Φ and φ are liquid surface tension, moisture contact angle, half filling angle and angle of nip – half of the angle between connection ring and particle centre, respectively, and r_1 and r_2 are two curvatures of radius for liquid bridge. Their related positions are shown in figure 2.9. To the particles with high hydrophilicity contact with surface the magnitude of liquid bridge force, F_L, approximates to the magnitude of capillary force [82].

2.7.3 Electrostatic Force

There are two types of electrostatic forces adhere particles on surface. The first one is coulombic attraction functioned by electrostatic image force, F_i, caused by bulk excess charges on the surface and particle [76,83]. The equation of this force is given by [76],

$$F_i = \frac{1}{4\pi\varepsilon}\frac{Q_p Q_s}{d^2} \qquad (2.17)$$

where Q_p, Q_s, ε and d are the charges on the particle, the charges on the substrate, the permittivity of the free space and the distance between the charge centres respectively. The second electrostatic force for small particles is electrical double layer forces that induced by electrostatic contact potential, F_E [76,84]. When two different materials are in contact each other, the contact potential would be formed because of differences in the local energy states and work functions. It is well known that electrons transfer between two materials until their equilibrium is reached where the current flow in

both directions is equal [76]. The contact potential difference, U, generally ranges from 0 to about 0.5 V, which forms the double layer charge region. In the case of laser cleaning, only the surface layer carries contact charges. This force is given by [76],

$$F_E = \frac{\pi \varepsilon U^2 r}{z_E} \tag{2.18}$$

where ε is the permittivity of free space, z_E is the distance between the particle and the surface and r is the radius of the particle.

2.7.4 Dominant Adhesion Forces

For a dry system capillary force would not be considered in calculation of the adhesion force between particles and substrate, because liquid film could not form. It is experimentally proved that Van der Waals force plays the most important role for the adhesion of tiny particles with diameter less than a few microns, and electrostatic force is the main adhesion force for large particles size more than 50 µm [37,85]. In real semiconductor manufacturing industry, the diameter of particles are much smaller than 50 µm. Hence, Van der Waals force, F_v, is considered as the dominant adhesion force, F_d, shown as equation 2.19, for tiny particles on flat surfaces [76].

$$F_d = F_v \tag{2.19}$$

For a steam cleaning system the main adhesion forces, F_w, are capillary force and Van der Waals force. Liquid bridge force is sorted in capillary force, and not listed separately. Its equation is shown as [76],

$$F_w = F_v + F_c = \frac{hr}{8\pi z^2} + \frac{h\delta^2}{8\pi z^3} + 4\pi\gamma r \qquad (2.20)$$

2.8 Cleaning force

2.8.1 Dry laser cleaning forces

Under the scenario of transparent particles on the substrate with high absorptivity at laser wavelength, the laser energy is fully absorbed and cause instantaneous temperature rise, which generates a thermal expansion that performs on the particles. Therefore, the cleaning force per unit area, f_c, from this thermal expansion is defined as [76],

$$f_c = \gamma E \Delta T(0,t) \qquad (2.21)$$

where γ and E are the linear thermal expansion coefficient and the elastic modulus of the substrate, respectively. The $\Delta T(0,t)$ is the temperature rise at the substrate surface.

2.8.2 Steam laser cleaning force

For a wet system capillary force and Van der Waals force are the main adhesion forces of tiny particles which can be calculated by equation (2.13). For laser irradiating on a solid surface coated by a liquid film, the liquid near the interface of substrate can be superheated through thermal diffusion [86]. Growth of vapour bubbles on the interface can be observed [87]. In process of bubble growth, the pressure and temperature in the bubbles are ranged as [76]:

$$P_\infty \le P_V \le P_{sat}(T_\infty) \qquad (2.22)$$

$$T_{sat}(P_\infty) \le T_V \le T_\infty \tag{2.23}$$

where P_∞, P_v, P_{sat}, T_{sat}, T_v, and T_∞ are the ambient liquid pressure, vapour pressure inside the bubble, saturation vapour pressure, saturation temperature, temperature inside the bubble and ambient liquid temperature, respectively.

The process of bubble growth is divided into two scenarios, inertial controlled growth and heat transfer controlled growth [76]. In the cases of laser irradiation, inertial controlled growth likely occurs. Under this scenario, $T_v \approx T_\infty$, and with the constraint of local thermodynamic equilibrium, $P_v = P_{sat}(Tv) \approx P_{sat}(T_\infty)$ [88].

The velocity of bubble growth in inertial controlled process has been theoretically expressed as [88]:

$$v(T) = \left(\frac{2}{3}\frac{P_v(T) - P_\infty}{\rho_l(T)}\right)^{1/2} \tag{2.24}$$

where $v(T)$ and $\rho_l(T)$ are the velocity of bubble growth, liquid density at temperature of T, respectively. It has been known that water film on metal surface can enhance the laser generated pressure of stress wave by up to 20 dB [89]. The enhancement of pressure is caused by plasma formation, rapid evaporation and bubble expansion. The plasma formation occurs only for high power laser irradiation because of air breakdown. When laser intensity is below the breakdown threshold, the pressure of stress wave is dominated by the rapid evaporation and bubble expansion [76].

Based on literature, the pressure of stress wave is deduced relying on three

assumptions [76,88].

(1) In the area near to the interface between liquid and substrate, the vapour layer is created by evaporation of liquid, which compresses liquid layer and generates stress wave [90].

(2) Because of the non-uniform temperature distribution in the liquid film, the vapour pressure in bubbles is considered as the average vapour pressure of the superheated liquid layer.

(3) The expansion velocity of vapour layer is considered to be equal to the growth velocity of the bubbles, as expressed in equation (2.24). The average energy on unit area on vapour and liquid interface, E_i, during the inflation of vapour layer is [76],

$$E_i = \int (P_v - P_\infty) v f \, dt \tag{2.25}$$

where v and f are expansion velocity and volume fraction of vapour, respectively. To the stress wave in this process, its energy per unit area, E_s, is defined as [91],

$$E_s = \int \frac{P^2}{2\rho c} dt \tag{2.26}$$

where ρ, c and P are the liquid density, transmit speed and pressure of stress wave, respectively. According the equations (2.25) and (2.26), the pressure of stress wave at the vapour and liquid interface, P, is [76],

$$P = [2\rho c (P_v - P_\infty) v f]^{1/2} \tag{2.27}$$

2.9 Plasma shielding effect

The mechanism of material ionization is sophisticated and strongly affected by many factors including material properties, concentration and thickness of plasma electrons and the ion cloud. However, for calculation purpose a simplified model was established based on Beer-Lambert law, which assumes that a layer of plasma contacts the evaporation face closely. Its expression is given as [92],

$$I_s(t) = I_0(t)\exp(-\alpha\Lambda) \qquad (2.28)$$

where $I_s(t)$ is the temporal laser intensity at the sample surface, α is absorption coefficient of plasma cloud, Λ is the thickness of plasma cloud. The thickness of plasma cloud, Λ, is given by [93],

$$\Lambda = c_s t \qquad 0 < t < \tau_\ell \qquad (2.29)$$

where c_s is the hydrodynamic expansion velocity of the plasma. The absorption coefficient, α_p, is deduced from the equation (11), which is expressed by [94]

$$\alpha_p = \frac{4\pi k_{ext}}{\lambda} \qquad (2.30)$$

where k_{ext} and λ are extinction coefficient of material and wavelength of laser, respectively. From the established literature, it is known that absorption coefficient is also related to the laser output power [95].

2.10 Laser shock cleaning

Lee and Watkins developed the laser shock cleaning technique [65]. In this method, laser beam was used to generate the plasma shock wave above the particles through air breakdown phenomenon. Its strong flow would blow and clean the tiny particles

on the surface. The diagram of this technique is shown as figure 2.10 [96]. Corresponding shock wave dynamic was analysed by Lim et al. [96]. The equation of shock pressure is given by [65,96],

$$P_a = bI^{0.7}\lambda^{-0.3}\tau^{-0.15} \tag{2.31}$$

Where P_a is the shock pressure (kbar), b is the material dependent coefficient, I is the laser intensity (GW/cm^2), λ is the laser wavelength (μm) and τ is the pulse length (ns).

Also, Song et al. extended this technique to the field of under water laser cleaning [97]. In their study, laser beam was focused into the water, which induced shock wave and formed cavitation bubbles. The contaminant was cleaned by the high-speed liquid jet during bubble collapse. In fact, laser shock cleaning is an indirect laser cleaning method [98]. The contaminants (tiny particles) must be removed by the other forms of power, such as shock wave, which is initiated by the laser energy.

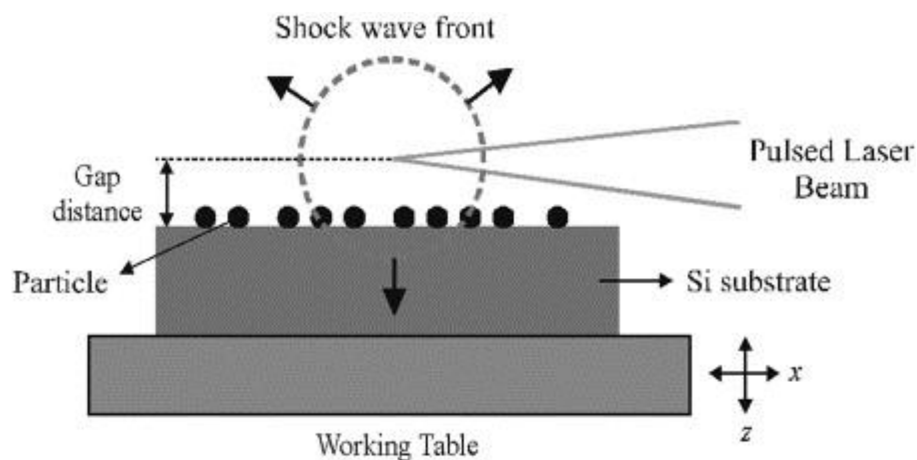

Figure 2.10 Schematic for laser shock cleaning [96]

2.11 Simulation methods

2.11.1 Finite elements method (FEM)

The finite element method (FEM) is a numerical technique to obtain approximate solutions for partial differential equations (PDE). It was developed for solving complex elasticity and structural analysis problems in civil and aeronautical engineering. Its development could be traced back to the work by Hrennikoff in 1941 and Courant in 1942 [99]. The solution approach is based on the complete differential equation, which is understood as steady state problems, or disassembles the PDE into an approximating system of ordinary differential equations [99]. Once the domain changes, the desired precision would loss in the entire domain and the solution becomes smoothness. The steps of FEM analysis are shown below.

(1) Discretization

Using the finite element method, the solution domain is discretized into smaller regions called elements, and the solution is determined in terms of discrete values of some primary field variables φ (x, y, z) at the nodes [100]. The number of unknown primary field variables on a node is called the degree of freedom [101]. The governing differential equation is applied to the domain of a single element. At the element level, the solution to the governing equation is replaced by a continuous function approximating the distribution of φ over the element domain D^e, expressed in terms of the unknown nodal values φ1, φ2, φ3 of the solution φ. A system of equations in terms of φ1, φ2, and φ3 can be formulated for the element.

(2) Element analysis

Once the element equations have been determined, the elements are assembled to the entire domain D. The solution φ (x, y, z) to the problem becomes a piecewise approximation, expressed in terms of the nodal values of φ [100]. A system of linear algebraic equations results in the assembly procedure. For practical engineering problems the number of elements could be thousands, which means calculation is relying on super computers and related commercial software to find an acceptable solution.

(3) Element combination

Using boundary conditions, elements can be connected to each other, and form one integrated finite element formula. Boundary of one element is marked S^e. Accordingly the differences and characters of this formula, one solution could be found by proper method. The schematic diagram of elements and boundaries is shown in Figure 2.11 [101]. This concept has been applied on multiple mechanical, thermal, even optical analyses [59,102].

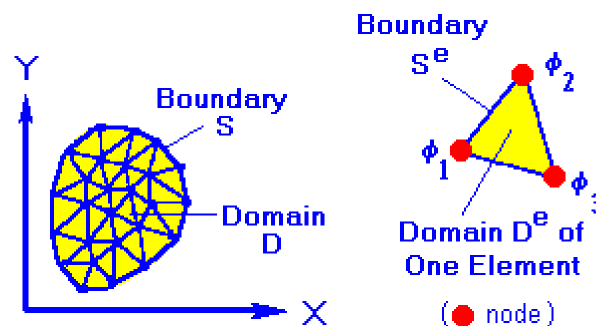

Figure 2.11 The schematic diagram of elements and boundaries [101]

2.11.2 Finite difference method (FDM)

Analytical methods may fail if the Partial Differential Equation (PDE) is not linear, the solution region is complex, or the boundary conditions are of mixed types and time dependent. Finite difference method (FDM) is a numerical method to solve the PDEs. It was first developed by Thom in the 1920s [103]. Basically the continuous solution domain could be replaced by the matrix made up from finite discrete grid points. The finite difference method is based on the approximations that permit replacing differential equation by finite difference equations.

The error in the solution is defined as the difference between the numerical and analytical solution. Two main sources of error are realised. The one is called round off error, which is the loss of precision due to computer rounding of decimal quantities, the other one is truncation error that is the difference between the exact solution of the finite difference equation and the exact quantity assuming perfect arithmetic [99].

2.11.3 Finite integration technique (FIT)

The finite integration technique (FIT) is a spatial discretization scheme to numerically solve electromagnetic field problems in time and frequency domain. It preserves basic topological properties of the continuous equations such as conservation of charge and energy. FIT was proposed in 1977 by T. Weiland and has been enhanced continually over the years [104,105]. This method covers the full range of electromagnetics (from static up to high frequency) and optic applications and is the basis for commercial

simulation tools [104,105].

The basic idea of this approach is to apply the Maxwell equations in integral form to a set of staggered grids. This method stands out due to high flexibility in geometric modelling and boundary handling as well as incorporation of arbitrary material distributions and material properties such as anisotropy, non-linearity and dispersion. Furthermore, the use of a consistent dual orthogonal grid (e.g. Cartesian grid) in conjunction with an explicit time integration scheme (e.g. leap-frog-scheme) leads to calculate and memory-efficient algorithms, which are especially adapted for transient field analysis in radio frequency (RF) applications. The Maxwell's equation in integral form is given by [106]:

$$\oiint_{\partial V} E \cdot dA = \frac{Q(V)}{\varepsilon_0} \tag{2.32}$$

$$\oiint_{\partial V} B \cdot dA = 0 \tag{2.33}$$

$$\oint_{\partial S} E \cdot dl = -\frac{\partial \Phi_s (B)}{\partial t} \tag{2.34}$$

$$\oint_{\partial S} B \cdot dl = \mu_0 \cdot Is + \mu_0 \cdot \varepsilon_0 \cdot \frac{\partial \Phi_s (E)}{\partial t} \tag{2.35}$$

Where ∂V and V are its boundary surface and any three-dimensional volume respectively, E is electric field intensity, dA is differential vector element of surface area A, $Q(V)$ is net electric charge within the three-dimensional volume V, ε_0 is permittivity of free space, B is magnetic field density, ∂S and S are its boundary curve and any surface respectively, dl is differential vector element of path length tangential

to the path, $\frac{\partial}{\partial t}$ is partial derivative with respect to time, $\Phi_s(B)$ and $\Phi_s(E)$ are magnetic and electric flux through any surface S respectively, μ_0 is permeability of free space and I_s is net electrical current passing through the surface S.

2.11.4 Computational fluid dynamic (CFD)

Computational fluid dynamic (CFD) is a fluid mechanics using numerical methods to solve fluid flow problem. Generally the interaction of liquids and gases with interface needs to be calculated relying on boundary conditions. Better solutions could be achieved by using computer. Reasonable calculation methods would improve the accuracy and speed of simulation. Corresponding methods were first developed to solve the Linearized Potential equations. Two dimensional methods, using conformal transformations of the flow about a cylinder to the flow about an airfoil were developed in the 1930s [107]. The development of the computer made the three-dimensional methods available for approaching reality. The first work using computers to model fluid flow, the Navier-Stokes equations, was performed at Los Alamos National Labs, in the T3 group. The group published a paper modelling two dimensional swirling flow around an object in July 1963[108].

The finite volume method (FVM) is a common approach used in CFD. The equations are solved from discrete control volumes. Finite volume methods change the PDEs in conservative form, and then discretize the new equation. This guarantees the

conservation of fluxes through a particular control volume. The form of finite volume equation that converts of PDE is given by [108],

$$\frac{\partial}{\partial x}\iiint Q dV + \iint F_{vector} dA = 0 \quad (2.36)$$

where Q is the vector of conserved variables, F_{vector} is the vector of fluxes, V is the volume of the control volume element, and A is the surface area of the control volume element.

The normal procedure of CFD is followed as shown below.

1. Preprocessing. The geometry of the problem is defined. The volume occupied by the fluid is divided into discrete cells (the mesh). The mesh may be uniform or non uniform. Then material properties, such as enthalpy, motions during phase change, is loaded into the model. Finally the boundary conditions that involve fluid behaviour are defined.
2. The equations are solved as a steady state or transient mode.
3. A postprocessor is used for the analysis and visualsation of the resulting solution.

2.11.5 Modelling boundary conditions

There are three types of heat transfer involved in the laser heating model: conduction, convection and radiation. The absorbed laser light energy changes into thermal energy at the laser material interaction zone on the substrate surface, and the temperature would rise above the melting point of the material. The material starts the melting

procedure, and related phase change occurs immediately. The heat flow process involved is dominated by conduction [109]. In this period, some of the heat in the melt pool may be lost to environment in the electromagnetic wave form, which is called radiation heat transfer, and does not require the presence of a medium. Thermal convection interaction describes the thermal energy in laser beam-material interaction zone dispersed by the influence of environmental fluid flow [110]. Considering the short pulse duration and high peak power for nanosecond laser, thermal convection and radiation only take a small proportion of energy diffusion in the bulk of the material, which is neglected in the current model [111]. Meanwhile, due to the fact that the software is only capable of handling finite size structures, the boundary conditions on the edge of model were defined as open boundary in both electric and thermal modules. The open boundary condition mimics the situation that materials at the computing boundaries extend themselves to the infinite space.

On the other hand, melting is non alternative phase change during laser processing. The boundary conditions for this phenomenon are defined regarding on the regions. The liquid phase or melting pool can be divided into three regions, cold boundary layer near solid liquid interface, warm boundary layer near the heated area, and the core region between these two boundary layers. The solid-liquid interface can be assumed to be sufficiently straight and long. In addition, the following assumptions are made:

1. The properties of liquid phase are function of temperature. The liquid is Newtonian

and incompressible.

2. The Prandtl number of the liquid phase material is greater much than 1 [112].

3. The liquid motion induced by volumetric variation during melting is neglected [113,114].

2.12 Modelling of laser cleaning

During the laser cleaning process, high energy densities provided by pulsed laser provoke abrupt heating-cooling cycles. Material absorption of the laser energy and corresponding heating on the surface could be mathematically expressed by the heat conduction differential equations with either analytical or numerical solutions [115-119]. The temporal shapes of the laser play an important role and the thermal history of the material is significantly influenced by it. Compared with analytical solutions, FEM (numerical) is able to apply to complex geometry. Its calculation progress is theoretically expressed as a numerical approach of partial differential equations (PDE) using integral equations and proper boundary conditions [120]. The established literature proved that plasma shielding effect should be considered in the simulation of laser processing involving high intensity laser beam vaporisation of materials, because a large amount of electrons, ions and excited neutrals coexisting would absorb the laser energy and form a plasma cloud above the target surface, which may partially or fully block the energy input from the laser beam [121,122].

On the other hand, it is noted that tiny transparent particle contaminants interact with

laser light differently with thin film contaminants, and it is well known that small transparent particle contaminants could manifest unique near field effects such as lens focusing [102,123,124]. Luk'yanchuk and Zheng et al. have experimentally quantified the influence of near-field effect in dry laser cleaning system, and found it depended on factors of laser wavelength, substrate and particle properties. It is known that this effect could partially explain the problem of the exact solution of light scattering. [104,125]. Meanwhile, this phenomenon was also verified by many previous researchers [126-128]. They found that the distribution of absorbed intensity is the basic input characteristic for the laser cleaning model. Besides, the numerical simulation could be employed to calculate the temperature gradient, distribution of energy intensity and shock pressure during the process of dry laser cleaning or laser shock cleaning by using CFD method [129,130]. Furthermore, Yang and Astratov verified the phenomena of regular attenuation of light intensity and alternate near-field focusing and defocusing effects in microspheres chain through experiments and software simulation [131].

2.13 Slot cleaning

The slot as a normal structure could be observed on many parts or components. In the semiconductor industry a slot is an ideal structure to store data, which always appears on the integrated circuits made by silicon wafer [132]. Mono-crystal silicon wafers are used as the substrate, and photolithography is applied to mark different areas of the substrate to be doped or to have polysilicon, insulators or metal deposition.

Meanwhile, integrated circuits have many overlapping layers. Although the structures of integrated circuit are complicated, thickness of layers remains much thinner than the device widths. Thus photons of higher frequencies typically in ultraviolet range, such as laser, or chemical etching are the commonest methods to create the slot patterns on each layer. The wafer is then cut into rectangular blocks for each integrated circuit [133]. Also, each device is tested before packaging using automated test equipment, so the residues caused by laser patterning or etching must be cleaned. Laser cleaning as a non physical contact technique should be performed to this application. The silicon wafer after fabrication is shown in figure 2.12 [134].

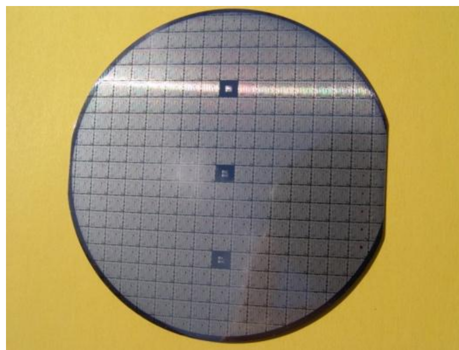

Figure 2.12 The silicon wafer after fabrication [134]

The slotted structures have always been found in the biological research field. Biocompatibility of a material is often related to surface microtopography and micro textures. Since surface topography would affect the nature and the strength of the interactions occurring at the biomaterial-biological host environment, such as protein adsorption, cell deposition, adhesion, mobility, spreading and proliferation, many novel techniques were developed to microfabricate surfaces with well defined and controlled micro structures, which can change surface biocompatibility and cell

adhesion, achieve better control of above phenomena. The slot structures are the normal micro textures to improve biocompatibility performance of material. The processing method for micro slots relies on laser ablation technique using excimer laser [135]. These micro slots could be built on a stent, pacemaker or other devices that is implanted into human body. From the established literature, it is known that these slot structures cause positive inhibition of protein adsorption on the surface of device, as shown in figure 2.13, which benefits to enhance the effect of treatment [135].

Figure 2.13 The surface of stent after micro fabrication for anti-growth of protein [135]

On the other hand, slots are also often found on metal parts. A water cooling system has many channels which effectively enlarge the heat radiation area of part [136]. An example of a CPU water cooling part is shown in figure 2.14 [137]. The rust and oxide layers inside them are difficult to remove by traditionally mechanical techniques. The chemical solution would damage the substrate, and is not friendly to the environment. On the other hand, the chemical solution may pollute the whole

cooling and water circulation system. Laser cleaning keeps the integrity of parts without extra tool cost and avoids risk of secondary pollution.

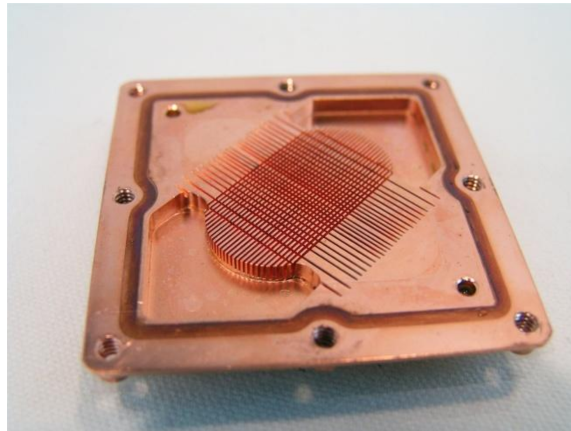

Figure 2.14 The slots on the water cooling transfer part [137]

2.14 Conclusions

For the contaminants with small size or particles its cleaning principle is similar to the model established by Lu [76]. The laser beam that irradiates on the slot sidewall is angularly absorbed by the slot. Meanwhile, if the cleaning target is oxide or the other contaminant layer, its principle approaches to the laser ablation theory, which is reviewed in this chapter.

From this review, it is known that several important achievements of laser cleaning technique have been obtained. The milestone in laser cleaning is summarized in Table 2.1.

Table 2.1 Milestone of laser cleaning technique

Year	Milestone
1916	Albert Einstein established the theoretical foundations for the laser
1928	Rudolf W. Ladenburg confirmed the existences of the phenomena of stimulated emission and negative absorption
1957	Gordon Gould published the term LASER in a paper
1958	Arthur Schawlow and Charles Townes credited with inventation of laser from Columbia University
1960	Theodore H. Maiman operated the first functioning laser
1961	Q-switching allowed short pulses with high power in the nanosecond range
1964	The CO_2 laser was invented by Kumar Patel
1965	The Nd:YAG laser was invented by J.E. Geusic at Bell Laboratory
1966	Laser cleaning was invented by Arthur Schawlow
1970	The Excimer laser was invented by Nicholai Basov’s group
1972	John Asmus applied laser cleaning technique on the conservation of historical building
1974	J. Ewing and Charles Brau invented first rare gas halide excimer at Avco Evert Laboratories
1977	John Madey’s group invented first free electron laser at Stanford Univesity
1987	W. Zapka, Yu. Petrov and S.D. Allen applied laser cleaning technique to the devices in the microelectric field
1988	A.C. Tam further developed steam laser cleaning technique
1989	Y.F. Lu established model for laser cleaning technique
1994	Laser shock cleaning was invented by Ken Watkins, University of Liverpool

Table 2.1 (Continued)

Year	Milestone
2001	Near-field optics was included in the theoretical model of laser cleaning
2004	Laser cleaning technique applied to aerospace engineering field by Laser Processing Research Centre, University of Manchester
2007	SAMULET project started at University of Manchester
2009	The slot cleaning was developed as a project

This literature review shows that there has been no reported work on laser cleaning of slotted components. Thus a knowledge gap exists and new challenges including the identification of laser beam absorption characteristics and contaminant/substrate behaviour in laser cleaning of contaminants in slots (including micro-cracks) of different sizes would be the main focus of this research reported in this thesis.

Chapter 3. Methodology and equipments

3.1 Introduction

This chapter describes the methodology adopted in this research. The experimental procedures and determination of cleaning quality are presented. Several parameters which significantly influence the cleaning effect are listed. Besides this chapter also introduces the material and laser systems used in the experiments and describes their specifications. The characterisation equipment used is included as well.

3.2 Materials

3.2.1 Silicon wafer

Silicon is a chemical element with the symbol Si and atomic number 14. Since most elemental silicon produced remains as ferrosilicon alloy, only a relatively small amount (20%) of the elemental silicon produced is refined to metallurgical grade purity. The fraction of silicon which is further refined to semiconductor purity is estimated at only 15% of the world production of metallurgical grade silicon [138].

Pure monocrystalline silicon is used in electronics and in some high cost and high efficiency photovoltaic applications [139]. In terms of charge conduction, pure silicon is an intrinsic semiconductor which means that unlike metals it conducts electron holes and electrons which may be released from atoms within the crystal by heat, and thus increase the electrical conductance of silicon with higher temperatures. Pure silicon has too low a conductance to be used as a circuit element in electronics

without being doped with small concentrations of certain other elements. This process greatly increases its conductivity and adjusts its electrical response by controlling the number and charge (positive or negative) of activated carriers. Such control is necessary for transistors, solar cells, semiconductor detectors and other semiconductor devices, which are used in the computer industry and other technical applications [140-142].

Presently silicon has become the most popular material to build both high power semiconductors and integrated circuits, because of all the elements, silicon is the semiconductor which can withstand the highest powers and temperatures without becoming dysfunctional due to avalanche breakdown, a process in which an electron avalanche is created by a chain reaction process where heat produces free electrons and holes, which in turn produce more current which produces more heat [143]. In addition, the insulating oxide of silicon is not soluble in water, which gives it an advantage over germanium (an element with similar properties which can also be used in semiconductor devices) in certain type of fabrication techniques [144].

In electronics, a wafer is a thin slice of semiconductor material, such as a silicon crystal, used in the fabrication of integrated circuits and other microdevices [145]. Normally a wafer of monocrystalline silicon serves as a mechanical support for the circuits, which are created by doping, and insulated from each other by thin layers of silicon oxide, an insulator which is easily produced by exposing the element to

oxygen under the proper conditions. The wafer as the substrate for microelectronic devices built in and over the wafer and undergoes many microfabrication process steps, such as doping or ion implantation, etching, deposition of various materials, and photolithographic patterning [146]. Finally the individual microcircuits are diced and packaged. During this process, some tiny contaminants and residues would be left on the substrate. To approach the reality silicon wafer is used extensively as the cleaning substrate in the laser cleaning experiments. The supplier of silicon wafer used in this experiment is Ted Pella, Inc. Their Ultra-Flat 6 inches diameter silicon wafer can also observed by AFM or SEM . The silicon wafer used in experiment is shown in figure 3.1, and its specification of silicon wafer is demonstrated below.

Specification of silicon wafer

Resistivity: 1-10 Ω/cm

Dopant: Boron

Wafer Thickness: 675 +/- 25µm

Front surface: Polished

Back Surface: Etched

Roughness: Typical 2-3 Å

Figure 3.1 The silicon wafer used in this study

3.2.2 Fused silica particle

Fused silica is a glass containing high-purity silica in amorphous (non-crystalline) form [147]. It is different from traditional glasses, in that there are no ingredients added to lower the melt temperature. Fused silica, therefore, has much higher working and melting temperatures.

Fused silica is manufactured by fusing (melting) naturally occurring quartz crystals of high purity at approximately 2000°C, using either an electrically heated furnace (electrically fused) or a gas/oxygen-fuelled furnace (flame fused). Fused silica is normally transparent. The optical and thermal properties of fused quartz are superior to those of other types of glass due to its purity. For these reasons, it finds use in situations such as semiconductor fabrication and laboratory equipment [148]. It has better ultraviolet transmission than most other glasses, and so is used to make lenses and other optics for the ultraviolet spectrum [149]. Its low coefficient of thermal expansion also makes it a useful material for precision mirror substrates.

Fused silica particles provide some particular applications today. Basically they could be frequently used in papermaking, abrasive, and some scientific research applications [150]. Their sizes range from approximately 20 nm to few microns. Ion exchange process is the mainstream for manufacturing of the fused silica particle. Hydrogen ions from the surface of colloidal silica tend to dissociate in aqueous solution, yielding a high negative charge. In this case, the fused silica particles are selected to serve as the contaminants on the substrate. The contaminants found on the silicon wafer usually are transparent. The fused silica has outstanding transmissivity at the wavelength range of ultraviolet light, which benefits the absorption of laser energy on the substrate. The supplier of fused silica particles used in this experiment is Q minerals Co, Ltd. The pureness of SiO_2 is 99.9%, and the particle sizes are 1, 2 and 5 μm.

Before the experiment the turbid liquid mixed by dry particle powder and deionized water was drawn by a syringe firstly, and then dripped and naturally dried on the silicon wafer. The ratio between particle powder and deionized water was carefully measured to make sure that the relatively even monolayer of particles could be obtained due to gravity working on the particles. According to this layering method, the particles of various materials (diameter less than 10 μm) could be attempted to evenly adhere to the silicon surface by Van der Waals force [151]. The fused silica particle used in this study is presented in figure 3.2.

Figure 3.2 Fused silica particle used in this study (a) powder (b) SEM picture for the particle with 1.5 µm diameter manufacturer,supplier

3.2.3 Titanium alloy (Ti6Al4V) and alpha case

Ti6Al4V or Ti64 is the most commonly used titanium alloy. It has a chemical composition of 6% aluminium, 4% vanadium, 0.25% (maximum) iron, 0.2% (maximum) oxygen, and the remainder titanium [152]. The alloy is light weight with extraordinary corrosion resistance and the ability to withstand extreme temperatures. However, the high cost of both raw materials and processing limit their use to military applications, aircraft, spacecraft, medical devices, connecting rods on expensive sports cars and some premium sports equipment and consumer electronics.

Titanium alloys are indispensable engineering materials in modern industrial applications. In addition to light weight and outstanding corrosion resistance, they have very high tensile strength and toughness, extraordinary corrosion resistance, excellent fatigue property and biocompatibility [153-155]. Ti6Al4V alloy, also known as Grade 5 Titanium alloy, is one of the most widely used alloys in the aerospace and medical industries [156-158]. Generally, it is used in applications up to 400°C [159].

At temperatures from 600°C to 1000°C, oxygen diffusion would cause the generation of an oxygen enriched surface layer, known as alpha case titanium, which is hard, brittle and difficult to machine [152,160]. The formation of alpha case titanium surface layer substantially degrades the structural integrity of the titanium alloy, and causes a significant loss of tensile strength and reduction in fatigue performance of the alloy.

Removal of such alpha case layer (typically 100-300 μm), mainly through chemical processes at present, is of great importance in aerospace manufacturing. The chemicals used in the cleaning processes, such as Hydrofluoric acid (HF), are hazardous and unfriendly to the environment [161]. Besides chemical cleaning, some other erosion processes, such as mechanical milling and water jet, have also been attempted but found not as effective as the chemical cleaning method, based on considerations of their removal rate, surface integrity and tooling cost [162,163]. For avoiding these drawbacks an alternative technique could be explored by using laser ablation, because there is no solvents left and it is easy to finish and suitable for automatic processing [164]. From the established literature, it is known that some previous researchers have attempted to use laser to process and modify the surface of Ti6Al4V alloy [165-167]. However, until now there is no report work on laser removal of alpha case titanium layer in the literature, despite of a large number of publications on laser processing of the other films on titanium alloys [168-170]. The author of this thesis investigated laser removal of the alpha case layer from titanium

alloy. The supplier of Ti6Al4V for this experiment is BAE systems. The Titanium alloy sheet used in experiment is shown in figure 3.3.

Figure 3.3 Ti6Al4V alloy sheets used in experiment

3.3 Laser systems

3.3.1 KrF Excimer laser

GSI - Lumonics IPEX800 KrF excimer laser (as shown in figure 3.4) delivers high power ultraviolet beam with 248 nm wavelength, 8-15 ns pulse width, maximum 200 Hz repetition and 80 W average power. The pulse shape of laser could be modified according to the requirement of users. This laser is adopted in this study, because its high peak power and relatively large beam spot size. Using the fused silica convex lens (Thorlab LA4984) with a focal length of 200 mm, this laser provides a rectangular spot (3×1.5 mm^2) with flat top profile at the focusing position. If the cleaning requires the defocusing beam, the spot size could be much larger.

Figure 3.4 GSI - Lumonics IPEX800 KrF excimer laser at LPRC

3.3.2 Nanosecond laser

The nanosecond laser used in this research was Laserline Laserval Violino (as shown in figure 3.5), $Nd:YVO_4$ with a wavelength of 532 nm (green), maximum power 7 W, 7 ns pulse duration and maximum 30 kHz repetition. A three axis galvo head is installed in this laser for accurate scanning. This laser outputs a Gaussian intensity distribution with temporal Gaussian pulse shape. The diameter of beam spot could be down to 55 μm. This laser is used on laser surface patterning and ablation in this study due to its higher peak power and circular beam spot with Gaussian distribution.

Figure 3.5 532 nm Laserval Violino laser at LPRC

3.3.3 Femtosecond laser

The femtosecond laser used in this work was the Coherent Ti-Sapphire laser (as shown in figure 3.6) with a wavelength of 800 nm, average power of 1 W, repetition of 1-2 kHz, pulse duration of 150 femto seconds and a Gaussian intensity distribution. The diameter of laser spot could be focused down to 80 μm spot size, which could be controlled by a galvo head. The super short pulse duration provided by this laser would show some unique characters on the surface ablation and patterning, which could enhance the laser cleaning and ablation effect on the material surface.

Figure 3.6 Ti Sapphire femtosecond laser at LPRC

3.3.4 Pulsed CO_2 laser

The pulsed CO_2 laser used in this study is GSI Lumonics IMPACT 3000 Series (as shown in figure 3.7). It outputs a laser beam with the wavelength of 10.6 μm, pulse duration of 100 ms and maximum repetition rate of 200 Hz. The original output beam size is 19×19 mm^2, and the beam divergence is limited in 6.0 mrad. The pulsed CO_2 laser shows many advantages on the ablation of polymer and glasses in this project.

Figure 3.7 GSI Lumonics IMPACT 3000 pulsed CO_2 laser

3.4 Characterisation equipments

3.4.1 Scanning Electron Microscope (SEM)

The scanning electron microscope (SEM) is a useful characterisation equipment for the research. The multiple signals produced by a SEM include secondary electrons (SE), back-scattered electrons (BSE), characteristic X-rays, cathodoluminescence (CL), specimen current and transmitted electrons. The signals are from interactions of the electron beam with atoms at or near the surface of the sample. Secondary electron imaging of SEM can produce high resolution images of sample surface [171]. SEM micrographs have a large depth of field to characterise three-dimensional data for understanding the surface structure of a sample because of narrow electron beam. High magnifications can be achieved, even more than 500,000 times.

Back-scattered electrons (BSE) are beam electrons that are reflected from the sample by elastic scattering. BSE images can provide information about the distribution of different elements in the sample. For this reason, BSE imaging can apply on the objects which are difficult to detect in secondary electron, especially for biological specimens. Characteristic X-rays are outputted when the electron beam removes an inner shell electron from the sample, which leads a higher-energy electron to fill the shell and release energy. These characteristic X-rays can identify the composition and measure the elements in the sample [172].

The scanning electron microscope (SEM) used in this study is Hitachi High

Technologies (S-3400N) (as shown in figure 3.8) with secondary electron (SE) and back scattered electron (BSE) detectors. Normally the sample in the SEM should be conductive to react with the electrons. Otherwise, the gold coating should be applied on the surface of the sample.

Figure 3.8 Hitachi High Technologies SEM at Photonic Science Institute, University of Manchester

3.4.2 Optical microscope

The optical microscope used in this study is manufactured by Polyvar (as shown in figure 3.9). The optical microscope is equipped what a camera and connected to a computer to store data and pictures. The largest magnification for this optical microscope is 500 times. And the feature with size of 1 μm could be observed clearly.

Figure 3.9 Optical microscope (Polyvar) at LPRC

3.4.3 White light interferometer

White light interferometer (WLI) is a fast non-contact measurement technique for surface topography. The resolution in axial direction achieves to 3 Å, and an resolution in lateral direction is 3 nm. In an interferometer, a light beam is split into two beams. One split beam is reflected from the sample whereas the other split beam is reflected by a reference mirror. When two waves of beam combine, the target pattern is determined by the phase difference between the two waves due to constructive interference. Currently, most interferometries are using a laser as the light source, because long coherence length of laser light makes it easy to obtain interference fringes and interferometer path lengths no longer have to be matched as they do if a short coherence length white light source is used [173,174]. In this work, WYKO NT1100 White Light Interferometer with an axial resolution of less than 1 nm was used. The WYKO is shown in figure 3.10.

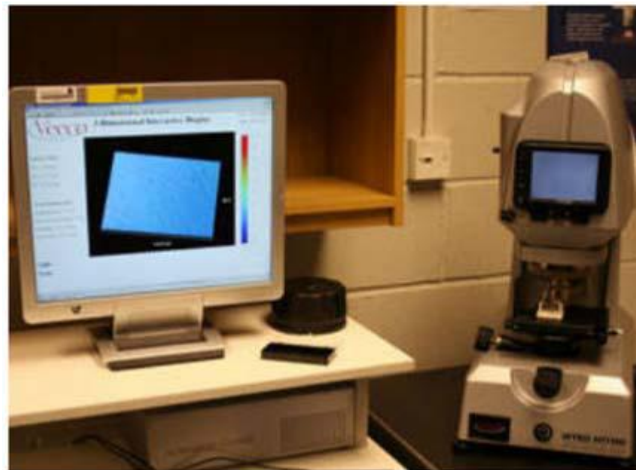

Figure 3.10 White light interferometer WYKO NT1100 at LPRC

3.4.4 Atomic force microscope

Atomic force microscope (AFM) is a contact based characterisation equipment with very high lateral and axial resolution. AFM is a scanning probe microscopy technique which consists of a cantilever and tip coupled with a laser and a detector. During scanning, the AFM tip slides over the sample bending the cantilever according to its profile. When the tip is scanning a sample surface, forces between the tip and the sample lead to a deflection of the cantilever according to Hooke's law [175]. Forces that are measured in AFM include mechanical contact force, van der Waals forces, capillary forces, chemical bonding, electrostatic forces, magnetic forces, Casimir forces, solvation forces. Typically, the deflection is measured using a laser spot reflected from the top surface of the cantilever into a photodiodes. The motion of the laser to the cantilever is calibrated to detect the profile of the sample. The AFM used in this research was Veeco AFM, and it is shown in figure 3.11.

Figure 3.11 Veeco AFM at LPRC

3.4.5 Spectrophotometer

Spectrophotometer is used to measure the optical properties (transmission, absorption and reflection) of a material. These properties are required to establish the percentage of laser energy that would be absorbed, reflected or transmitted by the material. In this research, this equipment had a specific importance because the reflectivity of material plays an important role for the laser cleaning. The real laser absorbed by substrate is known through it. The spectrophotometer used in this work was Ocean optics SD2000 Spectrometer with Integrating Sphere, as shown in figure 3.12.

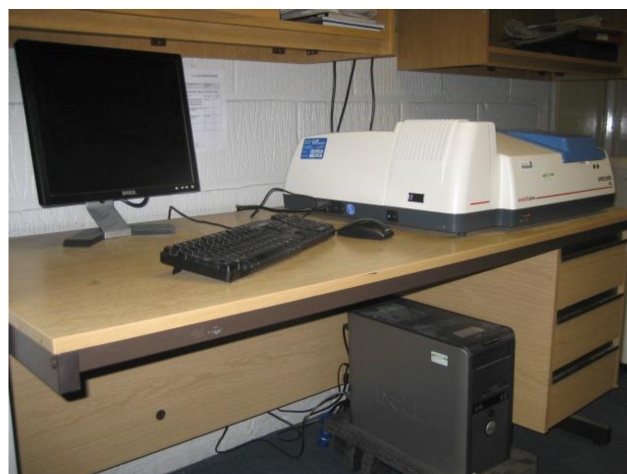

Figure 3.12 Photo spectrometer Ocean optics SD2000

3.5 Commercial software

3.5.1 ANSYS

ANSYS is an engineering simulation software (CAE), and the headquarters of the the company is in Canonsburg, Pennsylvania, United States. Relying on its outstanding performance and powerful solver, it has been used in multiple engineering research fields. It has some famous customer of ANSYS, such as BOEING, BMW, Speedo, all improved the reliability, design and cost of their products with the help of ANSYS [176]. These products cover almost every engineering field, which could be a good proof of performance of ANSYS in multi-physics field. Currently, there are nine basic functions. They are:

- Structural static analysis
- Structural dynamics analysis
- Structural non-linear analysis
- Dynamics analysis
- Thermal analysis
- Electromagnetic analysis
- Fluid dynamics
- Acoustic analysis
- Piezoelectricity analysis

Its thermal and stress modules were used to simulate the process of laser cleaning per pulse. ANSYS provides three basic heat transfer types. They are thermal conductivity,

thermal convection and thermal radiation, and each of them could be independently calculated in static, transient, linear or non-linear modes. Besides, phase change is concerned in thermal-stress coupling field, which is meaningful in the simulation of laser cleaning. The calculation of ANSYS follows the order of preprocessor, solution and general postprocessor. The boundary conditions are loaded in the preprocessor part. Also, the users could select suitable calculation method for their model in solution part. Without extra option, the system would change into non-linear solver for particular models that include phase change. And then the postprocessor is used to analyse the result and plot the required diagrams.

Melting capacity is always the bottleneck of FEM software. The non-linear viscoelastic behaviour of liquid and phase change increase the difficulties of modelling on the melting mechanism. The hydrokinetics can be applied to solve the melting problem region, which solves the phase change and the solid-melt interface tracking problems. A user defined Maxwell constitutive equation is developed with the ANSYS. This constitutive equation can reflect the relaxation time spectrum of liquid melt. The melting process with various vibration parameters can be simulated, and the rule of the influence of frequency and amplitude on melting process is analysed [177].

3.5.2 CST 2011

CST 2011 is a specialist tool for the 3D electromagnetic simulation of high frequency

components. Its unparalleled performance makes it the first choice in many research institutions. CST 2011 enables the fast and accurate analysis of high frequency (HF) devices such as antennas, filters, couplers, planar and multi-layer structures. CST promotes the complete technology for 3D electromagnetic simulation [178]. Users are provided great flexibility in tackling a wide application range through the variety of available solver technologies. Beside, time domain solver and the frequency domain solver could be alternative for the different specific applications. Filters for the import of specific CAD files and the extraction of Simulation Program with Integrated Circuit Emphasis (SPICE) parameters enhance design possibilities and save time [178]. Meanwhile, the calculation results in the CST electromagnetic module could be coupled into its multiphysics module, which is a powerful thermal and mechanical stress analysis tool. The thermal and mechanical data is obtained based on the results in previous electromagnetic calculation.

3.6 Experimental procedures

3.6.1 Beam size measurement

The beam size measurement is very important for the laser cleaning project. It is also related to the quantification of the laser energy on the material surface. In this case, the beam size measurement is finished by the utilization of the photosensitive paper, which is adhered on the material surface which is irradiated by the laser. Its dye reacts with the high photonic energy (laser beam) and fades quickly. For this reason, the projection shape of the laser beam on the target could be clearly recorded. This

measurement method can apply on some angular and axial beam irradiation cases.

3.6.2 Energy measurement

In this study, the magnitudes of energy were measured by an energy meter (Geotech solo SE) which was placed at the defocusing position after convex lens, and their mean values among pulses were recorded as laser output energy. Meanwhile, to obtain the traditional energy intensity unit – fluence (J/cm^2), the ratio of measured magnitude of energy to beam spot size at the target surface should be calculated.

3.6.3 Evaluation of cleaning quality and rate

Compared with the other laser surface techniques, the evaluation of laser cleaning quality would be easier using the characterisation equipments. For some colourful film contaminants, such as paint, ink and some oxide, the cleaning effect can be observed by the naked eye. The integrity of substrate after cleaning should maintain at its original level. Many tiny defects, such as cracks, deformation and colour changes, could be found through observation by an optical microscope. Meanwhile, scanning electron microscopy (SEM) is used to search for tiny contaminants on the substrate because of its relatively higher magnifications.

Cleaning rate, R_c, is defined by the unit (m^2/s), which is related to the beam spot size and its velocity. For keeping the fluence in a moving beam the same as in a stationary beam, the scanning speed (S) for the moving laser beam is related to the number of

pulses in the stationary laser beam (N_s), the frequency of the moving laser beam (v_m) and the length of laser spot size in scanning direction (L_m) by equation (3.1) [179].

$$S = \frac{L_m \times v_m}{N_s} \tag{3.1}$$

The cleaning rate, R_c, is given by [179],

$$R_c = S \times W_m \tag{3.2}$$

where W_m represents the width of laser spot size.

Also, to achieve a complete and regular cleaning area the laser beam ought to overlap to each other. The percentage of laser beam overlap is calculated using the equation (3.3) [179].

$$Laser\ beam\ overlap\% = \frac{Laser\ beam\ size - Offset\ length}{Laser\ beam\ size} \tag{3.3}$$

3.7 Summary

In this chapter, the materials and lasers used in the experiment are introduced firstly. The main processing materials in this project are silicon wafer and Titanium alloy sheet. Four lasers, Excimer laser, femtosecond laser, nanosecond laser and pulsed CO_2 laser, were used to clean the contaminants. The morphology of sample could be presented by the characterisation equipment. Also, the background of two commercial software, ANSYS and CST Studio 2011, is shown. ANSYS is able to calculate the phase change factor during laser processing, and CST Studio 2011 focuses on the coupling function among electromagnetic, thermal and mechanical fields. Several

definitions of experimental parameter, such as beam size measurement, energy measurement and cleaning quality and rate, are shown in the experimental part.

Chapter 4. Laser cleaning of alpha case from Titanium alloy

Abstract

Alpha case (an oxygen enriched alloy layer) is commonly formed in forged titanium alloys during the manufacturing process and it reduces the service life of the materials. This layer is normally removed mechanically or chemically. This chapter reports the feasibility and characteristics of using a short pulsed laser to remove oxygen-enriched alpha case layer from a flat titanium alloy (Ti6Al4V) substrate. The material removal rate, i.e., ablation rate, and ablation threshold of the alpha case titanium were experimentally determined, and compared with those for the removal of bulk Ti6Al4V. Surface morphologies of laser processed alpha case titanium layer, especially that of cracks at different ablated depths, were carefully examined, and also compared with those for Ti6Al4V. It has been shown that in the alpha case layer, laser ablation has always resulted in crack formation while for laser ablation of alpha case free Ti6Al4V layers, cracking was not present. In addition, the surface is rougher within the alpha case layer and becomes smoother (R_a - 110 nm) once the substrate Ti-alloy is reached. The work has demonstrated that laser is a feasible processing tool for removing alpha case Titanium, and could also be used for the rapid detection of the presence of alpha case Titanium on Ti6Al4V surfaces in aerospace applications. This work was published as a peer reviewed journal paper on page 8065-8071, volume 258, Applied Surface Science.

4.1 Introduction

In this chapter, we explore the feasibility and characteristics of using a nanosecond pulsed laser to remove alpha case titanium formed on a titanium alloy (Ti6Al4V) substrate. The material removal rate, i.e., ablation rate, and ablation threshold, of alpha case titanium were experimentally determined, and compared with those for Ti6Al4V. The surface roughnesses at various ablation depths were also measured in the experiments. Surface morphologies of laser processed alpha case titanium layer, especially the characteristics (width and density) of cracks at different ablation depths, were examined, which were compared with those for the substrate Ti6Al4V. In addition, some empirical expressions were derived to predict the thickness of alpha case layer based on the changes of surface roughnesses (R_q, R_a) and crack widths.

4.2 Experimental Procedure

A pulsed GSI Lumonics IPEX 848 Excimer laser (τ = 15 ns, λ = 248 nm, f_{max} = 200 Hz) was used as the laser source. The laser beam with flat top profile was reflected by a mirror and then passed through a rectangular beam-shaping mask (10×5 mm^2), and finally focused by a convex lens with a focal length of 100 mm which provided the laser spot size of 3×1.5 mm^2 on the target surface. The sample was placed with its surface facing vertically to the beam path and its position was controlled by a CNC motion stage (Aerotech A3200). The alpha case titanium sample was obtained by heat treatment of Ti6Al4V alloy inside a high temperature furnace for 24 hours at 800°C. To measure the alpha case layer thickness, the sample was sectioned and etched by

Kroll's reagent (2% HF, 6% HNO_3 and 92% H_2O) for 20 seconds, which provided a clear optical contrast between the alpha case and the Ti6Al4V substrate under the optical microscopic examination (Keyence VHX-500F 3D microscope). Using this method, the alpha case layer grown in furnace was determined to be 60 μm in thickness, and the surface hardness approximated to 800 Hv. Meanwhile, the ablation depth was also measured by Keyence VHX-500F 3D microscope, with its built-in depth composition software function. The data of ablation depth could be outputted and divide to the pulse number to achieve the ablation rate (ablation depth per pulse).

In this study, the measurement of laser fluence was based on following steps. Firstly, the output laser energy (J) was measured by energy meter (Geotech solo SE). Secondly, a laser sensitive paper was used for mapping of the beam spot size. Thus, the fluence was calculated relying on the result that output laser energy (J) divided the spot size (cm^2). Considering the fluctuation of laser output energy per pulse and the error of spot size measurement, the calculation error of the laser fluence was about 5%. Optical reflectivity of the sample surface was measured by Ocean optics SD2000 spectrometer with an integrating sphere. For the accurate control of input laser energy the reflectivities of alpha case and Ti6Al4V alloy at wavelength of 248 nm were experimentally measured to be 8.72% and 17.73% respectively.

Two sets of laser processing experiments were performed. First, the ablation rate of alpha case titanium and Ti6Al4V were determined at laser fluences between 0.3 to

18.0 J/cm^2. The fixed pulse number mode of GSI Lumonics IPEX 848 Excimer laser was employed in this experiment. The laser machine could automatically count the pulses that irradiated to the target till the setup number was reached. For relatively low fluence range (below 4.0 J/cm^2, repetition rate: 50 Hz) the pulse number was set to 230 to minimize the error of depth measurement of 3D microscope. Meanwhile, for relatively high fluence (above 4.0 J/cm^2, repetition rate: 50 Hz) the pulse number was reduced to 200 to avoid full penetration of the alpha case layer material (about 60 µm thick).

Second, morphologies at numerous ablation depths were studied with scanning electron microscopy (SEM, Hitachi S-3400N) for samples treated by a stationary beam at a laser fluence of 5.2 J/cm^2 (repetition rate: 50 Hz). The information of crack widths and densities was collected from the central zone of the laser irradiation area. In this study, multiple SEM images with same magnification (1000x) were taken at several typical ablation depths. Due to the fact that various cracks with different widths were presented at the same depth, the crack width at particular depth was defined as the largest width of crack shown in every image at that depth. Also, the crack density (per mm^2) could be mathematically deduced based on the number of cracks in unit image square (magnification 1000x) at particular depth.

The 3D surface tomography and surface roughness data were obtained by a white light interferometer (MicroXAM surface mapping microscope). In addition, nano-

indentation measurement (MTS Nano indentater) was used to determine the hardness of the alpha case layer.

4.3 Results

4.3.1 Ablation rate

Figure 4.1 (a) shows the ablation rates of the alpha case and the Ti6Al4V alloy at different laser fluences. It is found that the Ti6Al4V alloy has a higher removal rate compared to that of the alpha case layer in the experimental laser fluence range. The ablation thresholds are approximately 1.0 J/cm^2 for the alpha case layer and 0.7 J/cm^2 for Ti6Al4V alloy (error of laser fluence measurement is about 5%). The ablation rates of alpha case and Ti6Al4V alloy climbed rapidly with fluences above 4.0 J/cm^2. It was observed that the differences between ablation rates of two materials widened as the laser fluence was above 10.0 J/cm^2.

To illustrate the processing effect and verify the ablation rate at other pulse numbers, Figure 4.1 (b) shows the cross sections of the alpha case sample after 900 pulses of laser radiation with a fluence of 6.1 J/cm^2. The samples were etched with Kroll's reagent (2% HF, 6% HNO_3 and 92% H_2O) to make the alpha case layer visible prior to the optical microscopic examination. The alpha case layer turned into a bright white colour during this process, and can be clearly observed with an optical microscope. From figure 4.1 (b), it is seen that an approximate 60 μm thick alpha case layer was completely removed, and the substrate of Titanium alloy was revealed.

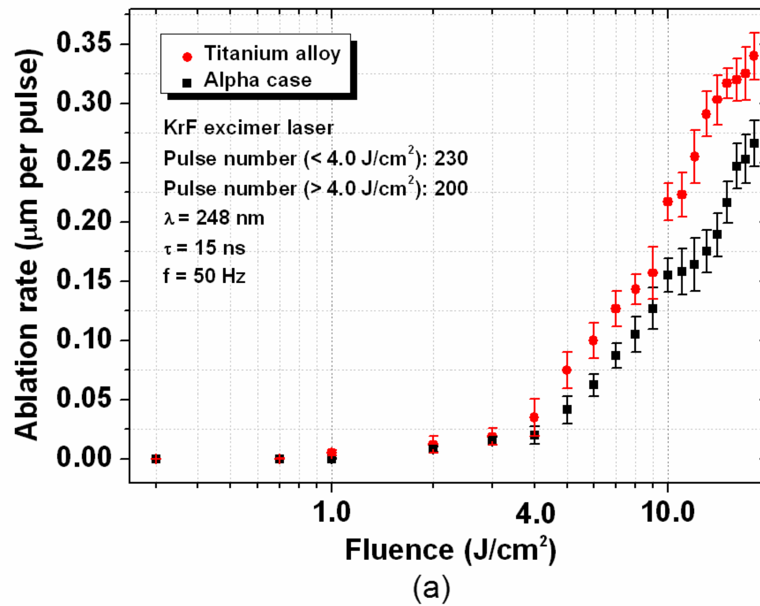

(a)

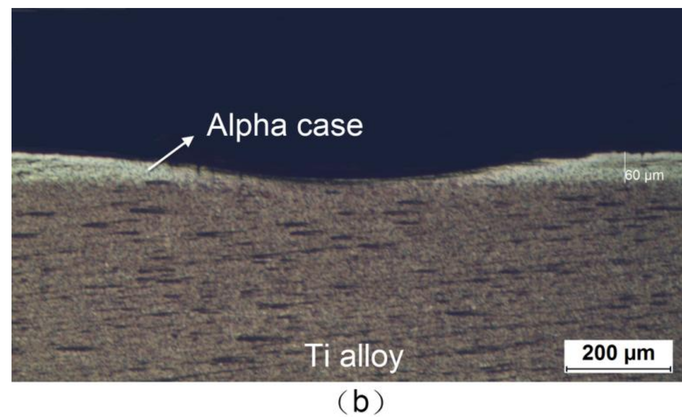

(b)

Figure 4.1 (a) Ablation rate of alpha case titanium and Ti6Al4V alloy at various laser fluences (b) Cross sections of the alpha case samples after 900 pulses of laser radiation with a fluence of 6.1 J/cm^2.

Material removal rate (MRR) is a common value to assess the removal processing technique, whose definition is given

$$MRR = \frac{ablation\ rate \times spot\ size \times pulse\ number}{processing\ time} \tag{4.1}$$

According to the data of ablation rate and aforementioned laser setup, the MRR of laser ablation of the alpha case titanium was 8.1 mm^3/min for the laser fluence of 10

J/cm^2, and 14.8 mm^3/min for the laser fluence of 18 J/cm^2, which is much higher than those for the chemical processing and mechanical milling [161,162].

4.3.2 Morphology

Figure 4.2 shows the morphology of ablated surfaces of the alpha case layers at different depths. All the samples in this group of experiments were ablated at a laser fluence of 5.2 J/cm^2. From the structural schematic – figure 4.2 (a), it is known that the thickness of alpha case layer is about 64 μm, and maximum ablation depth in this group of experiment was 72 μm. Six typical depths - 4, 15, 30, 45, 60 and 72 μm (marked as a-f) are illustrated schematically in figure 4.2 (a), which are selected to demonstrate morphologies of ablation surface of alpha case by using the SEM, as shown in figure 4.2 (b) (1-6). From figure 4.2 (b) (1-4), it is clear that the ablation surface of the alpha case is rough. Multiple sized cracks obviously appear on the ablation surface at the depth a, b, c and d, and their widths shown in figure 4.2 (b) (1-4) are 2.22, 1.7, 0.89 and 0.50 μm respectively. However, the aforementioned characters are not found on the ablated surface at depth e (figure 4.2 (b) (5)) which is at the interface between the alpha case layer and the substrate Ti6Al4V. It is found that their ablation surfaces are flat, even and crack-free, which is completely different from the morphologies seen for laser ablated alpha case layers. In fact, the same characters also appear on the morphology of depth f, as shown in figure 4.2 (b) (6), which is beyond the thickness of alpha case layer into titanium alloy substrate.

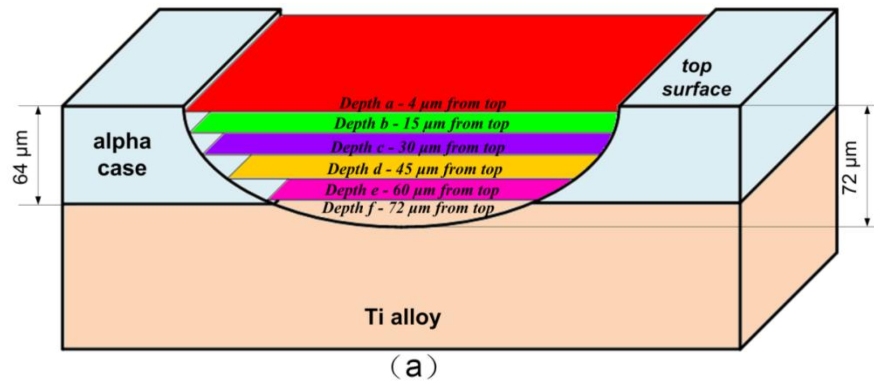

(b)

Figure 4.2 (a) Structural schematic of cross section of sample after laser irradiation (b) Morphologies of ablation surface of alpha case at multiple depths (1-6)

It has been observed that as the ablation depth is close to the boundary between the alpha case layer and the Ti6Al4V substrate, morphology of alpha case starts to gradually approach to the ablated surface morphology of Ti6Al4V alloy. Figure 4.3 (a,b) shows the morphologies of an excimer laser ablated surface of Ti6Al4V alloy sample without an alpha case layer at 4 and 70 μm depth with 1000x magnification. It is noted that all morphologies in this depth range demonstrate the same characters – flat, even and crack-free, which agrees with the finding in figure 4.2.

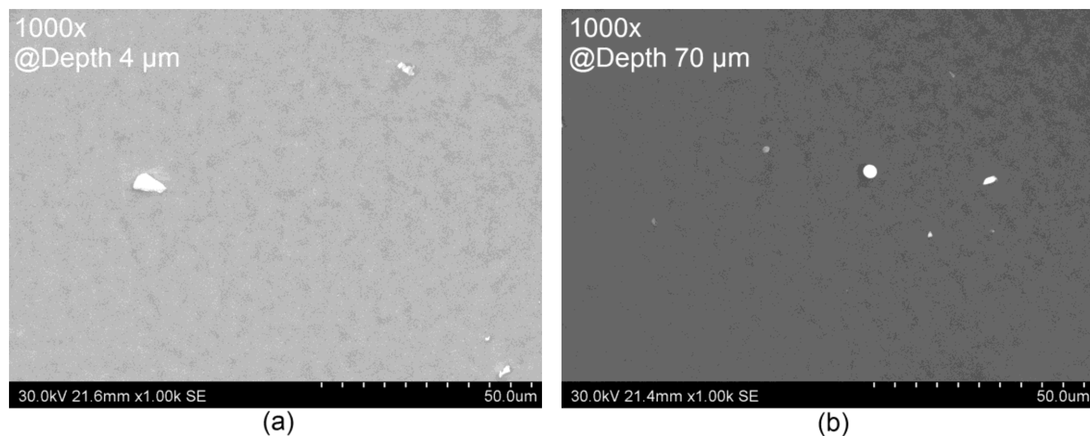

Figure 4.3 Morphologies of ablation surface of Ti6Al4V alloy at depths (a) 4 μm (b) 70 μm

Meanwhile, the 3D micrographs of the ablated surface at depths a-f are captured by the white light interferometer (measurement dimension 160×125 μm^2). Figure 4.4 (a) provides the complete surface roughness (R_a, R_q) of ablation surface in the alpha case layer as a function of the ablation depth. It indicates that the surface roughness of the ablated surface of the alpha case layer has an obvious decreasing trend with the growth of depth. At the surface layer (depth a, b) where relatively wide cracks are visible, surface roughness values are obviously higher than those at depths c and d

where tiny cracks still appear. Once the ablation depth approaches or exceeds the thickness of alpha case layer, such as depths e and f, R_a and R_q could be below 0.2 μm. The 3D micrograph of the ablated surface at depth f is illustrated in figure 4.4 (b). Its surface roughnesses (R_a = 0.11 μm, R_q = 0.13 μm) are much lower than those for the other existing techniques for removal of alpha case titanium. From the literature, it is known that the surface roughness range could be from 1.5 to 13.5 μm. [151,162,163].

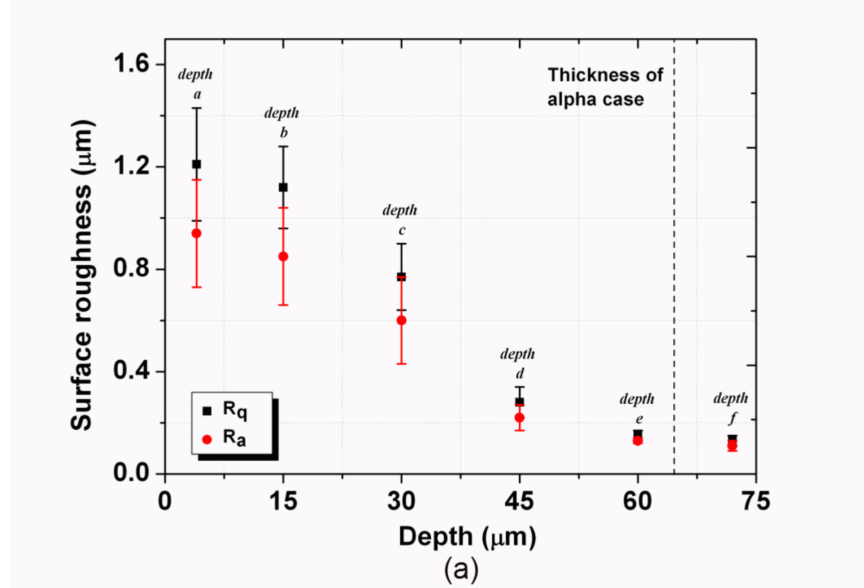

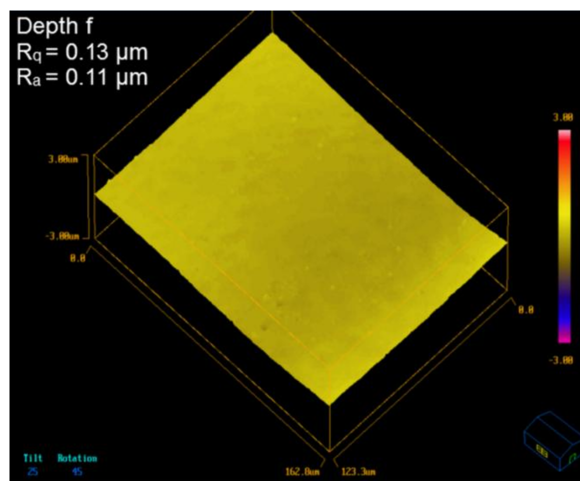

Figure 4.4 (a) Surface roughness (R_a, R_q) of ablated surface in the alpha case layer as a function of the ablation depth. (b) 3D micrographs of ablation surface captured by white light interferometer at depth f

4.4. Discussion

4.4.1 Cracks and surface finish

It is emphasised that the behaviours of cracks on the alpha case ablation surface follow some trends, which can be summarized using hardness of alpha case layer, crack width and density, as shown in figure 4.5.

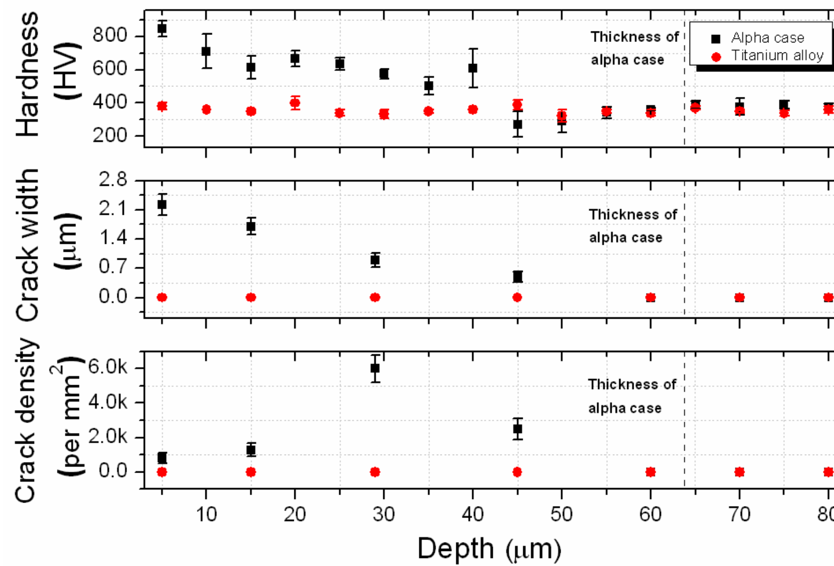

Figure 4.5 Relationship between the hardness of alpha case, crack widths and densities against depth

Based on the nanoindentation measurement on the cross section, hardness of alpha case layer and Ti6Al4V alloy are presented as a function of depth. The Ti6Al4V alloy substrate as a uniform material has a steady hardness value along the depth, which is approximately 350 Hv. However, it is known that the hardness of the alpha case layer is not as uniform as that in the Ti6Al4V alloy, and an obvious decrease trend is shown in figure 4.5, which agrees with the previous findings [180]. The upper surface is the

hardest part in the alpha case layer, with more than 800 Hv at the 4 μm depth. The largest hardness decrease from about 600 to 300 Hv is observed at the 40 μm depth. Then the hardness range of alpha case layer maintains this level further towards the substrate, and approaches to the hardness of Ti6Al4V alloy, as shown in figure 4.5. From the crack width characteristics shown in figure 4.5 an obvious downtrend is found with increasing depth. It is clear that the crack width is more than 2 μm when the depth is less than 10 μm, and gradually drops to below 1 μm at around 30 μm depth. Finally the tiniest cracks were found on the 45 μm deep ablated surface. Its width is only approximate 500 nm. Beyond this depth, the ablation surface of alpha case is crack-free as the case with the Ti6Al4V alloy, as shown in figure 4.5. The number of cracks in a unit area (per mm^2) was collected and analysed from the morphologies of the alpha case layers. It has an obvious trend and relates to the crack width and the corresponding ablation depth. It was observed that larger crack widths near the top surface always corresponded to a lower density. For a crack width of 2.2 μm at the 4 μm depth, the crack density is only approximate 792 per mm^2. However, crack density increases very quickly with the decrease of crack width. The maximum is nearly 6000 per mm^2 at around 30 μm depth. Then crack density reduces after this peak, finally approaches to 0 at 60 μm depth.

The surface morphology and corresponding roughness of the irradiated areas depend on the physical and chemical properties of the material [181]. Two typical properties that most dramatically affect the morphology of laser ablated surfaces are the thermal

absorption coefficient and thermal conductivity [182]. Non-homogeneity of these properties complicates the surface roughness distribution along the ablation depth, as shown in figure 4.4, especially in the high temperature environment. Also, it is found that many cracks were initiated at the material boundaries of components which have different properties [183,184]. In the alpha case ablation investigation, theoretically more oxygen elements dissolve on the upper layer of alpha case [185]. For this reason, alpha case layer is brittle and cannot be considered as a uniform material with the constant thermal and mechanical properties, which would contribute to crack propagation and rough ablated surface due to nonlinear thermal expansion during laser irradiation, and rapid cooling and large thermal gradients following the laser irradiation. Figure 4.4 indicates that the surface roughness is the lowest at the ablation depth around 60 μm. At the same depth the width and density of cracks are down to 0, as shown in figure 4.5. It demonstrates that in the zone that is near to the boundary between the alpha case and the Ti6Al4V alloy substrate there would be little material property change from that of the substrate, because few oxygen elements diffuse in these areas to form alpha case.

Meanwhile, hardness can be considered as an important index to identify the alpha case titanium and normal Ti6Al4V alloy. Other than material homogeneity, changes of mechanical properties also result in cracks on the ablation surface. From the established literature, it is known that the super plastic deformation of titanium alloy at high temperatures is determined by the proportions of the α and β phases, and

relatively equal value usually leads to better performance [186]. At the temperature above the β transus (about 750 °C), titanium alloy contains mostly β phase, which means the standard phase proportion of Ti6Al4V is changed and the material ductility inside alpha case titanium layer declines. Also, rapid cooling of the β phase from above β transus results in the formation of martensite which could make material harder and more brittle [187].

In fact, in the process of laser ablation, the target is separated by two interfaces – vapour and liquid. The liquid interface is generated at the surface and propagates into the bulk during the pulsed laser irradiation. After the termination of the laser pulse, the solid-liquid interface changes direction and recedes to the surface. In addition, as the pulse energy density is further increased, a vaporization interface may also initiate on the surface of the laser irradiated solid [115]. The material whose temperature is above the boiling point transfers into plasma and vapour flume as the output of this process. As an even material with outstanding mechanical performance, Ti6Al4V alloy provides better tensile strength and plastic deformation to overcome the stress initiated by instant shrink during solidification compared with alpha case titanium. Thus its ablation surface could be relatively flat and even and without cracks and bumps, as shown in figure 4.3. In contrast, for the non-ductile material like alpha case, stress relief tends to occur via brittle fracture. The rapid cooling of the material following laser treatment results in induced tensile surface stresses known as thermal shock [182]. Although the alpha case layer shows higher hardness on the top surface,

brittleness, losing tensile ductility and fatigue resistance as the main weaknesses caused by oxygen dissolving lead to crack tips, which would further propagate, due to thermal shock on the ablation face. The resistance of material to thermal shock of laser is expressed by a parameter, $\sigma_{thermal}$, which is a temperature depended thermal stress, given by [188],

$$\sigma_{thermal} = \frac{E\beta\Delta T}{1-\nu} \tag{4.2}$$

where E is Young's modulus, β is the coefficient of thermal expansion and ν is Poisson's ratio. ΔT is the difference between the critical temperature that stresses are released and the atmospheric temperature. From the established literature, it is found that the yield tensile strength of Ti6Al4V alloy is approximate 880 MPa [189]. The morphologies shown indicate that the thermal stress, $\sigma_{thermal}$, initiated by the same laser fluence would not achieve the yield tensile strength of Ti6Al4V alloy, but is higher than the limit of alpha case, especially for its upper layer, which could explain the difference of morphology between the two materials. Meanwhile, the inflection point of hardness of alpha case is around 40 µm depth, as shown in figure 4.5, corresponding with the depth that tiniest cracks appear on the morphology. This phenomenon supports the fact that cracks would significantly relate to the changes of the mechanical property of the alpha case.

4.4.2 Prediction of thickness of alpha case layer

Prediction of thickness of alpha case layer was performed based on the aforementioned analysis of cracks and surface finish after laser irradiation. The

determination of the thickness of alpha case is useful for industrial applications, because related machining parameters are significantly influenced by it. Currently the normal procedure for the measurement of alpha case layer includes: sectioning, grinding, polishing, etching, and measurement of cross section by optical microscopy or electron scanning microscopy. Many disadvantages are shown during this process. Firstly, sectioning breaks the integrity of target. Secondly, a small amount of HF acid is involved in the etching process, which introduces the chemical hazards. Thirdly, processing period and cost inevitably increase. Due to this fact, some previous researchers established the experimental oxidation model to predict the thickness of alpha case layer depending on exposure temperature and time [180,190]. However, most of their experiment and statistics were done at particular temperature and oxygen concentration in lab environments, which limits its application.

In this study, it is known that the crack widths and surface roughness (R_q, R_a) of ablation surface has obvious decrease trend along the growth of ablation depth in the alpha case layer, as shown in figure 4.4 and 4.5. For this reason if establishing the value of crack width, R_q, and R_a as variable, l, the function of thickness of alpha case layer (z_α) could be defined by empirical expressions to fit aforementioned experimental trend. The expression for the surface roughness (R_q, R_a) represented using a variable, l_r, related to the alpha case layer thickness, z_α, is proposed as:

$$z_\alpha = z_0\left(\frac{c_2 - c_1}{l_r - c_1} - 1\right)^{1/p} \tag{4.3}$$

where c_1, c_2, z_0 and p are the constants. Meanwhile, the expression for the alpha case

layer depth in relation to crack width, l_c , is proposed as:

$$z_{\alpha} = \frac{l_c - c_3}{s} \tag{4.4}$$

where c_3 and s are the constants. All the values of constant are listed in Tab.1 for each expression, and corresponding function curves of alpha case layer are illustrated in figure 4.6.

Table 4.1 The values of constants

Items	c_1	c_2	z_0	p	C_3	s
R_q	0.11	1.16	33.02	5.50	-	-
R_a	0.098	0.9	32.67	5.30	-	-
Crack width	-	-	-	-	2.28	-0.04

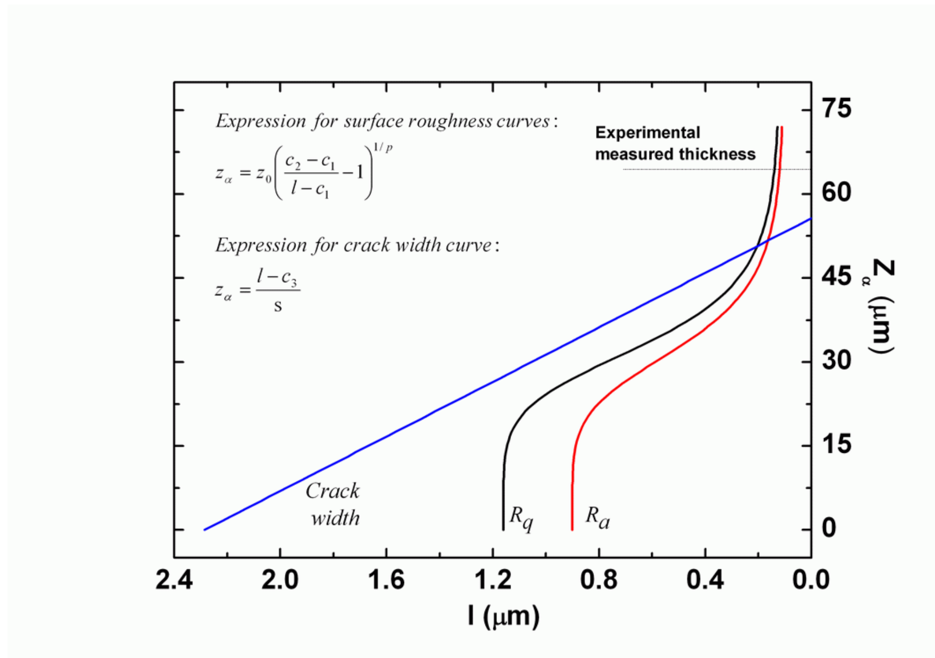

Figure 4.6 Function curves of thickness of alpha case layer

Figure 4.6 indicates that a sharp increase occurs at the two ends of the both curves, which correspond to the experimental result which is that the surface roughness only has small declines around the interface between the alpha case and the Ti6Al4V

substrate. The linear function applies to the empirical expression – equation (4.4) for crack width, because the variable, l_c, (crack width) must be down to 0 finally and the y-intercept ought to appear on the curve, which cannot be solved by the other function forms. Hence, the thickness of alpha case layer predicted by expression by equation (4.3) is the depth that the surface roughness starts being stable, not falling anymore. For the case predicted by expression for crack width, the thickness of alpha case should be the value of y-intercept. For the empirical expressions for R_q, R_a and crack width, the thicknesses of alpha case layer are predicted to 66.5, 68.8 and 58 μm. The experimental measured thickness is about 64 μm, as shown in figure 4.6, and their errors are 3 %, 7.5% and 12.5 % respectively.

4.5 Conclusions

The present work demonstrates a new laser based process that successfully removes alpha case titanium from Ti6Al4V alloy by using pulsed laser irradiation. Corresponding experimental ablation rate of alpha case is compared with that for normal Ti6Al4V alloy. The crack characteristics, surface roughness and hardness change of alpha case varied along the ablation depth. In addition, surface morphology after the laser ablation could be used as a testing method to identify alpha case and measure its thickness due to the specific characteristics of the surface roughness and cracks generated on the ablated surface after laser irradiation. An empirical model was proposed for this measurement.

Chapter 5. Laser cleaning of tiny particles on slot sidewalls

Abstract

The laser cleaning is a rapid developed technique in recent years. However, it is difficult to apply to the slot profile, because the sidewalls cannot absorb enough laser energy. Meanwhile, the focusing lens concentrates the laser beam and energy in a small spot size at the focusing position. The defocused laser beam after the focusing position would disperse and spatially enlarge. In this study, an axial laser beam (Excimer laser, 248 nm) is focused at the position that is slightly in front of the slot (silicon), which makes the defocused beam propagate into the slot and sidewall is able to absorb the laser energy through its dispersion. The slot structure is constructed through three silicon wafers combination (two as side walls, one as bottom). In this manner the slot width can be well controlled during experiment. Using this method, tiny particles (fused silica, diameter 5 μm) adhered on the slot sidewall were successfully cleaned. The cleaning threshold and efficiency for multiple slot widths (3.5 to 13 mm) and pulse numbers (0 to 40) are experimentally determined. A multi-physics model was established to understand the experimental phenomena. The electromagnetic-thermal-mechanical processes during the laser cleaning are also analysed. The paper was published on page 365106, volume 45, Journal of Physics D: Applied Physics.

5.1 Introduction

The transparent particles are usually found on the silicon surface as the residue after chemical etching in semiconductor industry [116]. Laser energy could propagate through them, which boosts the generation of cleaning force due to relatively high absorption on the substrate [191]. Usually, laser cleaning of particle contaminants are realized with sample surface facing vertically to the laser irradiation direction. However, the slot as a common structure widely used in industrial applications is different from the flat surface. Its sidewalls are difficult to absorb enough laser energy to form cleaning force without damaging the bottom of the slot, since the sidewalls are parallel to the laser irradiation direction.

In this study, we explore the feasibility of using an axially defocused Excimer laser beam (λ = 248 nm) to remove the tiny fused silica particles (diameter 5 μm) on the slot sidewalls. The defocused beam after the focusing position propagates into a silicon slot, and successfully removes the particles on the sidewalls. The corresponding cleaning threshold and efficiency for multiple slot widths and pulse numbers are experimentally determined. The surface morphologies of sidewalls before and after cleaning were examined.

5.2 Experimental Procedure

The experimental setup is shown in figure 5.1 (a). A pulsed GSI Lumonics IPEX 848 KrF Excimer laser (τ = 15 ns, λ = 248 nm, f_{max} = 200 Hz) was used as the laser source.

The output axial laser beam was focused by a fused silica convex lens (Thorlab LA4984) with a focal length of 200 mm that provides a rectangular spot (3×1.5 mm^2) with flat top profile at the focusing position which was placed at 2 mm in front of the slot. The laser beam divergence was 1×3 milliradians. The defocused beam propagated into the slot at the same direction. The slot structure was made up by three silicon wafers. Two of them were set to be the sidewalls, and interiors were layered by the tiny fused silica particles with 5 μm diameter. The third wafer became the slot bottom. This is a flexible structure. The slot width, *d*, could be changed through moving the sidewall wafers from 3.5 mm to 6 mm, as shown in figure 5.1 (b).

The fused silica particles are selected to serve as the contaminants on the sidewalls in this study due to its low reflectivity at wavelength of 248 nm and relatively simple layering method. The suspension mixed by dry particle powder and deionized water was drawn by a syringe firstly, and then dripped and naturally dried on the silicon wafer. The monolayer of particles can be readily obtained by controlling the concentrations of the suspension. According to this layering method, the particles of various materials (diameter less than 10 μm) could be attempted to evenly adhere to the silicon surface by Van der Waals force [76,151]. After the experiment, we took apart the structure and the cleaning effect on the side wall could be observed directly.

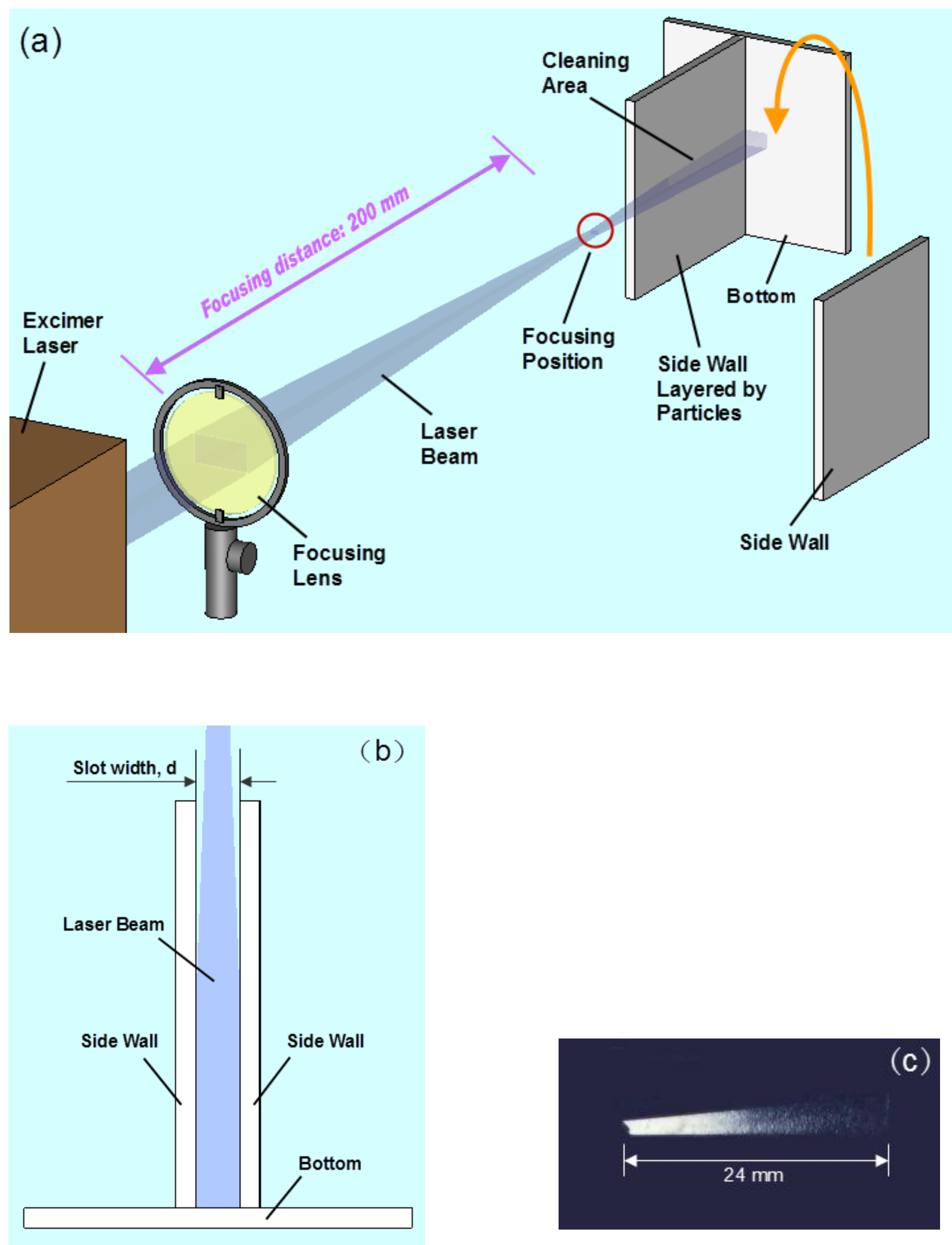

Figure 5.1 (a) The schematic of experiment setup (b) The vertical view schematic of silicon slot (c) The outline for the cleaning area on the side wall of 3.5 mm wide slot

The cleaning area on the sidewalls could be measured by a photosensitive paper which was adhered on the slot sidewall. Its dye would react with the high photonic energy (laser beam) and fade quickly. For this reason, the projection shape of laser

beam on the slot sidewall could be clearly recorded when the beam axially propagated into the slot. The outline of the cleaning area on the sidewalls for 3.5 mm wide slot was shown in figure 5.1 (c). It is shown that there is a regular trapezium with long ends seems like a "comet", which is caused by the laser fluence change on the sidewalls. The length was about 24 mm.

Two sets of experiments were performed. First, the cleaning thresholds (laser pulse number: 50, repetition rate: 50 Hz) for 5 μm diameter particles were determined at the slot width between 3.5 to 13 mm. The magnitudes of energy were measured by an energy meter which was placed at the defocusing position after convex lens, and their mean values among pulses were recorded in thresholds measurement. The slot whose width is smaller than 3.5 mm was not included in this group of experiments, because its dimension is too close to the focal laser spot size (3×1.5 mm^2). The magnitude of laser energy that propagates into the slot significantly reduced in this circumstance. Second, the cleaning efficiency for multiple laser pulse numbers was studied at several particular slot widths. In this experiment, the number of particles in unit area before cleaning was generally counted from the morphological pictures of slot sidewall and considered as 100% remained. The coverage values after laser irradiation with particular pulse numbers would be compared with it. The percentage difference between them was defined as the cleaning efficiency in this paper. Corresponding morphologies on the sidewalls were obtained by the scanning electron microscopy (SEM, Hitachi S-3400N).

5.3 Simulation Process

5.3.1 Model description

A multi-physics numerical model was developed to simulate the cleaning process. A commercial finite integral technique (FIT) software package - CST Microwave Studio 2011 (CST) was used in the study. The electromagnetic intensity field distribution (electric field amplitude) and its power loss were primarily simulated in this case. That part of energy was used as the heat source and coupled into the thermal module in CST. Corresponding transient temperature field distribution could be obtained. From the thermal field results, the cleaning force and simulated cleaning threshold for multiple slot widths are calculated based on a thermal-mechanical model.

5.3.2 Modelling geometry and materials

The particle was assumed to be ideally spherical and transparent in this study. The model dealt with a single particle sitting on the flat sidewall surface. A plane wave laser beam angularly irradiated to the model. Based on the focal length of the convex lens (200 mm) and beam projection size (26×13 mm^2) on the convex lens, the contact angle between laser wave and surface could be calculated using geometrical optics equation. Its value was 3.72°, and related incidence angle was set to 86.28° in CST 2011. The geometric sketch of modelling is illustrated in figure 5.2. The dimension of sidewall substrate (x and y axis directions) were considered as infinity. The optical and thermal properties of fused silica (particle) and silicon (side wall substrate) are summarized in table 5.1 [192-195]. The absorptivity and reflectivity of

material in the model would be automatically calculated in CST 2011 relying on the material optical parameters, *n* (refractive index) and *k* (extinction coefficient).

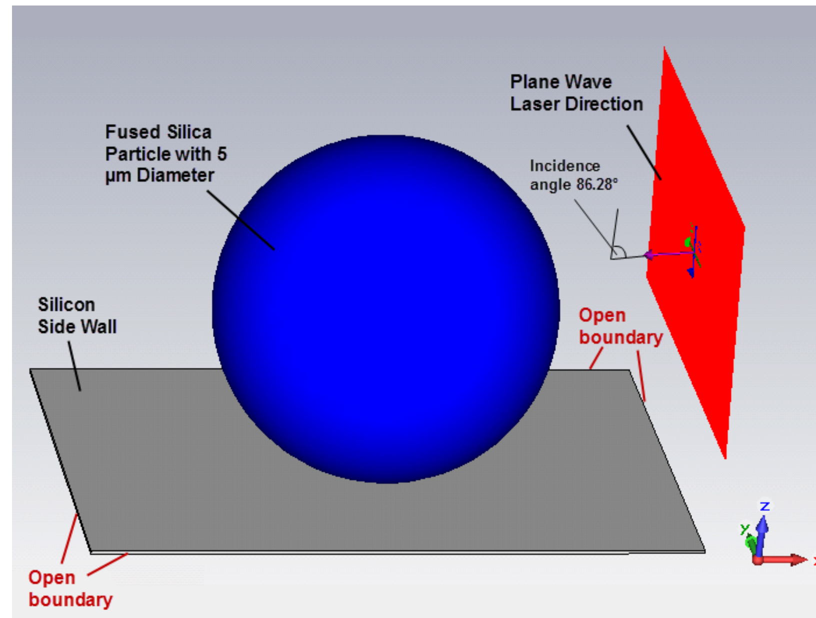

Figure 5.2 The geometric sketch of CST modelling

Table 5.1 Optical and thermal properties of fused silica and silicon [192-195]

Materials	Density, ρ(kg/m^3)	Thermal conductivity, k(W/m K)	Specific heat, C(J/kg K)	Refractive index, n	Extinction coefficient, k_{ext}
Particle: Fused silica	2330	1.3	700	1.51	0.00
Substrate: Silicon	2329	130	860	1.57	3.56

5.3.3 Laser Source: temporal and spatial profile

In this simulation, the laser source was considered to be linearly polarized (y-polarized) light with rectangular flat top spatial profile, a wavelength of 248 nm, and pulse duration of 15 ns. The temporal Gaussian pulse shape for an excimer laser was used in the study [117],

$$I_0(t) = I_0\left(\frac{t}{\tau_0}\right)^{\beta} \exp\left[\beta\left(1 - \frac{t}{\tau_0}\right)\right] \tag{5.1}$$

where $I_0(t)$, I_0 were the intensity of the incident beam at time t, and the peak intensity respectively. The temporal shape factor was defined as β = 1, and pulse duration τ_0 = 15 ns. The spatial profile of flat top beam was given by,

$$I(x, y) = I_0(t) = const. \tag{5.2}$$

where $I(x,y)$ and *const.* were the intensity on the xy plane and output laser energy constant respectively.

5.3.4 Boundary conditions

Unlike most numerical methods, the basic idea of FIT is to apply the Maxwell's equation in an integral form rather than the differential ones [106]. This approach shows advantages due to high flexibility in geometric modelling and boundary handling as well as incorporation of arbitrary material distributions and material properties such as anisotropy, non-linearity and dispersion. To obtain better accuracy on solver Cartesian grids are employed to the current model [196]. Meanwhile, due to the fact that the software is only capable of handling finite size structures, the boundary conditions on the edge of model were defined as open boundary in both electric and thermal modules. The open boundary condition mimics the situation that materials at the computing boundaries extend themselves to the infinite space.

5.4 Results

5.4.1 Cleaning thresholds

Figure 5.3 (a) shows the experimental and simulated cleaning thresholds for multiple slot widths. It is found that both experimental and simulated cleaning thresholds increase with the growth of slot widths, *d*, and form an approximately quadratic dependence. The experimental cleaning threshold for the 3.5 mm wide slot was approximate 21 mJ. However, when the slot width enlarges to 13 mm, it increases to about 330 mJ. The simulated curve well fits the experimental results for the slot whose width is smaller than 9 mm. When slot width is larger than 9 mm, it is observed that the experimental thresholds are 10% higher than the simulated values. The calculation procedure of simulated threshold is clarified in the discussion part.

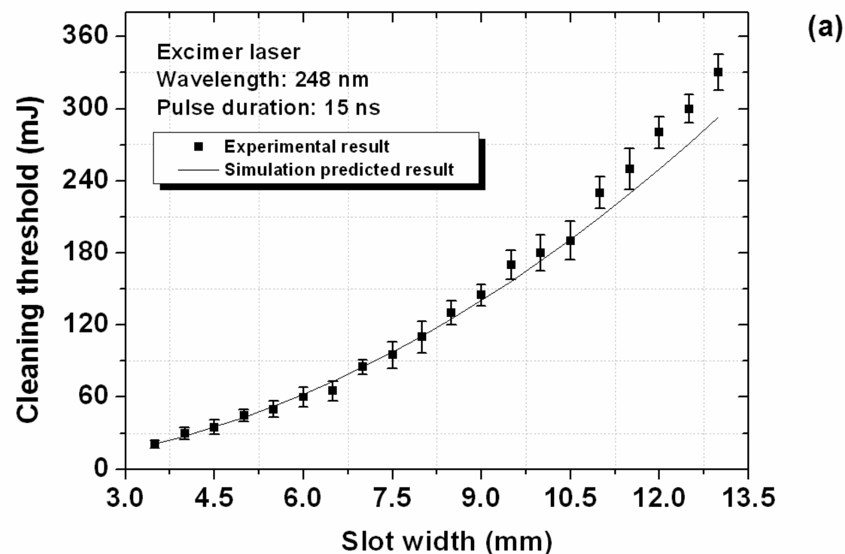

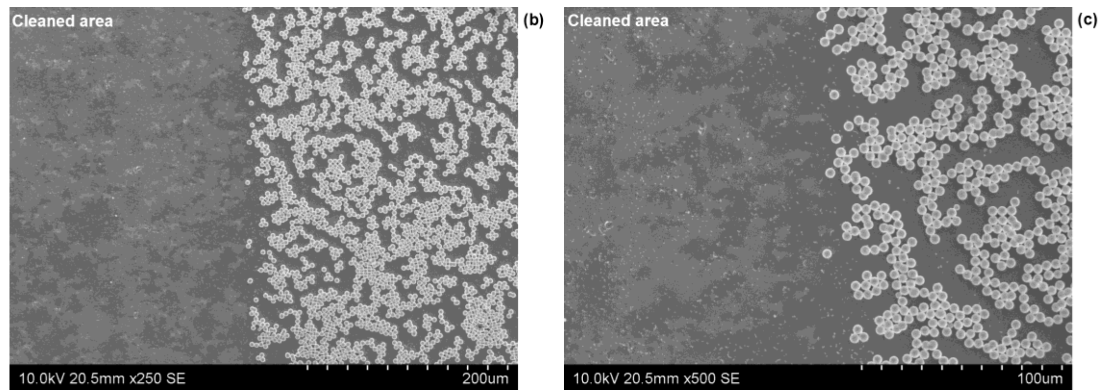

Figure 5.3 (a) The experimental and simulated cleaning thresholds for multiple slot widths. The surface morphologies at the edge of the cleaned area for 60 mJ laser on 6 mm wide slot sidewall with the magnification of (b) 250x and (c) 500x

To illustrate the cleaning effect figure 5.3 (b) and (c) show the surface morphologies at the edge of the cleaned area for 60 mJ laser on 6 mm wide slot side wall with the magnification of 250x and 500x. It is seen that there is no particle left in the laser cleaned area (left side in pictures). In contract the particles with high density are located at the area without laser irradiation (right side in pictures), as shown in figure 5.3 (b) and (c).

5.4.2 Cleaning efficiencies

The figure 5.4 (a) presents that the cleaning efficiencies of multiple laser pulse numbers for 60 mJ output energy on the side wall of 4, 5 and 6 mm wide slots. It is clear that the laser cleaning efficiency increases with the growth of pulse number for all the three slot widths. Under the same laser output energy and pulse number, the slot width plays an important role for the axial laser cleaning. For the same pulse

number the cleaning efficiency of 4 mm slot width is much higher than those for the other two dimensions, and achieves to 100% after the shooting of 15 pulses. The pulse numbers that clean the 100% particles for 5 and 6 mm wide slot approximate to 30 and 40 respectively. The surface morphology of the side wall layered particles for 5 mm wide slot is illustrated in figure 5.4 (b). Under the same conditions, the morphologies of the side wall after 5, 10, 20 and 30 pulses are shown in figure 5.4 (c-f) respectively. It is found that the number of particles decreases gradually till there is no particle at all after 30 laser pulses, as shown in figure 5.4 (f).

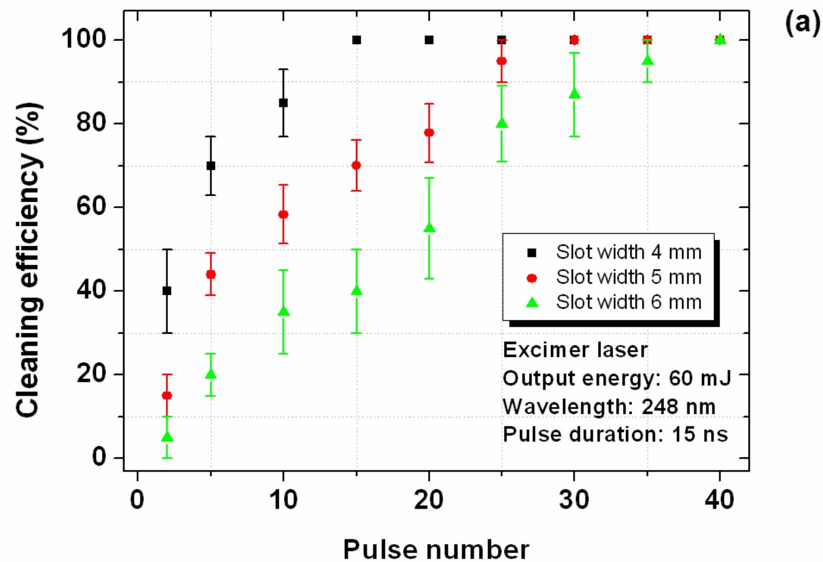

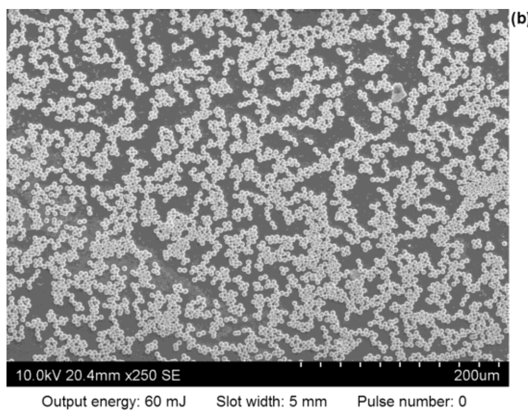

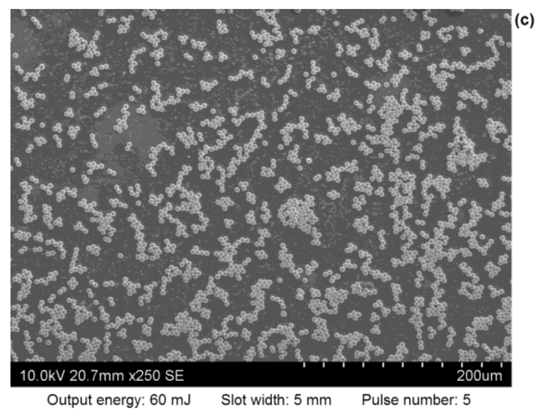

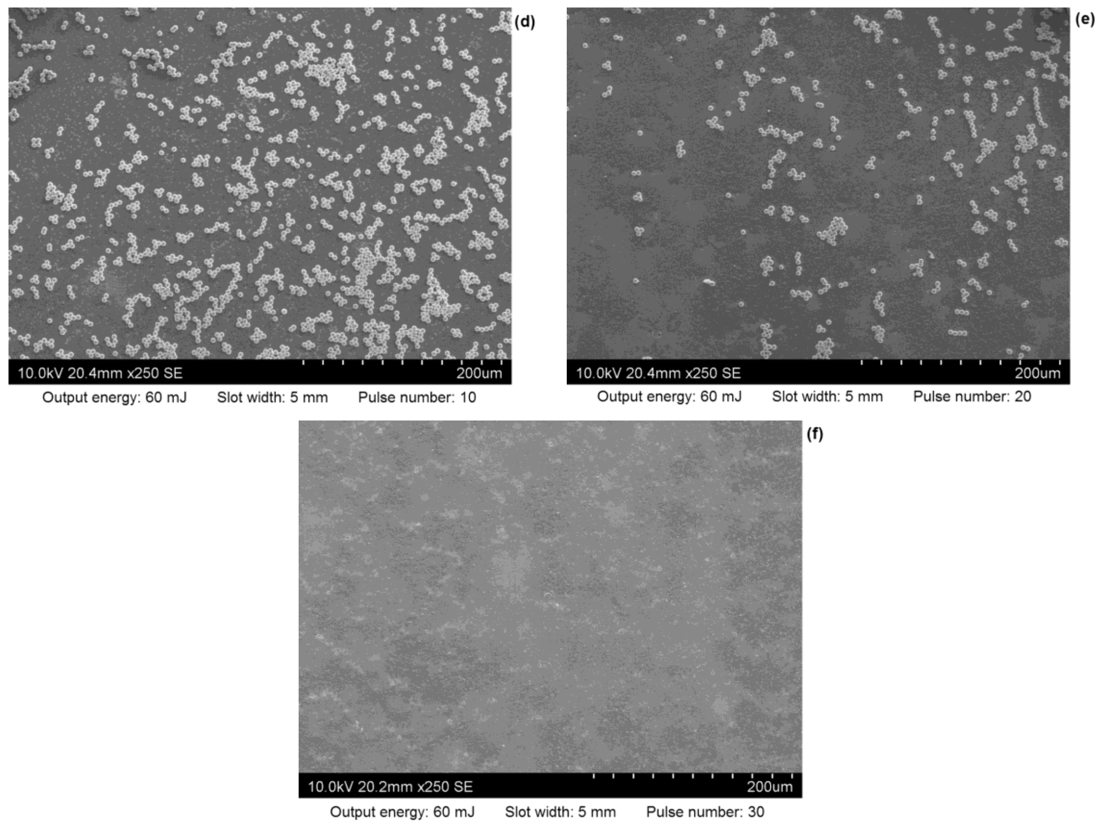

Figure 5.4 (a) Cleaning efficiencies of multiple laser pulse numbers for 60 mJ output energy on the side wall of 4, 5 and 6 mm wide slots. (b) The surface morphology of the side wall layered particles for 5 mm wide slot. (c-f) The surface morphologies of the side wall after 5, 10, 20 and 30 pulses.

5.4.3 Simulation results

Figure 5.5 (a) shows that the electromagnetic distribution of single particle sitting on the silicon sidewall. The electromagnetic module of CST uses the normalized units. The magnitude of input light is set up to 1 unit. The distribution of electric field is normatively mapped in the whole modelling space. It is found that the highest magnitude of electric field intensity is observed at the rear end of particle along the direction of laser propagation, and the largest value achieves to 448 units (not

particle-substrate contacting point), as shown in figure 5.5 (a). The intensity around silicon sidewall substrate and contact point almost keeps the same level with that for input laser light. The outstanding enhancement of intensity is not found in this area.

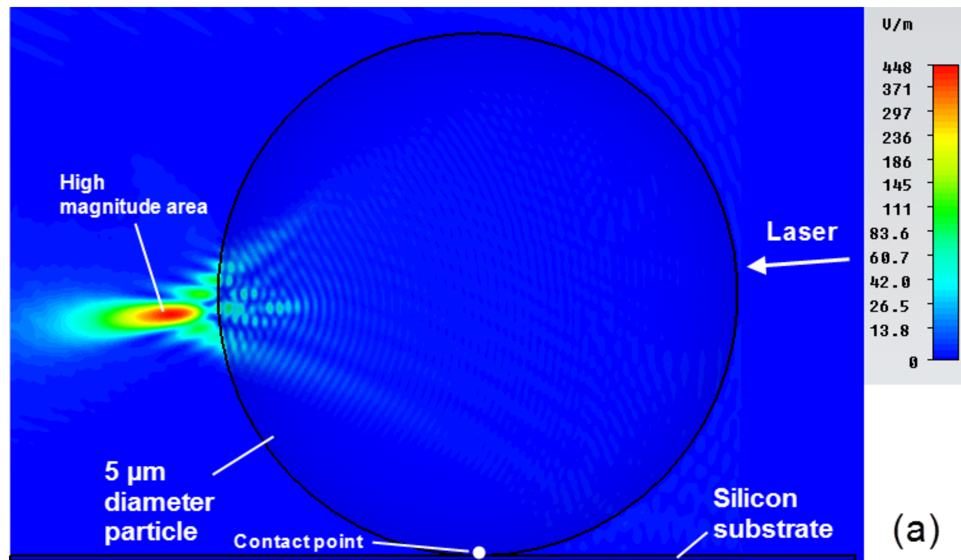

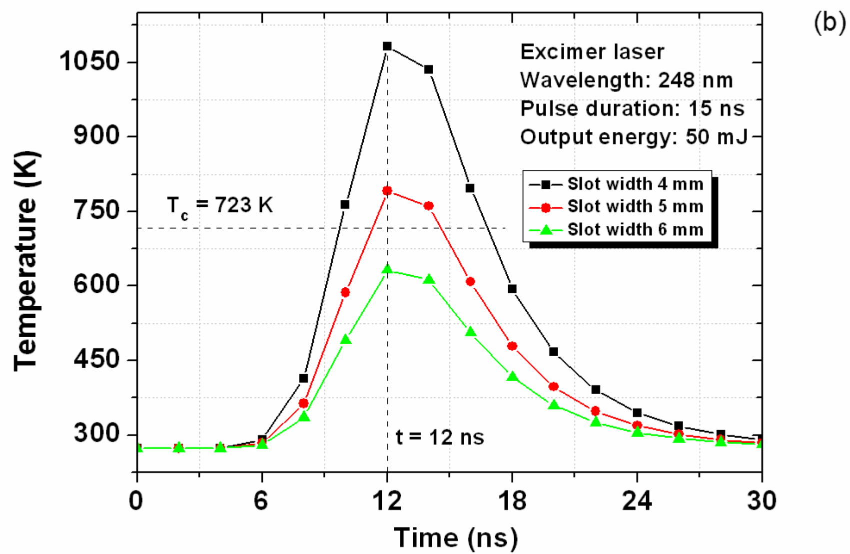

Figure 5.5 (a) Simulated electromagnetic distribution of single particle sitting on the silicon sidewall (b) The temporal temperature rises for the 4, 5 and 6 mm wide slots at the contacting point between the particle and side wall substrate

In this work, the data of electromagnetic field would couple to the thermal module of CST for the analysis of temperature distributions on the sidewalls surface. The laser fluences at the output pulse energy of 50 mJ laser irradiating on the side walls of 4, 5 and 6 mm wide slots are loaded in the thermal module through the corresponding calculated power scaling factors [197]. The equivalent laser fluences under above conditions are 625, 400 and 278 mJ/cm^2 for 4, 5 and 6 mm wide slots, respectively. The related equations and calculation procedure are indicated in discussion part. The figure 5.5 (b) shows the temporal temperature rise for three dimensions at the contacting point between particle and sidewall substrate. From figure 5.5 (b), it is found that the temperature rise of contacting point significantly relates the slot widths. Using the same output laser energy, the peak temperatures for the slots with 4, 5 and 6 mm widths achieves to 1080, 790 and 630 K respectively. All of them are obtained at 12 ns and temperature returns to room temperature after 30 ns. Also, a theoretical calculated temperature, T_c, which could generate minimum temperature rise to get enough cleaning force for 5 μm diameter particle is marked in figure 5.5 (b).

5.5 Discussion

5.5.1 Effect of slot widths and sidewall

It is emphasised that the slot width is an important process condition in axial laser beam cleaning of sidewalls. The size of cleaning area is significantly affected by the slot widths. Wide slots always provide the wider and shorter projection on the sidewall compared with that in relatively narrow slots, which means that the cleaning

area on the side wall of wide slot would not follow the same characters. However, the general shape of cleaning area may not be changed. If the focusing position of lens is fixed, it is observed that the front end of cleaning area would fall gradually with the increase of slot width. The vertical view schematic of this phenomenon is illustrated in figure 5.6 (a), and corresponding experimental effect is shown in figure 5.6 (b) (slot widths 3.5 and 4 mm, paint background). It is known that the axial spot sizes of the laser beam are different for various slot widths and grow with the increase of slot widths. For this reason, the beam needs longer distance to achieve to the side wall of slot with large width, which is considered as the main reason that caused the shift of the front ends of cleaning areas.

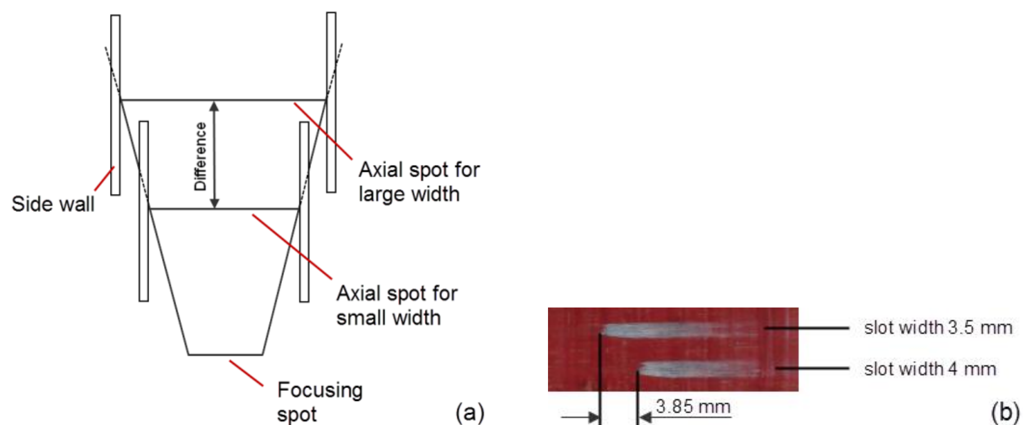

Figure 5.6 (a) Vertical view schematic of cleaning front end for different slot widths (b) The experimental effect of falling phenomenon (slot widths 3.5 and 4 mm, paint background)

This phenomenon also results in the difference of cleaning thresholds for multiple slot widths. From figure 5.3 (a), it is known that the cleaning thresholds increase with

growth of the slot widths. The particles on the sidewall of wide slot require much higher laser energy to be cleaned. In fact, if the output laser energy is a constant, the laser fluence at that particular plane would decline gradually with the enlargement of axial spot size of beam, and be angularly loaded on the particles on the slot side wall. It could be the reason that the cleaning thresholds for wide slots are much higher than those for relatively narrow slots. For our current laser source (GSI Lumonics IPEX 848 Excimer laser), the extreme cleaning slot width is experimentally about 13 mm. The laser fluence in that extreme circumstance could achieve to about 391 mJ/cm^2. Also, in this case, it is known that laser cleaning of slot bottom is similar to the cleaning of flat surface, because the bottom of the slot could absorb most of laser energy. If the damage threshold of the bottom material is known, the laser energy lower than this value should be used, and the slot bottom and sidewalls could be cleaned together. If the damage threshold is unknown, some protection needs to be place on the slot bottom first in case that too high laser energy damages its surface. The common protective idea is using an object to block the laser beam upon the slot bottom. After the cleaning of slot sidewalls, that object could be removed to make the slot bottom cleaned by the lower laser energy.

Meanwhile, from the established literature, it is well known that the laser cleaning of tiny transparent particles is different from that for the film contaminants, because the particles interact with laser light and manifest unique near field effects, such as lens focusing [102,123,124]. Based on this theory, the concentration of laser energy via the

particle would accelerate the ejection of the particle from the substrate and enormously enhance the cleaning force [104,125]. However, from figure 5.5 (a), it is found that the high magnitude area of electric field is along the direction of laser propagation after the focusing of convex lens and far from the substrate. The magnitude of electric field around substrate is still about 1 unit (normalized unit), which is same as the input laser light. Therefore, it is shown that the near-field focusing effect could not provide enhancement for the sidewall cleaning in this case because of its extreme angular irradiation.

5.5.2 Cleaning force

In a dry laser cleaning system, Van der Waals force is thought of the dominant adhesion force for the tiny particles with the diameter less than a few microns [37,76]. The attractive Van der Waals force between an ideal spherical particle and a flat solid surface, F_v, is given by [76],

$$F_v = \frac{hr}{8\pi z^2} \tag{2.8}$$

where r, h and z are the particle radius, the material-dependent Liftshitz-Van der Waals constant and the atomic separation between the particle and surface respectively. As it is the main adhesion force between particle and substrate, the radius of contact area, a, and elastic depth, d, could be deduced by the following equations [37],

$$F_v = \frac{4}{3} E^* r^{1/2} d^{3/2} \tag{5.3}$$

$$a = \sqrt{rd} \tag{5.4}$$

where E^* is the elastic modulus of two bodies, which is given by

$$\frac{1}{E^*} = \frac{1-v_1^{\ 2}}{E_1} + \frac{1-v_2^{\ 2}}{E_2} \tag{5.5}$$

E_1, E_2 and v_1, v_2 are the elastic modulus and Poisson's ratios associated with each part, respectively.

Due to the short pulse laser irradiation (15 ns), there is a rapidly increasing temperature gradient on the substrate, which generates a cleaning force that ejects particles from the substrate surface. Based on the established literature, the equation of dry laser cleaning force per unit area, f_l, and cleaning force, F_c, are given by [76],

$$f_l = \gamma E_s \Delta T(0,t) \tag{2.21}$$

$$F_c = f_l \pi a^2 \tag{5.6}$$

where γ and E_s are the linear thermal expansion coefficient and the elastic modulus of the substrate, respectively. $\Delta T(0, t)$ is the temperature rise at the substrate surface and time t, which is given by $\Delta T(0, t) = T(0, t) - T_0$, where T_0 is the initial temperature at substrate surface. For removal of the tiny particles on the side wall surface the cleaning force, F_c, must be larger than the main adhesion force – Van der Waals force, F_v, which is millions times larger than gravity of particle by calculation [198]. In this work, the radius of particle, r, is 2.5 μm (5 μm diameter particle). Regarding the aforementioned equation (2.8), the Van der Waals force, F_v, is calculated as 0.498×10^{-6} N, and for obtaining preconditions of cleaning, $F_c > F_v$, the $\Delta T(0, t)$ should theoretically achieve to 450 K. The temperature, T_c, as shown in figure 5.5 (b) is deduced from this value and achieves to 723 K. From figure 5.5 (b), it is observed that

the peak temperature of output laser energy of 50 mJ is not above T_c, which means corresponding temperature rise cannot generate enough cleaning force and it is impossible to clean the particles. The experimental cleaning thresholds, as shown in figure 5.3 (a), well correspond to this numerically thermal result.

5.5.3 Prediction of cleaning thresholds

With the help of coupling of CST electromagnetic and thermal modules, the simulation predicted cleaning thresholds for multiple slot widths are calculated in current study based on theoretical deduced $\Delta T(0, t)$ and T_c, as shown in figure 5.5 (b). The CST model could provide corresponding minimum fluence (mJ/cm^2), J_t, to achieve the known T_c. The predicted cleaning threshold of output laser energy (mJ), P_t, is expressed by [48],

$$P_t = J_t S \tag{5.7}$$

Where S is the laser beam size. In fact, due to the fact that the laser beam is restricted in the narrow slot, beam size, S, is decided by the slot width. According to the aspect ratio of original output beam (2:1, 26 × 13 mm^2), it is always presented in the form of

$$S = Slot\ width \times Slot\ width / 2 \tag{5.8}$$

In this case, the minimum cleaning fluences, J_t, is 347 mJ/cm^2. And the P_t values for the slot widths larger than 9 mm are about 10% lower than the experimental thresholds, which could be explained by the fluctuation of the output energy of excimer laser between pulses in the experiment and material properties errors in the modelling [199].

5.6 Conclusions

The present work demonstrates a novel laser cleaning method that successfully removes the tiny particles on the slot sidewalls by using axial beam. Corresponding experimental cleaning thresholds and efficiencies for multiple slot widths are presented, and well supported by an electromagnetic-thermal-mechanical coupled multiphysics model. The cleaning thresholds were found generally increase with slot widths. This work could be applied to laser cleaning of other complex 3D industrial components.

Chapter 6. Multiphysics modelling of dry laser cleaning of micro-slots with particle contaminants

Abstract

Light could interact differently with thin-film contaminants and particle contaminates because of their different surface morphologies. In the case of dry laser cleaning of small transparent particles, it is well known that particles could function like mini-lenses, causing a localized near-field hot spot effect on the cleaning process. This chapter looks into a special, yet important, phenomenon of dry laser cleaning of particles trapped in micro-sized slots. The effects of slot size, particle size, and particle aggregate states in the cleaning process have been theoretically investigated, based on a coupled electromagnetic-thermal-mechanical multi-physics modelling and simulation approach. The study is important for the development and optimization of laser cleaning processes for contamination removal from cracks and slots. This work was published as a peer reviewed journal paper on page 135401, volume 45, Journal of Physics D: Applied Physics.

6.1 Introduction

In this chapter, a multi-physics numerical model is developed to simulate a micro-slot laser cleaning process. A commercial finite integral technique (FIT) software package - CST Microwave Studio 2011 (CST) was used in the study. FIT method has been applied to solving problems in near-field optics previously. The electromagnetic intensity field distributions for varying slot widths and particle aggregate states were simulated and investigated relying on it. Laser energy flows, illustrated by Poynting vector field line plots [200], are presented to visualize and understand the near-field focusing effect inside the micro-slots. The electromagnetic simulation results were used as the heat source and fed into the thermal module in CST. Corresponding transient temperature field distributions were then obtained. From the CST temperature fields, the cleaning forces and cleaning threshold were determined following a well-known thermal-mechanical model.

6.2 Simulation Process

6.2.1 Modelling geometry and materials

The particle contaminants are assumed to be spherical and transparent in this study. The model deals with both single and multiple particles sitting at the bottom of a micro-slot. The length of micro-slot (y axis direction) was considered as infinity. The width of slot (x axis direction) varied from 1 to 5 µm and the depth of the slot (z axis direction) varies between 2 - 8 µm (leaving a one sphere gap from the top). Two sizes of particle (diameter 1 and 2 µm) were investigated in this research, and the geometric

sketches of single, double and triple particle layouts for 1 μm diameter particle are shown in figure 6.1(a-c) respectively.

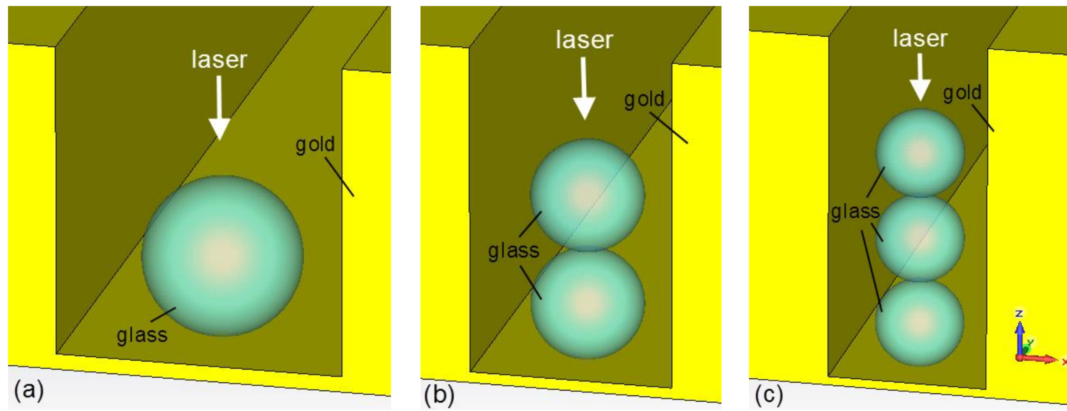

Figure 6.1 Geometric sketches of single (a), double (b) and triple (c) particle layouts for 1 μm diameter particle

In the study, a metallic substrate (gold) and spherical glass micro-particles were selected as the representative modelling system, as gold is used in many aspects of semiconductor manufacturing, particularly in the assembly or packing processes, and glass particle is representative for transparent residue after various manufacturing processes [116,201]. Corresponding thermal and optical properties of these materials at 248 nm wavelength laser are summarized in table 1 [193].

Table 6.1 Optical and thermal properties of the substrate and the particles [193]

Materials	Density, $\rho(kg/m^3)$	Thermal conductivity, k (W/m K)	Specific heat, C (J/kg K)	Refractive index, n	Extinction coefficient, k_{ext}
Particle: Glass	2330	1.3	700	1.51	0.000
Substrate: Gold	19300	318	130	1.484	1.636

6.2.2 Laser Source: temporal and spatial profile

The ultraviolet light irradiated by excimer laser provides higher emission current on the surface, which could enhance the cleaning effect [37]. For this reason, in this simulation, the laser source was considered to be linearly polarized (x-polarized) light irradiated by an excimer laser with rectangular flat top spatial profile, a wavelength of 248 nm, and a pulse duration of 20 ns. The direction of beam was along the z axis direction (top to down), as shown in figure 6.1. The typical spot size is about several square millimetres which covers the whole area of the modelled structure uniformly in xy plane. The typically temporal Gaussian pulse shape for an excimer laser was used in the study [117],

$$I_0(t) = I_0\left(\frac{t}{\tau_0}\right)^{\beta} \exp\left[\beta\left(1-\frac{t}{\tau_0}\right)\right] \tag{5.1}$$

where $I_0(t)$, I_0 are the intensity of the incident beam at time t, and the peak intensity respectively. The temporal shape factor is defined as $\beta=1$, and pulse duration τ_0 =20 ns. As CST can only accept electric field amplitude $|E|$ as laser source input, the peak intensity value I_0 was converted to the amplitude of electric field E by [106]:

$$|E| = \sqrt{\frac{2I_0}{cn\varepsilon_0}} \tag{6.1}$$

Where c is the speed of light in vacuum, n the refractive index of the medium (air in present case) and ε_0 the vacuum permittivity.

By considering that laser fluence (F_0) is related with peak intensity for a pulsed laser with [117]:

$$F_0 = I_0 \tau_0 \tag{6.2}$$

and combining (6.1) and (6.2), gives:

$$|E| = \sqrt{\frac{2F_0}{cn\varepsilon_0\tau_0}} \tag{6.3}$$

which converts the laser fluence, often used by the laser processing community, to electric field amplitude $|E|$ used by the CST software.

6.2.3 Boundary conditions

Due to the fact that the software is only capable of handling finite size structures, the boundary conditions on the edge of model were defined as open boundary in both electric and thermal modules. The open boundary condition mimics the situation that materials at the computing boundaries extend themselves to the infinite space.

6.3 Results and Discussion

6.3.1 Electromagnetic modelling: intensity fields in micro-slots

Figure 6.2 (a) shows the normalized enhancement factor of intensity fields, defined as z-component of time-averaged Poynting vector $I=Re(S_z)$, at the contacting point (Point A as in insets) of particle and substrate for single, double and triple layers of microspheres (diameter d=1.0 μm) located inside different size micro-slots (width $1<S<5$ μm). It can be seen that, regardless of the slot width, single layer particles produce a much stronger focus at the slot bottom surface than those by both the double and triple layers, and triple layers show a stronger focus than double layers. The slot width (S) has clear influences on the focusing fields. For a single layer (1P),

intensity enhancement at the focal point is weak at narrow slot widths 1 μm<S<1.4 μm. The intensity enhancement was boosted at slot width 1.4 μm<S<3 μm with a resonance peak of 32 times of the incoming beam intensity forming at S = 1.8 μm and stabilized to about 26.6 (mean value) with a weak oscillation at slot width S>3 μm. Similar tendency was observed for double layers (2P), with the intensity peak increasing at the slot width S=2.2 μm, and being stabilized to about 7 at slot widths S>3 μm. For the three layer particles (3P), more oscillations were seen within the investigated slot width range. The field intensity peak appeared at slot width around S=2.6 μm. To illustrate the field focusing effects at resonance peaks (P1, P2, P3), the corresponding 2D field distributions in both XZ-planes (across particle centre) and XY-planes (across point A) are presented in figure 6.2 (b-g).

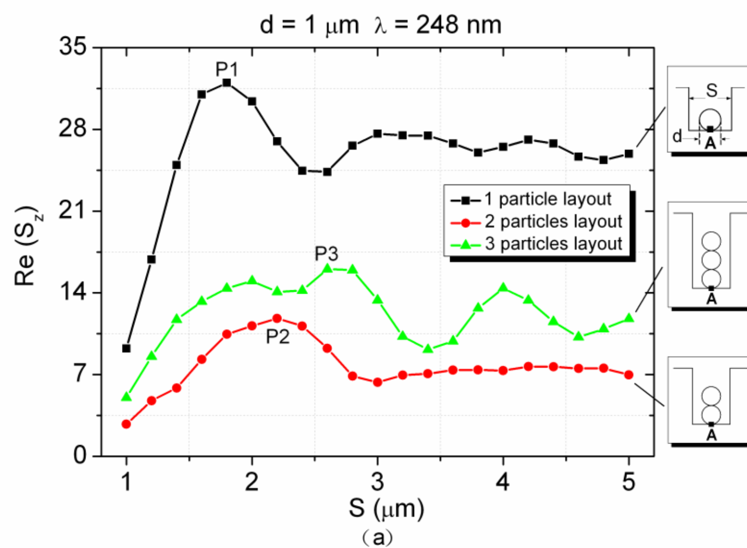

(a)

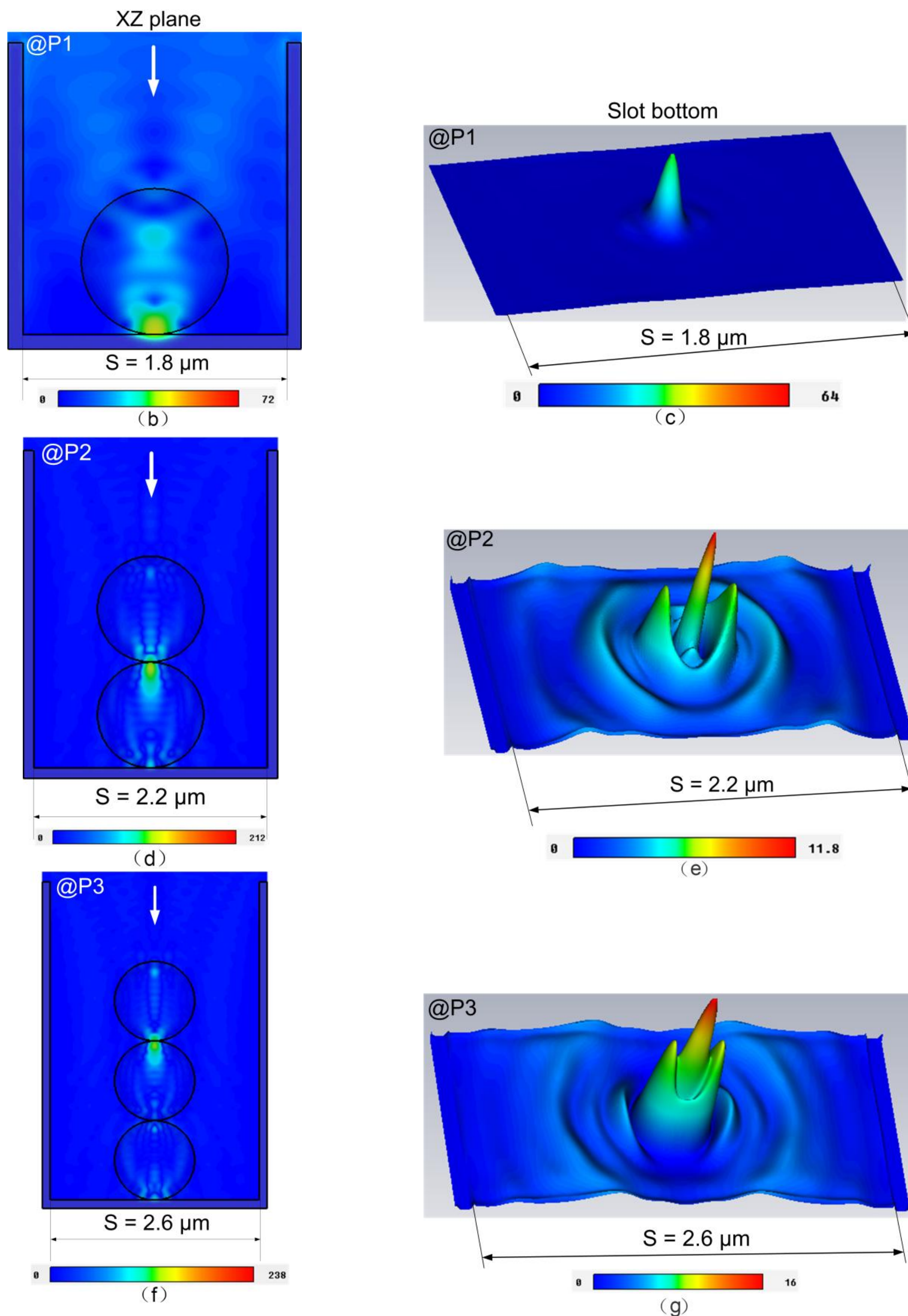

Figure 6.2 (a) Peak intensity on substrate surface beneath 1-um-diameter particles as a function of slot width. (b-g) Corresponding 2D cross-sectional views of the maximum intensity fields in XZ-plane (b,d,f) and XY-plane (c,e,g) for single (P1), double (P2) and triple (P3) layered particles.

Similar to figure 6.2, figure 6.3 shows the results of electromagnetic simulation with exactly the same modelling settings and parameters except that the particle diameter was increased from 1 μm to 2 μm. The single layer particle of 2 μm diameter sphere (figure 6.3(a)) behaves similar to a single 1 μm diameter sphere (figure 6.2(a)) with the main field enhancement within slot width $2.4\ \mu m < S < 3.6\ \mu m$. However, it should be emphasised that the near-field focusing effect of single particle layout for the 2 μm particle is much stronger than the 1 μm particle. The intensity for 2 μm particle is always above 30 with a maximum of 63.44 for slot width S=3 μm (P1 in figure 6.3 (a)). The curve stabilizes to around 40 at the end. For the double and triple layered particles, the graphs show peaks at S=3.8 μm and S=3.2 μm and gradually stabilize to about 5 and 3 respectively along with the increase of slot width. It is found that the stabilized values of double and triple layered 2 μm particles are lower than those for 1 μm particles, as shown in figure 6.2 (a) and figure 6.3 (a).

From figure 6.2 (b) and figure 6.3 (b), it is clear that the focusing point of single particle layout, which has the highest electric field intensity in the three layouts, is close to the substrate. From figure 6.2 (c) and figure 6.3 (c), it can be seen that the highest intensity concentrates at the centre of the slot bottom, which forms the central highest peak, and the height of secondary peaks was found to be lower for the same size particle. These two aspects mean that a better near-field focusing effect was obtained in the single particle layout, which benefits laser cleaning and most of the material processing (micro/nano fabrication) applications [202,203]. Conversely , the

strongest focusing positions of both double and triple particles layout are at the contact point of the first and second particles counting from the top, as shown in figure 6.2 (d,f) and figure 6.3 (d,f), which are far from the substrate. Besides, the phenomenon of multiple secondary peaks or double highest peaks was observed on the intensity field in XY plane for the cases of double and triple particles layouts. The light energy is not entirely focused to the position under the particles. Instead, it decentralizes and spreads in certain areas. The phenomenon is considered to be caused by the interference of particle array and Newton's rings effect [204]. For this reason it would be difficult for the substrate to absorb the focusing energy through the spheres in the multiple particle situations, supported by the fact that the energy intensity values for the multiple particle layouts are much lower than for the single particle layout, as shown in figure 6.2 (a) and figure 6.3 (a). However, by observing distributions shown in figure 6.2 (d,f) and figure 6.3 (d,f), the substrate under the multiple particles layout may still be heated, but the cleaning effect would be weakened. It also demonstrates that the distribution of intensity and the full width at half maximum (FWHM) of the beam on the substrate can be controlled by using different particle arrays, which could be useful for laser patterning applications. Figure 6.3 (b) illustrates that the focusing range of 2 μm diameter particle is much wider than that of the 1 μm diameter one, and more light waves penetrate through the single particle layout, which results in a higher magnitude of intensity in figure 6.3 (a). On the other hand, based on the established literature [129], it is known that light intensity attenuates through microsphere chain. Larger particle accelerates the

defocusing propagation and intensity attenuation in it, which could explain the fact that higher magnitude of intensity is observed on the slot bottom in figure 6.2 (e,g) compared to those in figure 6.3 (e,g).

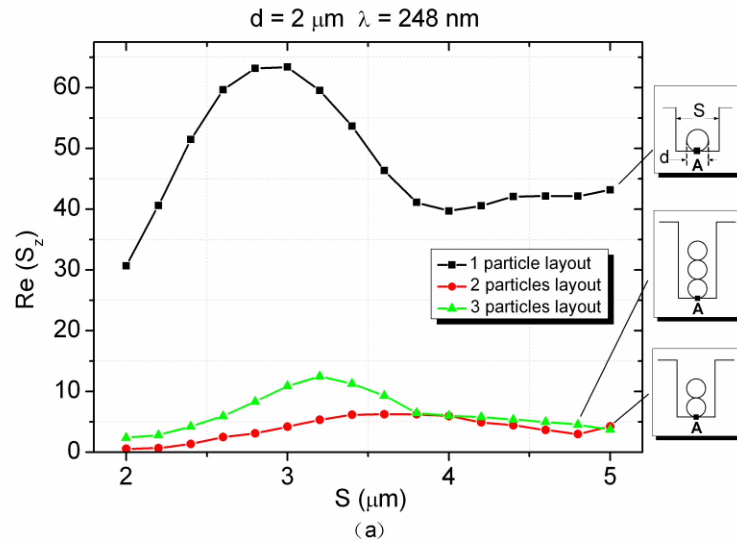

(a)

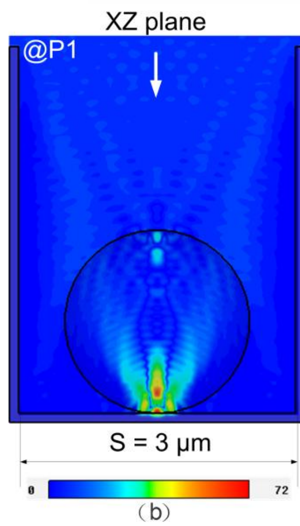

(b)

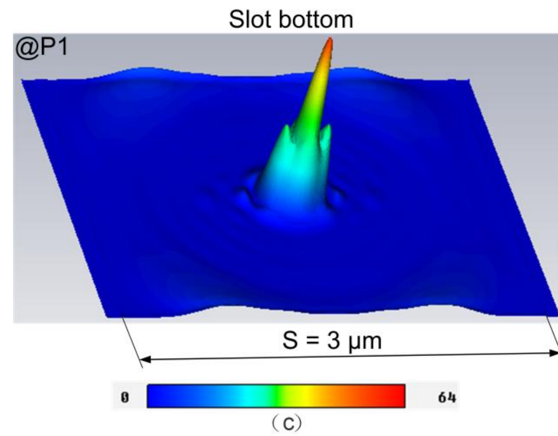

(c)

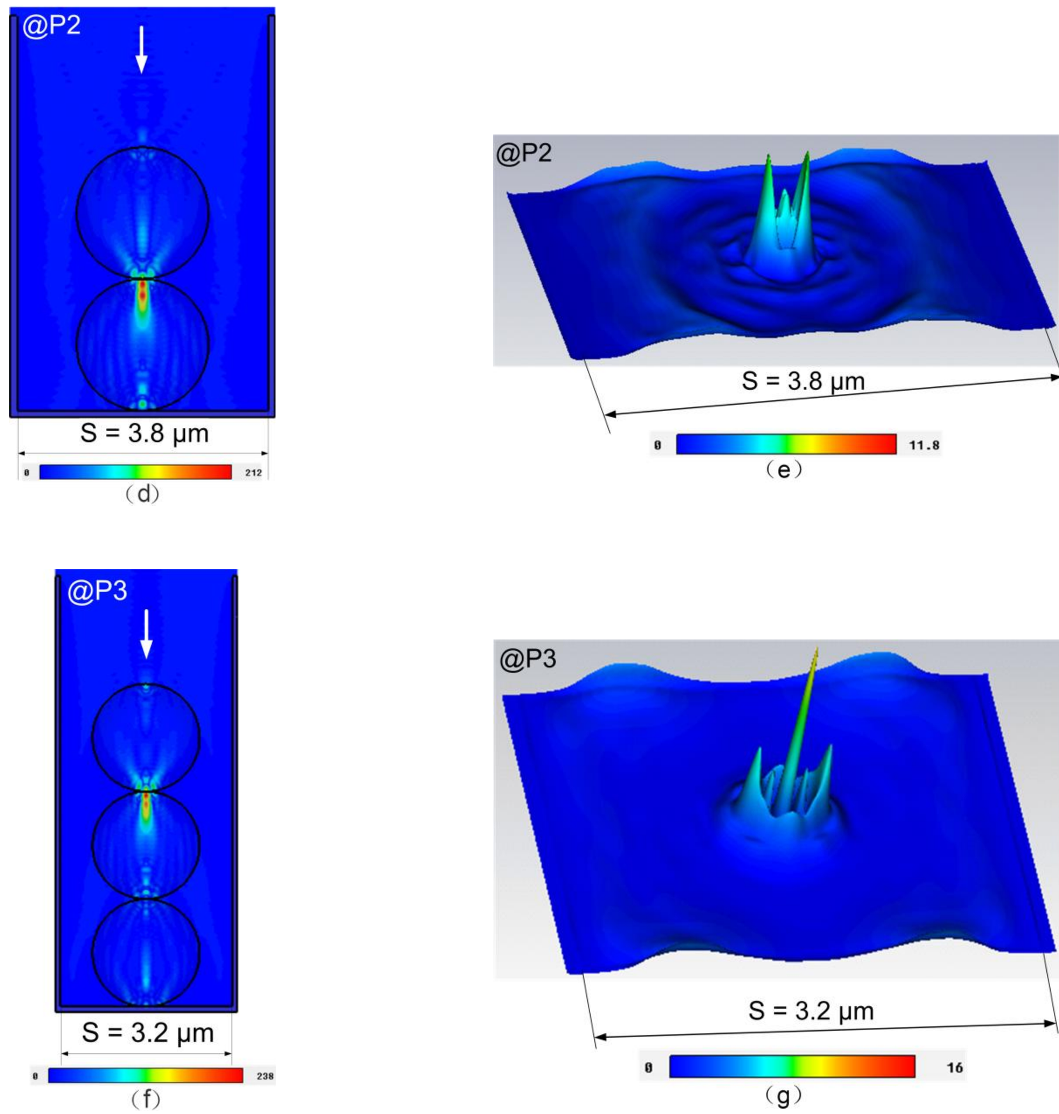

Figure 6.3 (a) Peak intensity on the substrate surface beneath the 2-um-diameter particles as a function of slot width. (b-g) Corresponding to the 2D cross-sectional views of the maximum intensity fields in XZ-plane (b,d,f) and XY-plane (c,e,g) for single (P1), double (P2) and triple (P3) layered particles.

A special phenomenon observed in the multiple particle layouts is that the near-field focusing and defocusing are in alternation with even number of particles producing a defocusing effect and odd number of particles giving a focusing effect at the bottom

of the sphere. For same size particles the focusing effect initiated by odd number of particles provides higher magnitude of intensity and energy level on the slot bottom compared to defocusing effect of even number of particles, as shown in figure 6.2 (a) and figure 6.3 (a). This phenomenon seems to be independent of the slot width. Generally, for the single particle layout the near-field focusing effect is the only optical interaction for this material and sphere size and the focal position is at the bottom of the sphere. In the two particles layout, it is possible for the defocusing effect to happen at the bottom sphere. The defocusing effect is due to the fact that the light focused by the top sphere starts to disperse through the bottom sphere. When the third particle was added into the particle array, the light was focused to the substrate again through the third particle despite the attenuation of intensity during the propagation. This phenomenon was also observed experimentally by Yang and Astratov [131].

6.3.2 Electromagnetic modelling: energy flow visualization

To understand the influence of slot width on the distribution of Poynting vector, the power flow of the single 1 μm diameter particle layout is presented in figure 6.4. From figure 6.4 (a) (slot width equals to the diameter of the sphere), it can be noticed that there are four singular points located in the centre of the sphere. The phase trajectories in the vicinity of the singular points form the clockwise vortexes which are in the relatively low electric intensity areas. It is known that, phase trajectories of the system contain one and a half degree of freedom in the vicinity of singular points,

and related clockwise vortex shape represents a stable focus in the phase space [205]. Also, power flow couples to the other planes through these singular points [206]. The inset in figure 6.4 (a) illustrates the typical helical trajectories that 3D vortex couples energy into different planes. When the slot width is increased to 1.8 μm (figure 6.4 (b)), the sphere has enough space to absorb more light than its diameter resulting in the intensity of electric field and the magnitude of Poynting vector on the substrate to be higher than for smaller slot dimensions. Due to the reflection or inference of light on the side walls, vortex trajectories and corresponding low intensity areas move closer to the sphere's lower boundary as shown in figure 6.4 (b). When the slot width increases to above 3 μm, the intensity on the substrate under the sphere approaches to a constant value as shown in figure 6.2 (a). In spite of changing positions of vortex to the upper part of the sphere, the sphere in a 3.2 μm wide slot still collects light from spaces wider than its diameter. As a result the intensity on substrate under the sphere is higher than that in the case of 1 μm slot width.

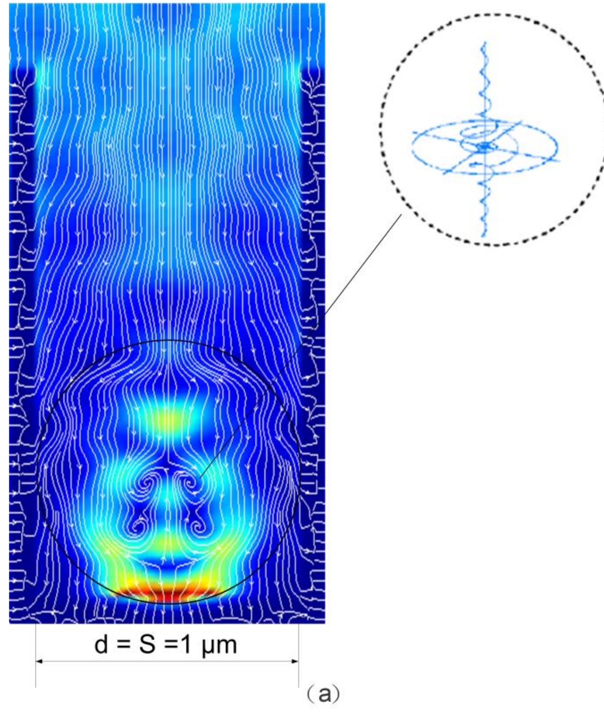

(a)

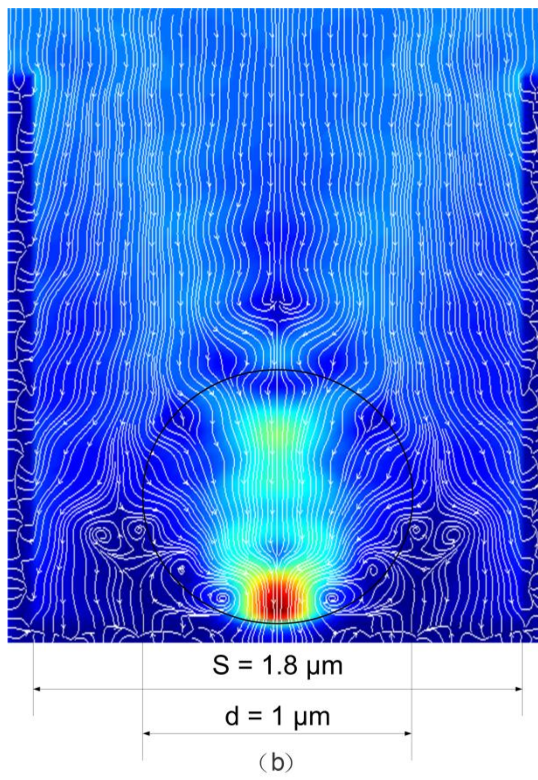

(b)

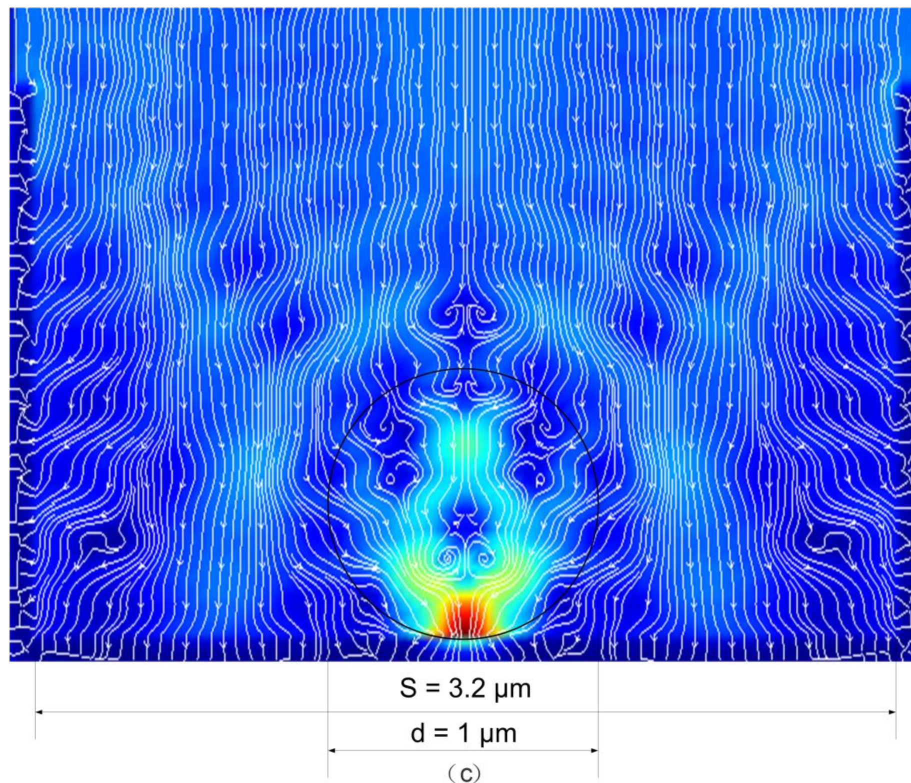

Figure 6.4 The energy flow field lines of single 1μm diameter particle in slot (a) at slot width = 1 μm (b) slot width = 1.8 μm (c) slot width = 3.2 μm. The schematic of 3D vortex coupling energy into different planes is shown as inset in (a).

It can be summarized that the envelope the light energy enters the particle is a limiting factor for the intensity at the bottom of the sphere, which could be wider than the diameter of the particle. The light intensity attenuates and couples to other phase planes through the vortex trajectories. When the vortex trajectories move to the sphere's lower boundary, electric intensity and corresponding magnitude of Poynting vector on the substrate is raised because the sphere focusing effect.

6.3.3 Electromagnetic to thermal modelling: temperature fields

In this work, the electromagnetic field data were coupled to the thermal field for the

analysis of temperature distributions. In this modelling, the laser fluence (0.2 J/cm^2) and related temporal pulse shape (Gaussian pulse) and pulse lengths of 20 ns are loaded. Figure 6.5 (a) shows the temporal temperature distribution on the substrate surface under the sphere for single, two and three particles layouts of 1 μm diameter particle at widths corresponding to P1, P2 and P3 in figure 6.2 (a) respectively. From figure 6.5 (a), it is found that the substrate temperature of the single particle layout is normally higher than those in the other two cases, which corresponds with the result of electromagnetic simulation. The higher magnitude of intensity on the slot bottom creates stronger substrate heating, and a peak temperature of 1928 K is achieved at 10 ns on the substrate. Also, due to the re-focusing effect of the third particle (shown in figure 6.2 (f)), the peak substrate temperature of the three particles layout (1462 K) is higher than for the two particles layout (1081 K). However, the peak temperatures of all three layouts are achieved at 10 ns and the temperature on the substrate returns to room temperature after 18 ns. The melting point of the gold substrate is 1337 K [193]. Therefore a laser beam with a fluence of 0.2 J/cm^2 could damage the substrate in single and three particles layouts, but may be suitable for the two particle layout cleaning. For laser cleaning, a much lower fluence would be needed for the single and three particle layouts.

Figure 6.5 (b) describes the spatial temperature distribution of substrate along the x axis of single, two and three particle layouts at 10 ns (peak temperature time). The curve of the one particle layout is nearly Gaussian distribution in shape. However, the

curves of two and three particles layouts do not form a typical Gaussian distribution because of interference of particle array and Newton's rings phenomenon, though they have obvious peaks in the centre.

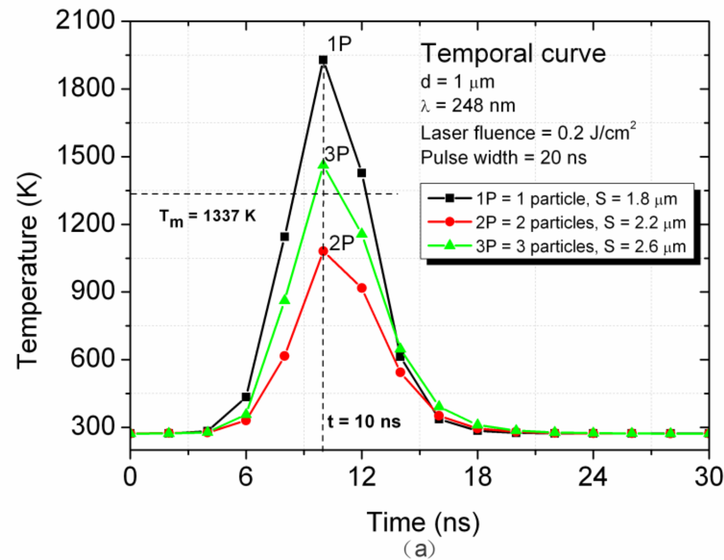

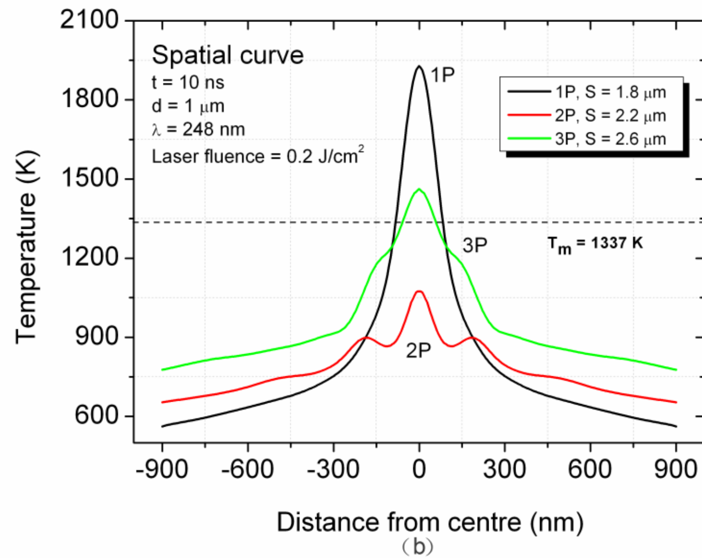

Figure 6.5 (a) Temporal temperature distribution of the substrate surface under single, double and triple particles at optimized slot widths (b), corresponding to spatial temperature distribution of substrate surface at t=10 ns.

6.3.4 Thermal to mechanical modelling: cleaning thresholds

Due to the short pulse laser irradiation, there is a rapidly increasing temperature gradient on the substrate. This sudden increase in temperature generates a cleaning force which ejects particles from the substrate surface. The equation of dry laser cleaning force per unit area, f_l, is given by [76]

$$f_l = \gamma E_s \Delta T(0,t) \tag{2.21}$$

Where γ and E_s are the linear thermal expansion coefficient and the elastic modulus of the substrate, respectively. $\Delta T(0, t)$ is the temperature rise at the substrate surface and time t, which is given by $\Delta T(0, t) = T(0, t) - T_0$, where T_0 is the initial temperature at substrate surface. In current study, $\Delta T(0, t)$ initiated by multiple laser fluences is calculated by the thermal module in CST 2011. The cleaning force can be obtained by calculating the contact area between particle and substrate, which relates to the dominant adhesion force - Van der Waals force, F_v, which is expressed by following equations [37].

$$F_v = \frac{hr}{8\pi z^2} \tag{2.8}$$

Where, r, h and z are the particle radius, the material-dependent Liftshitz-Van der Waals constant and the atomic separation between the particle and surface respectively. Assuming Van der Waals force are the main adhesion force applied to the particle, radius of contact area, a, and elastic depth, d, are deduced by the following equations [37].

$$F_v = \frac{4}{3} E^* r^{1/2} d^{3/2} \tag{5.3}$$

$$a = \sqrt{rd} \tag{5.4}$$

Where E^* is the elastic modulus of two bodies, which is given by

$$\frac{1}{E^*} = \frac{1 - v_1^2}{E_1} + \frac{1 - v_2^2}{E_2} \tag{5.5}$$

E_1, E_2 and v_1, v_2 are the elastic modulus and Poisson's ratios associated with each part, respectively. Thus, the cleaning force initiated by laser, F_c, is expressed by following equation.

$$F_c = f_l \pi a^2 \tag{5.6}$$

Its direction is opposite to the Van der Waals force and gravity of particles. For removal of the tiny particles in micro-slot the cleaning force, F_c, must be larger than the main adhesion force – Van der Waals force, F_v, which is millions times larger than gravity of particle by calculation. For this reason, it is found that the number of particles in layout is only able to influence the gravity of particles chain, whose effect on adhesion force is extremely restricted. Reversely, the size of particles (particle radius, r) controls the magnitude of dominant adhesion force - Van der Waals force by equation (2.8). For obtaining preconditions of cleaning, $F_c > F_v$, related cleaning force generated from laser also depends on it. Therefore, the cleaning threshold in this study is the minimum input laser energy density required to generate enough cleaning force to overcome Van der Waals force and eject the particles from the surface. The damage threshold is defined as the minimum input laser energy to cause surface damages. The damage in this study is assumed to be only caused by thermal reason. The complicated mutual surface stresses between particle and substrate is ignored in the model. In this case, the surface temperature should not be above the melting point of

substrate. If not, the surface is considered as the damage and not allowed.

Based on the above equations and the numerical model, the cleaning and damage thresholds for 1 μm and 2 μm diameter particles under different layouts are presented in table 2 and 3 respectively. The values of Van der Waals force used for table 2 and 3 are 0.179e-6 N and 0.359e-6 N respectively. It is shown that for the single particle layout the cleaning and damage thresholds for the 1 μm diameter particle (table 6.2) are obviously higher than those for 2 μm diameter particle (table 6.3) due to the relatively weaker near-field focusing effect and corresponding temperature rise. However, for the double and triple particles layouts the cleaning and damage thresholds for the 1 μm diameter particle (table 6.2) are lower than for 2 μm diameter particle (table 6.3), which is caused by a fact that 2 μm diameter particle provides stronger defocusing effect and the light intensity gradually attenuates and becomes weak on the substrate. Meanwhile, it is realised that for the same size particles the cleaning and damage thresholds of single and triple particle layouts are lower than for the two particle layout, which corresponds the simulation results of electromagnetic fields, as shown in figure 6.2 (a) and 6.3 (a). It proves that the near-field focusing effect initiated by various particle layouts plays a very important role in the dry laser cleaning system, which needs to be concerned for the measurement of cleaning and damage thresholds. Finally, it is worth mentioning that optical near-fields could be strongly influenced by the factors such as particle shape, transparency, substrate material [104,207,208], and it would be interesting to study non-spherical or nano-

transparent contaminants trapped in micro-slots in the future work.

Table 6.2 Cleaning and damage threshold for the 1-um-diameter glass particles in gold micro-slot

Thresholds	Single particle layout	Double particles layout	Triple particles layout
Cleaning threshold (mJ/cm^2)	42.0	93.3	63.4
Damage threshold (mJ/cm^2)	126.9	263.4	179.0

<u>Definition</u>: ***cleaning threshold*** is the minimum input laser energy density required to generate enough force to eject the particles from the surface**;** ***damage threshold*** is the minimum input laser energy to cause surface damage.

Table 6.3 Cleaning and damage thresholds for the 2-um-diameter glass particles in gold micro-slot

Thresholds	Single particle layout	Double particles layout	Triple particles layout
Cleaning threshold (mJ/cm^2)	17.4	176.5	87.9
Damage threshold (mJ/cm^2)	61.8	626.1	311.7

6.4. Conclusions

We have explored the fundamental physics behind dry laser cleaning of particle contaminants trapped in micro-slots. The multi-physics electromagnetic-thermal-mechanical coupled numerical models have revealed several important physical effects. The magnitudes of field intensity on substrate in certain range of slot width could be elevated by about 25% for 1 and 2 μm diameter particles, and their energy

distributions on the slot bottom were influenced by particle layouts. The transparent spheres could induce the formation of vortex phase trajectories on the laser flow lines, and partial laser power could couple to the other planes of media through these singular points, which affects the focusing effect of particle. The coupled temperature field calculation has revealed enhanced temporal and spatial heating scenario of the substrate beneath different particles layouts, and corresponding surface cleaning and damage thresholds were finally determined.

Chapter 7. Modelling of laser cleaning of tapered micro-slots with different temporal pulses

Abstract

Thermal based laser surface cleaning could strongly depend on the temporal pulse shaping of laser. In this study, we have investigated, based on a Finite Element Method (FEM), the effects of different temporal pulses (Excimer laser, 248 nm, 26 ns), including rectangular and Gaussian shapes, in laser cleaning of micro tapered slots covered by oil film (1.0 μm thick). The FEM model was verified with an analytical solution for a flat surface, and then applied to the tapered micro-slots structure. Plasma shielding effect as an important factor was included in current model. The temporal heating profiles with various laser fluences at different locations of micro-slot were obtained. Corresponding cleaning effects on the cross section of oil film were illustrated. Besides, a mesh size control equation was derived, which could ensure the modelling accuracy (<3% deviation). This work has laid down a theoretical base for further research work in laser cleaning of tapered micro-slots. This work was published as a peer reviewed journal paper on the page 533-539, volume 44, Optics and Laser Technology.

7.1 Introduction

The ultraviolet light with wavelength of 248 nm irradiated by excimer laser provides higher emission current on the surface, which could enhance the cleaning effect [78]. Compared with continuous wave or millisecond pulse lasers, nanosecond laser could provide higher peak power, furthermore boost the cleaning efficiency per pulse. Also, short pulse (ns pulse) and its low duty cycle could greatly restrict the expansion of heat affect zone on the cleaning target surface. For this reason, the substrate could be better protected from the heat damage [78]. On the other hand, tapered silicon micro-slot is a common structure in chemical etching of silicon wafer, and has been widely used in semi-conductor industry [209,210]. In the mass production, the silicon wafers could be sealed by a thin layer of oil as in fabricating of the 3D micro-gears or the microelectromechanical systems (MEMS) devices, which could be the residue that adhesives on the tapered micro-slot after chemical etching [211,212].

In this chapter, a mesh size control equation was initially derived and an FEM model was developed based on two temporal beam shapes (rectangular and Gaussian). This was verified with established analytical solution for a flat surface model. Comprehensive modelling of laser cleaning of tapered micro-slot layered oil film was consequently carried out after the above verification. The optical thickness of plasma cloud was assumed to evenly increase during the pulse duration, and had uniform absorptivity for the laser energy. Corresponding temporal heating profile and cleaning effect on the cross section of the oil film were illustrated. Material phase change,

reflectivity changes at locations and temperature dependent material properties were taken into account in the modelling.

7.2 Numerical simulation

7.2.1 Boundary conditions

The thermal conduction is the only formation of heat transfer chosen in ANSYS software. Thus, several assumptions are ensured in this paper.

(1) All entities in this model are defined as homogeneous bodies, and corresponding thermal properties are isotropic.

(2) Laser beam intensity distribution is an ideal flat top beam. The loaded power intensity in the beam irradiation area is constant.

(3) The power loss in the form of convection and radiation are neglected. The thermal conduction is the only formation of heat transfer in this model.

(4) The multiple reflection that would happen inside micro-slot is neglected. And all reflectivities used this model is based on the wavelength 248 nm.

(5) The sublimation and recoil pressure of material is ignored in this model. The phase change follows the classic solid-liquid-vapour order, and the energy consumed during this process is represented by the enthalpy of material.

Following heating process and boundary conditions are described by equations (7.1), (7.2), (7.3) and (7.4) [213].

$$\rho(T)C(T)\partial T(r,t)/\partial t = \nabla[k(T)\nabla T(r,t)] \qquad T_0 < T < T_{bp} \tag{7.1}$$

$$\frac{\partial H(T)}{\partial t} = \nabla[k\nabla T(r,t)] \qquad T \geq T_{bp} \tag{7.2}$$

$$-k\frac{\partial T}{\partial z}\bigg|_{z=0} = I\left(\vec{r},t\right) \qquad on\ surface, t > 0 \tag{7.3}$$

$$T\left(\vec{r},0\right) = T_0 \qquad t = 0 \tag{7.4}$$

Where ρ is the density, C is heat capacity, t is time, r is radial position, $H(T)$ is the enthalpy function that incorporates the phase changes of the material, k is thermal conductivity, z is the depth, T is the temperature field, T_{bp} is the boiling point, T_0 is the ambient temperature, I is the laser beam intensity distribution which can be expressed by space and time domains equations. All differential equations of laser irradiation on the solid surface are calculated in the non-linear solution mode [214].

7.2.2 Modelling geometry and reflectivity

The model geometry consists of a 1.0 µm thick uniform oil film covering a tapered micro-slot structure. The taper angle was 10°. Fine element (side length < 50 nm) was employed to mesh the oil film part to elevate the accuracy. The schematic and dimensions are shown in figure 7.1(a). Two reflectivities are involved to distinguish the locations of the slot (top surface, bottom and side walls). The reflectivity of the oil was 0.048 for the top surface and the bottom and 0.397 for the side walls. The reflectivities of silicon were to 0.675 (top surface and bottom) and 0.687 (side walls) [194, 215].

7.2.3 Temporal pulse shapes

Rectangular and Gaussian pulses were separately loaded. The intensity of single rectangular pulse can be expressed by [117],

$$I_0(t) = I_0 H(\tau_\ell - t) H(t) \tag{7.5}$$

Where $I_0(t)$, I_0, H and τ_ℓ are intensity of incident laser, the maximum intensity, Heaviside function and pulse duration respectively. The laser fluence, ϕ_R, for this pulse is

$$\phi_R = I_0 \tau_\ell \tag{7.6}$$

Meanwhile, the intensity of the Gaussian pulse is given by following equation [117],

$$I_0(t) = I_0 \left(\frac{t}{\tau_0} \right)^{\beta} \exp\left[\beta \left(1 - \frac{t}{\tau_0} \right) \right] \tag{5.1}$$

Where β describes the temporal shape factor, and τ_0 is the duration that intensity increases to the maximum value from 0. The expression of fluence, ϕ_G, for Gaussian pulse is defined as [117],

$$\phi_G = I_0 \tau_0 \exp(\beta) \frac{\Gamma(\beta + 1)}{\beta^{\beta+1}} \tag{7.7}$$

Here the shape factor β is set to 1, $\Gamma(\beta+1)$ represents the gamma function which equals to the factorial of β here. The relationship between τ_ℓ and τ_0 can be obtained by equation (5.1), approximately as $\tau_\ell = 0.409\tau_0$. For comparison, the aforementioned two pulse shapes were calculated for the same fluence, $\phi_R = \phi_G$, which makes their integrations with the same squares on the intensity shape, as shown in figure 7.1(b).

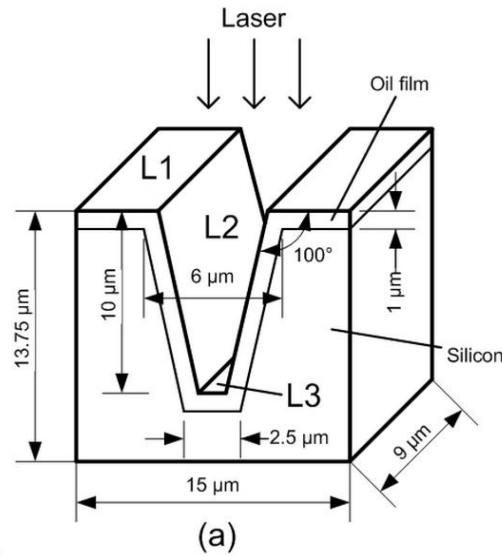

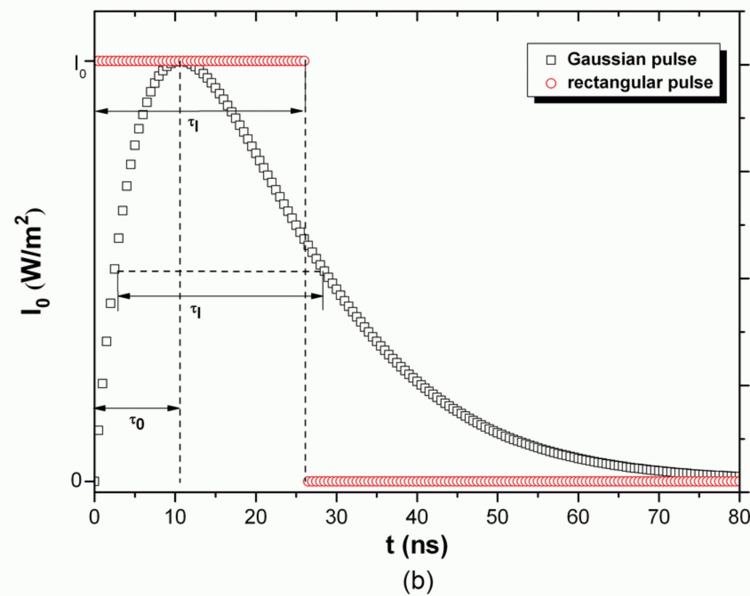

Figure 7.1 (a) The dimension of micro-slot structure (b) Temporal variation of the intensity for rectangular and Gaussian pulses

7.2.4 Material properties

The energy consumed by phase change has taken into account of the material properties and reflects on the temperature dependence of enthalpies. All the temperature dependent and constant properties of crystalline silicon and oil irradiated

by the excimer laser (248 nm wavelength) are given in Table 1 and 2 [193,216]. T_{mp} and A represent the melting point and absorptivity respectively in tables.

Table 7.1 Material properties of crystalline silicon [193,216]

ρ(kg/m^3)	2320	T_{mp} (°C)		1414	T_{bp} (°C)	3265		A	0.325
T(°C)	27	227	427	727	927	1227	1412	1727	2227
H(J/cm^3)	3.286	354.9	727.1	1320	1739	2406	2842	8213	9537
k(W/m K)	148	76.2	51	31.2	25.7	22.5	22	20	18
C(J/kg K)	705	830	860	880	910	920	925	930	930

Table 7.2 Material properties of oil film [193,216]

ρ(kg/m^3)	860	T_{mp} (°C)	-10	T_{bp} (°C)	280	A	0.95
T(°C)	0	37		54.8	67.9		82.5
H(J/cm^3)	214.2	241		276	298		327
k(W/m K)	0.18	0.17		0.15	0.15		0.13
C(J/kg K)	1680	1700		1780	1900		2090

7.2.5 Mesh element

To attach the temperature dependent enthalpies non-linear solution method is selected. For this reason, convergence conditions have become stricter than linear solution mode, which can easily lead to non-convergence on the mesh elements with a high node number. Considering the calculation speed and uneven meshing on the interface between oil film and silicon substrate, pyramid elements with 5 nodes were applied.

7.2.6 The plasma shielding effect

The mechanism of material ionization is sophisticated and strongly affected by many

factors including material properties, concentration and thickness of plasma electrons and the ion cloud. However, for calculation purpose a simplified model is established based on Beer-Lambert law, according to equation (2.28-2.30). In this case, absorption coefficient, α, is assumed as 4.23×10^4 /m, and hydrodynamic expansion velocity of the plasma, c_s, approximates to 340 m/s.

7.3 Results and discussion

7.3.1 Mesh size

In the course of building the current model, it was found that the side length of the mesh element, *l*, should be smaller than the state diffusion of the material, which ensures that boundary conditions could link each node and be loaded on the individual element for the best accuracy. The schematic of pyramid mesh element and its side length are illustrated in insect in figure 7.2 (a). The equations of diffusivity, *D*, is given by [154],

$$D = \frac{k}{\rho C} \tag{7.8}$$

where *D* is the thermal diffusivity.

The state diffusion, *J*, is expressed by

$$J = G\sqrt{D\tau_\ell} \tag{7.9}$$

where *J* and *G* are the state diffusion and empirical factor respectively. The empirical factor *G* could further improve the accuracy of the model. In this case, considering the calculation time, the empirical factor *G* is derived to be 0.9 through the practical

comparison of the temporal rise curves for multiple values. Due to the fact that the thermal conductivity of the oil film is low, the state diffusion of oil, J, is only 54.9 nm based on equations (7.8) and (7.9). Therefore, the side length of the mesh element should be below this value, and all the numerical solution in this paper are based on the geometry meshed by the element whose side length is below 50 nm. The analytical solution of rectangular pulse laser heating substrate is used to verify aforementioned rule [117], and the curves using the multiple mesh sizes are also involved, as shown in figure 7.2 (a). The black curve in figure 7.2 (a) is the standard analytical heating curve. It is found that the curve for $l < J$ (red) is much closer to the result of the analytical solution than the curves for the other mesh sizes.

7.3.2 Flat surface model

A flat surface model (z=0) is established to verify the feasibility of FEM (numerical) model from the proportions of peak temperature and peak temperature time between rectangular and Gaussian pulses on temporal heating profiles. Figure 7.2 (b) shows the temporal heating profiles initiated by the rectangular and Gaussian laser pulses with the same fluence solved by the numerical (dot line) and the analytical (solid line) methods. The analytical profile is obtained from the established literature [17]. Its analytical proportions between two pulse shapes are defined as the criterion, which would be compared with that for numerical solution. The normalized peak temperature and peak temperature time for the rectangular pulse are set to 1.0 in figure 7.2 (b). The FE modelling result is plotted and compared to the analytical one.

Plasma shielding effect is temporarily ignored from the FEM model for the objective comparison with the established literature under the same modelling conditions.

Figure 7.2 (b) shows that the temporal heating profiles and corresponding proportions calculated by two methods are in good agreement. It is observed that the result of the temperature profiles for the rectangular laser pulse calculated by the FE (numerical) model nearly coincides to the analytical one, and is only slightly higher during the cooling period. For the analytical curves (solid lines) the normalized peak temperature and peak temperature time of Gaussian pulse are 0.67 and 0.92 respectively. However, the peak temperature calculated by the numerical solution is higher than these values reaching, 0.70, and a 3% discrepancy appears. The main reason for this could be the error of enthalpy values used in the non-liner solver [216]. Therefore, the FE model is verified to be able to provide a reasonable result for the simulation of laser cleaning with rectangular and Gaussian pulses and the modelling error is low.

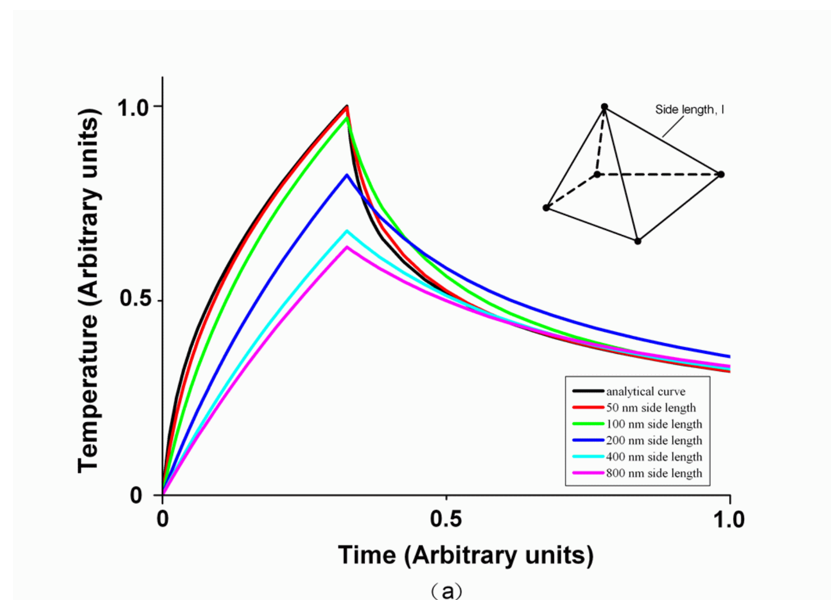

(a)

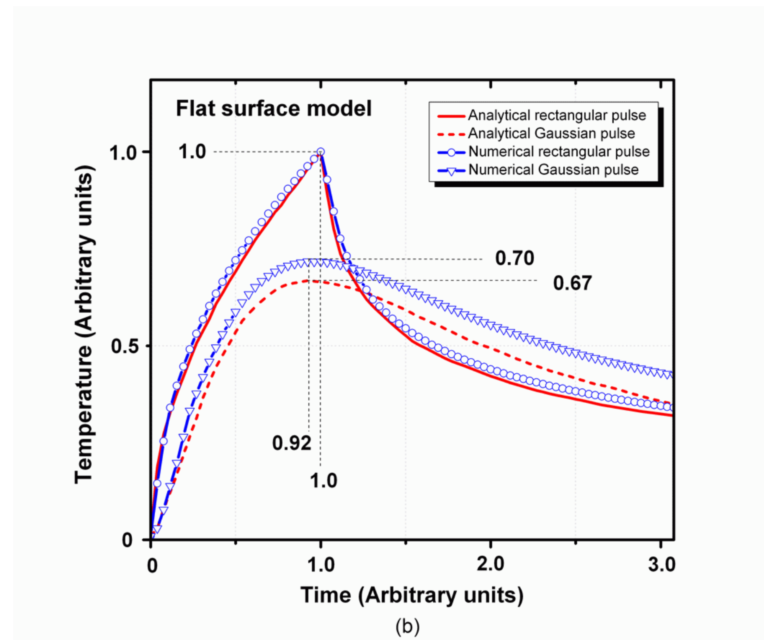

Figure 7.2 (a) Temperature profiles calculated by the analytical solution and numerical solution using FE modelling with multiple mesh sizes (b) Temporal temperature profiles on a flat surface irradiated by the rectangular and Gaussian pulses with the same fluence. Solid and dot lines are calculated by analytical and numerical solution respectively.

7.3.3 Tapered micro-slot modelling

The FE model simulation is that plane wave laser beam (248 nm, 26 ns) vertically irradiating on the micro-slot structure. The geometry has three parts: top surface (L1), side walls (L2) and the bottom surface (L3), as shown in figure 7.1 (a). The ambient temperature is set to 20°C. Figure 7.3 shows that the temporal heating profiles on the oil film surface (z = 0) irradiated by rectangular and Gaussian pulses with 5 fluences (30, 40, 50, 60, 70 mJ/cm^2) at three locations (L1, L2 and L3). Theoretically the oil film where temperature is below the boiling point (T_{bp} = 280°C, as shown in figure 7.3)

directly absorbs the energy from the laser and maintains its liquid state. When its temperature is above the boiling point, the phase change occurs immediately. The oil film starts transferring into the plasma cloud that travels away from the surface towards the laser beam. Meanwhile, the plasma cloud replaces the oil film and absorbs the laser energy. Its temperature and thickness would increase rapidly because of plasma shielding effect during the pulse duration of nanosecond laser [115]. Therefore, the temperature above the boiling point is the plasma cloud temperature in figure 7.3. Also, the oil film where temperature is above the boiling point is considered to be cleaned from substrate.

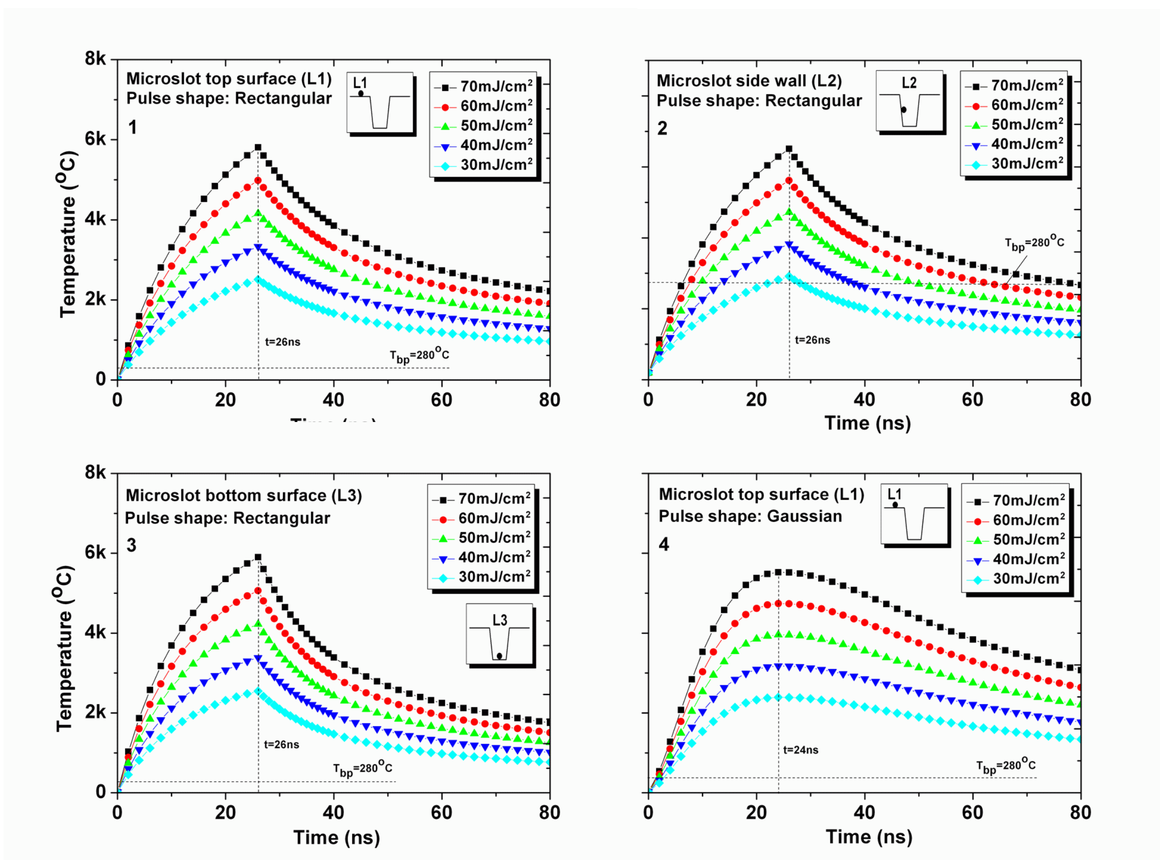

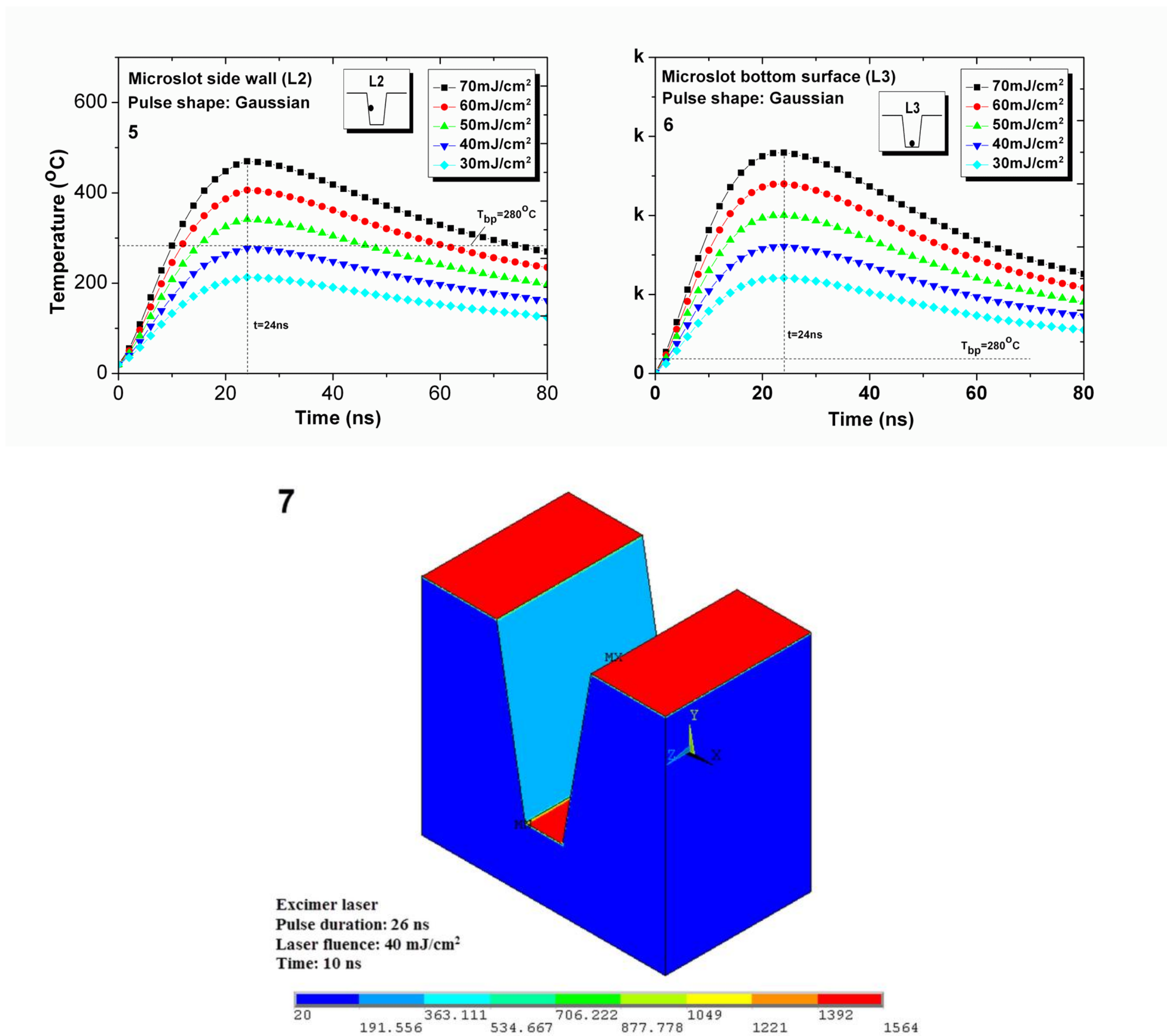

Figure 7.3 Temporal heating profiles of at top surface (L1), side wall (L2) and bottom (L3) with multiple laser fluence for (1-3) rectangular and (4-6) Gaussian pulses. The 3D temperature distribution of 40 mJ/cm^2 for Gaussian shape at 10 ns is illustrated in (7).

Figure 7.3 (1-6) indicates that the peak temperatures on the heating profiles are linear to the increase of laser fluences. The curves of 70 mJ/cm^2 have the highest peak temperature, as shown in figure 7.3 (1-6). For the curve with the same fluence and location it is found that the peak temperature of rectangular pulse approximates 29%

higher than that for the Gaussian pulse. The peak temperatures for the rectangular and the Gaussian pulses occur at 26 ns and 24 ns respectively. Also, for both the rectangular and Gaussian pulses it is observed that the temperature rise of the side wall (L2) is far lower than those on the top surface and the bottom of the slot. Its peak temperature on the side wall is only about 10% of those for on the other locations (L1 and L3) with the same fluence, because the side walls (L2) have the smaller horizontal projection and lower beam intensity. Meanwhile, the 3D temperature distribution of 40 mJ/cm^2 for Gaussian shape at 10 ns is illustrated in figure 7.3 (7). The distributions for other fluences are similar to it.

The cleaning depth and temperature distribution on the cross section of the oil film for the rectangular and Gaussian pulses with 70 mJ/cm^2 are shown in figure 7.4. The smaller mesh size (15 nm) is employed for the illustration of temperature distribution of oil film after laser irradiation. The elements where the temperature is above the boiling point of oil are removed. From figure 7.4, it is known that the cleaning depths for the rectangular pulse are 130 nm (L1), 50 nm (L2), and 135 nm (L3) respectively, and for the Gaussian pulse, the depths are 115 nm (L1), 40 nm (L2) and 120 nm (L3) respectively.

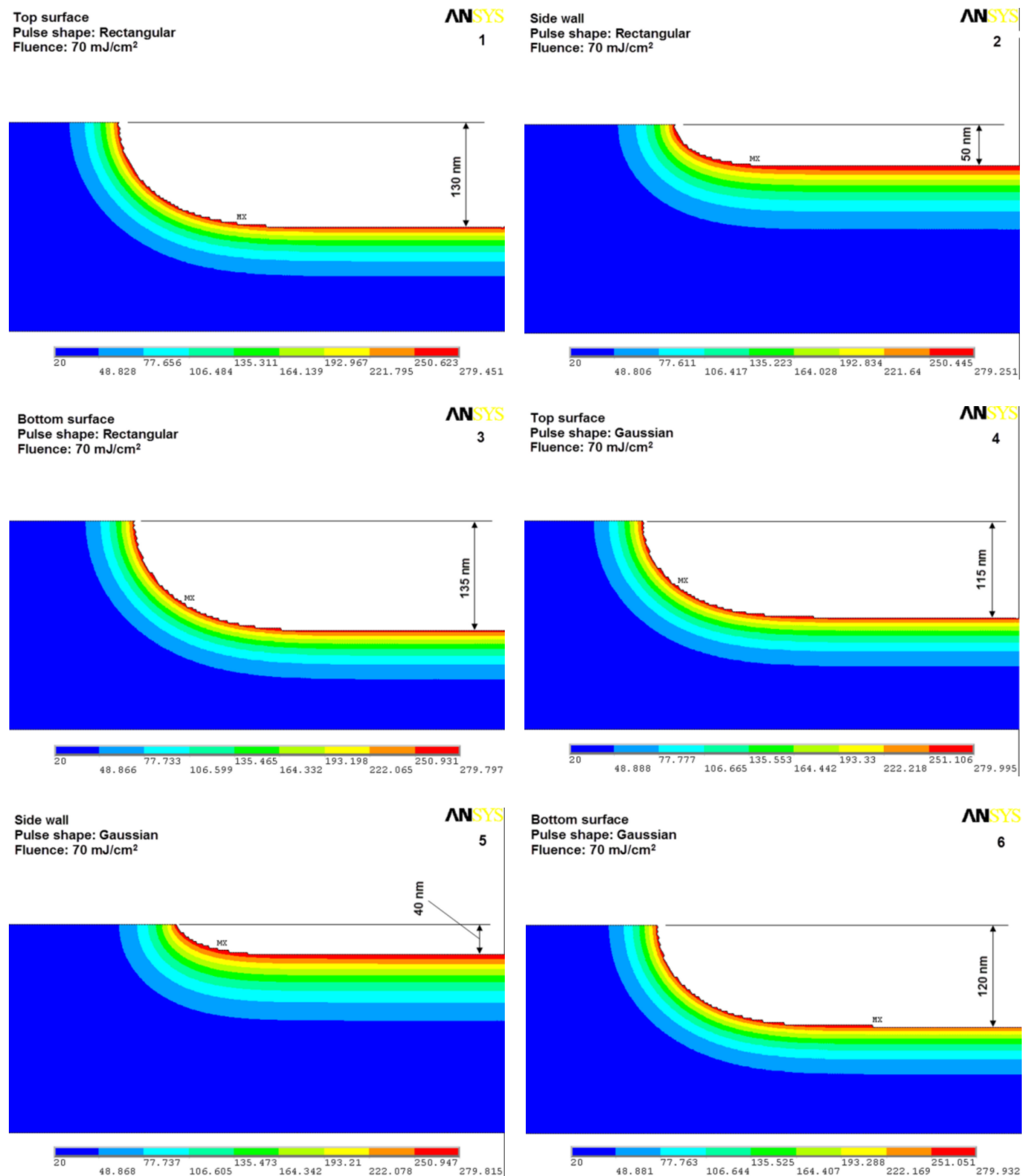

Figure 7.4 The cleaning depths and temperature distributions on the cross section of oil film at top surface (L1), side wall (L2) and bottom (L3) for (1-3) rectangular and (4-6) Gaussian pulses.

Meanwhile, figure 7.5 describes the cleaning depth of rectangular and Gaussian pulses as a function of fluence (20 mJ/cm^2, 30 mJ/cm^2, 40 mJ/cm^2, 50 mJ/cm^2, 60 mJ/cm^2, 70 mJ/cm^2, 80 mJ/cm^2, and 90 mJ/cm^2) at three locations (L1, L2 and L3). It is clear that

for the same location the cleaning depth is linear to the increase of fluence. For the same location and fluence it is observed that rectangular pulse could provide higher cleaning depth compared with that of the Gaussian pulse. The difference between them is about from 10 nm to 20 nm. Also, it is found that the cleaning depth of sidewalls (L2) is much lower than the other two locations under the same laser parameters. The cleaning depth can drop to 0 at low fluences, as shown in figure 7.5. The cleaning threshold is the minimum input laser energy density required to remove the contaminant. The cleaning thresholds of tapered micro-slot structure depend on the cleaning depth at sidewalls (L2) and can be predicted by the current model. All the predicted cleaning thresholds for rectangular and Gaussian pulses are presented in Table 7.3. It shows that higher fluences and extra pulse number are required for the cleaning of side walls (L2). In addition, the cleaning depth on bottom surface is larger than that on top surface, and the average difference is about 10 nm.

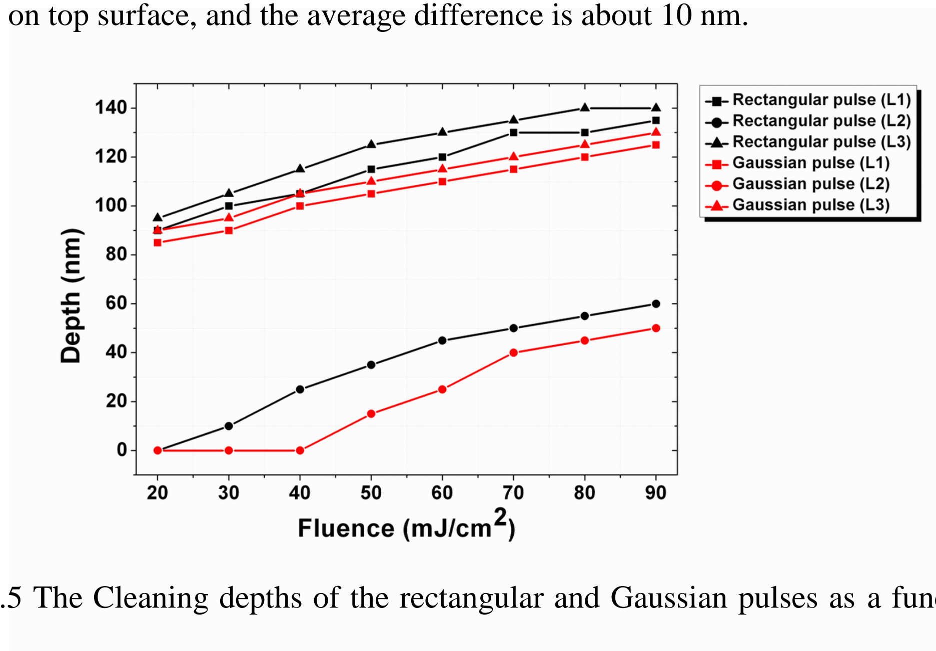

Figure 7.5 The Cleaning depths of the rectangular and Gaussian pulses as a function of laser fluence (20 mJ/cm^2, 30 mJ/cm^2, 40 mJ/cm^2, 50 mJ/cm^2, 60 mJ/cm^2, 70 mJ/cm^2, 80 mJ/cm^2, and 90 mJ/cm^2) at three locations (L1, L2 and L3)

Table 7.3 The cleaning thresholds on micro-slot model

Temporal laser pulse	Cleaning threshold (mJ/cm^2)
Rectangular	20
Gaussian	40

The phenomenon that rectangular provides higher peak temperature and larger cleaning depth could be caused by two factors. Firstly, the rectangular pulse could keep the maximum power intensity, I_0, for the whole pulse duration (26 ns), which benefits the accumulation of energy on the substrate surface. Reversely, although Gaussian pulse has longer pulse output time, it only achieves to the peak intensity at time, τ_0, and then the power intensity starts to go down, as shown in figure 7.1 (b). It is known that the amount of energy provided by Gaussian pulse would be smaller than that for rectangular pulse in the unit laser output period. Secondly, as the main formation of thermal transfer, thermal conduction continuously influences the temperature rise at the substrate surface. Compared with the laser power intensity absorbed by material surface, the intensity loss leaded by thermal conduction at surface only takes the small proportion of power intensity input in whole system which is less than 1% in this case based on equation (7.3). The intensity loss could offset part of the input laser intensity on the material surface. For the rectangular pulse its working period is only the pulse duration (26 ns), which is far shorter than that for Gaussian pulse. Therefore, more laser fluence would be offset due to thermal conduction if Gaussian pulse is employed in cleaning task.

7.4 Conclusions

The FE model successfully simulates the laser cleaning of tapered micro-slot structure irradiated by temporal rectangular and Gaussian pulses, and the cleaning thresholds are predicted based on it. A mesh size control equation has been derived, which provides the modelling accuracy (<3% deviation) compared with established analytical solution. The micro-slot model indicates that the rectangular pulse has higher cleaning efficiency compared to the Gaussian pulse, and cleaning depth at side walls (L2) is lower than the other locations (L1 and L3) using the same laser parameters.

Chapter 8. Conclusions and recommendations for the future

8.1 Conclusions

8.1.1 Technical achievement

A laser cleaning technique was firstly applied on the Ti6Al4V alloy to remove its oxide layer, alpha case, which is difficult to mechanically remove. In this study, it was demonstrated that a laser based process successfully removes alpha case from Ti6Al4V alloy using pulsed laser irradiation. The surface after cleaning is very smooth with 0.11 Ra roughness which is much lower than that for the other removal methods. It was found that the crack characteristics, surface roughness and hardness change of alpha case changed across the ablation depth. Previously the thickness of alpha case was only measured from the cross section of the sample after sectioning, polishing and chemical etching. It has been found from this PhD work that surface morphology after the laser ablation could be used as a diagnostic method to identify the presence of alpha case and measure its thickness due to the specific characteristics of the surface roughness and generated cracks on the ablated surface after laser irradiation. An empirical model was proposed based on this finding.

A novel laser cleaning method for narrow slots was developed. An axial laser beam which propagates into the narrow slots was shown to successfully clean the tiny particles (contaminants) on the slot sidewalls whose width ranges from 3.5 mm to 13

mm. Corresponding experimental cleaning thresholds and efficiencies for multiple slot widths were found. An electromagnetic-thermal-mechanical coupled multiphysics model was established to predict the threshold laser fluence for the initiation of cleaning and substrate damage thresholds, which was validated by experiments. It is shown that the cleaning thresholds generally increase with the increase in slot widths. This work has a potential to be applied to laser cleaning of other complex 3D industrial components.

8.1.2 Scientific achievement

Apart the technical investigation, the fundamental physics behind dry laser cleaning of particle contaminants trapped in small slots was investigated using multiphysics modelling techniques. It is shown that the electromagnetic field intensity on substrate in certain range of slot widths could be elevated by about 25% for 1 and 2 μm diameter particles, and their energy distributions on the slot bottom were influenced by the particle layouts. The transparent spheres change the formation of vortex phase trajectories of the power flow lines, and partial laser power could couple to other media through these singular points, which affects the focusing effect of particle. Therefore, the simulated temperature rises at slot bottoms are different for single, two and three particles vertical layouts, and corresponding surface cleaning and damage thresholds were determined based on an analytical model.

Laser temporal pulses shapes can influence the cleaning effect on the slot structure. A

FEM model was established to understand the effects of temporal rectangular and Gaussian pulses. Their cleaning thresholds were predicted based on this model, and a mesh size control equation was derived. It has been found that the rectangular pulse has higher cleaning efficiency compared to the Gaussian pulse under the same laser parameters, and cleaning depth at side walls is lower than the other locations due to higher reflectivities.

8.2 Future work

8.2.1 Technical exploration

The technique of axial laser beam cleaning could apply to uneven surface, such as cracks or structures with spiral structures such as shreds for screws. Multiple convex lenses with different focal lengths could be used in the axial beam cleaning. The change of optics would influence the contact angle between beam and slot sidewalls, which could change the cleaning effect. Lasers with shorter pulse duration, such as pico or femto second with large beam size, can be used for cleaning and ablation. They usually provide higher peak power and corresponding temperature rise, which benefits the processing effect, but with limited thermal penetration depths due to short pulses, thus limiting the damages to the substrates. The feasibility of steam laser cleaning of slot sidewalls should be investigated in the future. The explosion of bubbles on the slot bottom is possible to lash and move the contaminants on the slot sidewalls.

8.2.2 Scientific exploration

Exploration of the mechanical stresses could be undertaken by simulation using finite element method (FEM). The stress fields and crack propagation are important for the understanding of the mechanism of laser processing. The phase change during laser processing could be modelled by CFD. The analytical mechanics model for cleaning forces may be enhanced by the numerical modelling approach.

References

[1] K.F. Kobayashi, Laser Processing, Elsevier, Amsterdam, 1999, pp. 89-118

[2] A.C. Tam, H.K. Park, C.P. Grigoropoulos, Laser cleaning of surface contaminants, Appl. Surf. Sci, 127-129 (1998) 721-725

[3] G. Vereecke, Laser-assisted Removal of Particles on Silicon Wafers, J. Appl. Phys, 85 (1999) 3837-3848

[4] B.G. Yacobi, Semiconductor Materials: An Introduction to Basic Principles, Springer, Berlin, 2003, pp. 1-3

[5] J.C. Ion, Laser processing of Engineering Materials: Principles, Procedure And Industrial Application, Butterworth – Heinemann, Oxford, 2005, pp. 1-12

[6] D. Schuocker, Handbook of the EuroLaser Academy Vol.1, Springer, Berlin, 1998, pp. 381-388

[7] P. Schaaf, Laser processing of Materials: Fundamentals, Applications and Developments, Springer, Berlin, 2010, pp. 89-189

[8] C. Phipps, Laser Ablation and its Applications, Springer, Berlin, 2006, pp. 215-281

[9] W.T. Silfvast, Laser fundamentals, Cambridge University Press, Cambridge, 2004, pp.1-12

[10] D. Schuocker, Handbook of the Eurolaser Academy, Spinger, Berlin, 1998, pp.1-145

[11] A. Yariv, Quantum Electronics, Wiley, New York, 1989, pp. 302-400

[12] C. K. N. Patel, Continuous-Wave Laser Action on Vibrational-Rotational

Transitions of CO_2, Phys. Rev. A 136 (1985) 1187–1193.

[13] F. J. Duarte, Tunable Lasers Handbook, Academic, New York, 1995, pp. 63-167

[14] W.J. Witteman, The CO_2 laser, Springer-Verlag, Berlin, 1987, pp.8

[15] D.A. Eastham, Atomic Physics of Lasers, Taylor and Francis, Philadelphia, 1986, pp. 84-128

[16] D.R. Whitehouse, Guide to Laser Materials Processing, Laser Institute of America, California, 1993, pp. 46-50

[17] M.W. Turner, P.L. Crouse, L Li, A.J.E. Smith, Investigation into CO_2 laser cleaning of Titanium alloy for gas-turbine component manufacture, Appl. Surf. Sci, 252 (2006) 4798-4802

[18] T. Fourrier, G. Schrems, T. Mühlberger, J. Heitz, N. Arnold, D. Bäuerle, M. Mosbacher, J. Boneberg and P. Leiderer, Laser cleaning of polymer surfaces, Appl. Phys. A – Mater. Sci. Process, 72 (2001) 1-6

[19] Y. Koh, I. Sárady, Cleaning of corroded iron artefacts using pulsed TEA CO_2 and Nd:YAG lasers, J. Cult. Herit., 4 (2003) 129-133

[20] E. Wurzberg, A. Marmur, Laser cleaning of glass surfaces: The effect of thermal diffusion, Adv. Colloid Interface Sci., 119 (1987) 362-370

[21] P.W. Fecsik, F.A. Lancaster, Laser based paint decoating process, Metal. Finishing., 98 (2000) 10-14

[22] C.M. Pacella, G. Francicia, F.M. Di Lascio, V. Arienti, B. Caspani, F. Magnolfi, A.S. Megna, S. Pretolani, R. Regine, M. Sponza, R. Stasi, Long-term outcome of cirrhotic patients with early hepatocellular carcinoma treated with ultrasound-guided percutaneous laser ablation: a retrospective analysis, J Clin Oncol, 27 (2009) 2615-

2621

[23] J. Yang, T.L. Yin, W.M. Xu, L.B. Xia, A.B. Li, J. Hu, Reproductive outcome of septate uterus after hysteroscopic treatment with neodymium:YAG laser, Photomed Laser Surg., 24 (2006) 625

[24] J.E. Geusic, H.M Marcos, L.G. Van Uitert, Laser oscillations in Nd-doped yttrium aluminum, yttrium gallium and gadolinium garnets, Appl. Phys. Lett. 4 (1964) 182-184

[25] P.E. Optoelectronics, High Performance Flash and Arc Lamps, technical document available online at www.optoelectronics.perkinelmer.com., accessed July 2012

[26] G. Hollemann, E. Peik, H. Walther, Frequency-stabilized diode-pumped Nd:YAG laser at 946 nm with harmonics at 473 and 237 nm, Opt. Lett., 19 (1994) 192-194

[27] S.L. Trokel, R. Srinivasan, B. Braren, Eximer laser surgery of the cornea, Am. J. Ophthalmol., 96 (1986) 710-715

[28] G.K. Giust, T.W. Sigmon, High-Performance Thin-Film Transistors Fabricated Using Excimer Laser Processing and Grain Engineering, IEEE Transactions, 45 (1998) 925-932

[29] N. G. Basov, V. A. Danilychev, Y. Popov, D. D. Khodkevich, Sov. Phys. JETP Lett 12 (1970) 473

[30] D. Basting, G. Marowsky, Excimer Laser Technology, Springer, Berlin, 2005, pp. 234

[31] W. Zapka, The Road to ‘Steam Laser Cleaning’, World Scientific, Singapore, 2004, pp. 23-48

[32] G.K. Giust, T.W. Sigmon, High performance thin-film transistors fabricated using excimer laser processing and grain engineering, IEEE Trans. Electron Devices 45 (1998) 4

[33] L. Rymell, H.M. Hertz, Droplet target for low-debris laser-plasma soft X-ray generation, Opt. Commun., 103 (1993) 105-110

[34] N.A. Vainos, S. Mailis, S. Pissadakis, L. Boutsikaris, P.J.M. Parmiter, P. Dainty, T.J. Hall, Excimer laser use for microetching computer-generated holographic structures, Appl. Optics, 19 (1994) 192-194

[35] B. Eliasson, U. Kogelschatz, UV excimer radiation from dielectric-barrier discharges, Appl. Phys. B-Lasers Opt., 46 (1988) 299-303

[36] S. Reiss, A.L. Schawlow, Optics and laser spectroscopy, Bell Telephone Laboratories, 1961

[37] B. Luk'yanchuk, Laser Cleaning, World Scientific Publishing, Singapore, 2003, pp. 181-223

[38] W. Zapka, W. Ziemlich, A.C. Tam, Efficient pulsed laser removal of 0.2 μm sized particles from a solid surface, Appl. Phys. Lett 58 (1991) 2217-2219

[39] W. Zapka, A.C. Tam, W. Ziemlich, Laser cleaning of wafer surfaces and lithography masks, Microelectron. Eng. 13 (1991) 547-550

[40] J.F. Asmus, C.G. Murphy, W.H. Munk, Studies on the Interaction of Laser Radiation with Art Artifacts, Proc. SPIE 41 (1973) 19

[41] E. Galan, F. Zezza, Protection and conservation of the cultural heritage of the mediterranean cities, Taylor&Francis, London, 2002, pp. 615-665

[42] J. Greschner, H. Bohlen, H. Engelke, P. Nehmiz, Electron-beam proximity printing – a new high-speed lithography method for submicron structures, IBM J. Res. Develop. 26 (1977) 514-521

[43] K.L. Mittal, Particles on Surftzccs, Plenum Press, New York, 1998, pp.3-400

[44] A.C. Tam, W.P. Leung, W. Zapka, W. Ziemlich, Laser-cleaning techniques for

removal of surface particulates, J. Appl. Phys 171 (1992) 3515-3523

[45] M. Castillejo, M. Martin, M. Oujja, E. Rebollar, C. Domingo, J.V. Garcia-Ramos, S. Sanchez-Cortes, Effect of wavelength on the laser cleaning of polychromes on wood, J. Cult. Herit., 4 (2003) 243-249

[46] M. Mosbacher, V. Dobler, J. Boneberg, P. Leiderer, Universal threshold for the steam laser cleaning of submicron spherical particles from silicon, Appl. Phys. A – Mater. Sci. Process, 70 (2000) 669-672

[47] P. Maravelaki-Kalaitzaki, V. Zafiropulos, C. Fotakis, Excimer lasercleaning of encrustation on Pentelic marble: procedure and evaluation of the effects, Appl. Surf. Sci., 148 (1999) 92-104

[48] W.M. Steen, Laser material processing, Springer, Berlin, 2005, pp. 327-349

[49] J.F. Asmus, W.H. Munk, C.G. Murphy, Studies on the interaction of laser irradiation of laser radiation with art artefacts, Pro. Soc. Photo-optical Instrum. Eng. (1973) 41

[50] J.F. Asmus, Laser consolidation tests. Final Report, International Fund for Monuments, 1974

[51] J.Q. Hu, Y. Bando, Q.L. Liu, D. Golberg, Laser-Ablation Growth and Optical Properties of Wide and Long Single-Crystal SnO2 Ribbons, Adv. Funct. Mater., 13 (2003) 493-496

[52] M. Von Allmen, P. Blaster, K. Affolter, E. Sturmer, Absorption phenomena in metal drilling with Nd-lasers, J. Quantum Electron, QE-14 (1978) 85

[53] A.M. Bonch-Breuvich, Y.A. Imas, G.S. Romanov, M.N. Libenson, L.N. Mal'ster,

Effect of laser pulse on the reflecting power of a metal, Sov. Phys.-Tech. Phys, 13 (1968) 640

[54] R.M. White, Elastic wave generation by electron bombardment or electromagnetic wave absorption, J. Appl. Phys, 34 (1963) 2123

[55] C.M. Percival, Laser-generated stress waves in a dispersive elastic rod, J. Appl. Phys. 38 (1967) 5315

[56] M. Aden, E. Beyer and G. Herziger, Laser-induced vaporisation of metal as a Riemann problem, J. Appl. Phys. D, 23 (1990) 655-661

[57] C. Knight, Theoretical modelling of rapid vaporisation with back pressure, AIAA J, 17 (1979) 519-523

[58] S. Georgiou, V. Zafiropolos, D. Anglos, C. Balas, V. Tornari, C. Fotakis, Excimer laser restoration of painted artworks: procedures, mechanisms, effects, Appl. Surf. Sci, 127-129 (1998) 738-745

[59] B.S. Luk‘yanchuk, N. Arnold, S.M. Huang, Z.B. Wang, M.H. Hong, Three-dimensional effects in dry laser cleaning, Appl. Phys. A – Mater. Sci. Process, 77 (2003) 209-215

[60] N. Arnold, Theoretical description of dry lasercleaning, Appl. Surf. Sci., 208-209 (2003) 15-22

[61] S. Siano, F. Fabiani, R. Pini, R. Salimbeni, M. Giamello, G. Sabatini, Determination of damage thresholds to prevent side effects in lasercleaning of pliocene sandstone of Siena, J. Cult. Herit., 1 (2000) S47-S53

[62] V. Dobler, R. Oltra, J.P. Boquillon, M. Mosbacher, J. Boneberg, P. Leiderer,

Surface acceleration during dry laser cleaning of silicon, Appl. Phys. A 69 (1999) S335-337

[63] K.G. Watkins, C. Curran, J.M. Lee, Two new mechanisms for laser cleaning using Nd:YAG sources, J. Cult. Herit., 4 (2003) 59-64

[64] S.H. Lee, J.G. Park, J.M. Lee, S.H. Cho, H.K. Cho, Si wafer surface cleaning using laser-induced shock wave: a new dry cleaning methodology, Surf. Coat. Technol., 169-170 (2003) 178-180

[65] J.M. Lee, K.G. Watkins, Removal of small particles on silicon wafer by laser-induced airborne plasma shock waves, J. Appl. Phys., 89 (2001) 6496-6500

[66] C. Curran, J.M. Lee, K.G. Watkins, Ultraviolet laser removal of small metallic particles from silicon wafers, Opt. Laser. Eng 38 (2002) 405-415

[67] W. Kautek, S. Pentzien, P. Rudolph, J. Kruger, E. Konlg, Laser interaction with coated collagen and cellulose fibre composites: fundamentals of laser cleaning of ancient parchment manuscripts and paper, Appl. Surf. Sci., 127-129 (1998) 746-754

[68] P. Neves, M. Arronte, R. Vilar, A.M. Botelho do Rego, KrF excimer laser dry and steam cleaning of silicon surfaces with metallic particulate contaminants, Appl. Phys. A – Mater. Sci. Process, 74 (2002) 191-199

[69] A. Kruusing, Underwater and water-assisted laser processing: Part 1—general features, steamcleaning and shock processing, Opt. Lasers Eng., 41 (2004) 307-327

[70] K. Imen, S.J. Lee, S.D. Allen, Laser assisted micron scale particle removal, Appl. Phys. Lett., 58 (1991) 203-205

[71] W.D. Song, M.H. Hong, S.H. Lee, Y.F. Lu, T.C. Chong, Real-time monitoring of

laser cleaning by an airborne particle counter, Appl. Surf. Sci., 208-209 (2003) 306-310

[72] P.V. Maravelaki, V. Zafiropulos, V. Kilikoglou, M. Kalaitzaki, C. Fotakis, Laser-induced breakdown spectroscopy as a diagnostic technique for the laser cleaning of marble, Spectroc. Acta Pt. B – Atom. Spectr., 52 (1997) 41-53

[73] A. Leontyev, A. Semerok, D. Farcage, P.Y. Thro, C. Grisolia, A. Widdowson, P. Coad, M. Rubel, Theoretical and experimental studies on molybdenum and stainless steel mirrors cleaning by high repetition rate laser beam, Fusion Eng. Des., 86 (2011) 1728-1731

[74] D.H. Tan, D.S Lu, Study of laser cleaning threshold and damage threshold, Laser & Optoelectronics Progress, 34 (1997) 17-20

[75] R. Tambay, D.V.S. Muthu, V. Kumar, R.K. Thareja, Laser induced air breakdown using 0.355, 0.532, and 1.06μm radiation, Pramana – J. Phys., 37 (1991) 163-166

[76] Y.F. Lu, W.D. Song, Y. Zhang, T.S. Low, Theoretical model and experimental study for dry and steam laser cleaning, Proc. SPIE—Int. Soc. Opt. Eng 3550 (1998) 7–18

[77] Y.F. Lu, W. Sung, M. Hong, Laser removal of particles from magnetic head sliders, J. Appl. Phys. 80 1 (1996) 499-504

[78] Y.F. Lu, M. Takai, S. Komuro, Surface cleaning of metals by pulsed-laser irradiation in air, Appl. Phys. A. 59 3 (1994) 281-288

[79] K. Kuwagi, K. Takano, M. Horio, The effect of tangential lubrication by bridgeliquid on the behavior of agglomerating fluidized beds, Powder Technol., 113 (2000) 287-298

[80] K. Hotta, K. Takeda, K. Linoya, The capillary binding force of a liquid bridge, Powder Technol., 10 (1974) 231-242

[81] Z. Wei, Y.P. Zhao, Growth of liquid bridge in AFM, J. Phys. D: Appl. Phys., 40 (2007) 4368

[82] G. Lian, C. Thornton, M.J. Adams, A theoretical study of the liquid bridge forces between two rigid spherical bodies, J. Colloid Interface Sci 161 (1993) 138-147

[83] T. Daido, Electrochemistry of cytochrome c: influence of coulombic attraction with indium tin oxide electrode, J. Electroanal. Chem., 344 (1993) 91-106

[84] U. Mohideen, A. Roy, Precision Measurement of the Casimir Force from 0.1 to 0.9 μm, Phys. Rev. Lett., 81 (1998) 4549-4552

[85] L. Heim, J. Blum, M. Preuss, H. Butt, Adhesion and Friction Forces between Spherical Micrometer-Sized Particles, Phys. Rev. Lett., 83 (1999) 3328-3331

[86] V.P. Carey, Liquid-Vapor Phase-Change Phenomena, Hemisphere Publishing Corporation, Bristol, 1992, pp. 230-280

[87] W. Zapka, W. Ziemlich, W. P. leung, A.C. Tam, Laser cleaning removes particles from surfaces, Microelectron. Eng. 20 (1993) 171

[88] C.J. Knight, Theoretical modeling of rapid surface vaporization with back pressure, AIAA J. 17 (1978) 519

[89] D.A Hutchins, R.J. Dewhurst, S.B. Palmer, Laser generated ultrasound at modified metal surfaces, Ultrasonics, 19 (1981) 103

[90] O. Yavas, A. Schilling, J. Bischof, J. Boneberg, P. Leiderer, Bubble nucleation and pressure generation during laser cleaning of surfaces, Appl. Phys. A 64 (1997) 331

[91] P.D. Edmonds, F. Dunn, Ultrasonics (Methods in Experimental Physics, Vol. 19), Academic, New York, 1981, pp. 67-137

[92] A.V. Bulgakov, N.M. Bulgakova, Thermal model of pulsed laser ablation under

the conditions of formation and heating of a radiation-absorbing plasma, quantum electron. 29 (1999) 433-437

[93] M. Stafe, C. Negutu, I.M. Popescu, Theoretical determination of the ablation rate of metals in multiple-nanosecond laser pulses irradiation regime, Appl. Surf. Sci. 253 (2007) 6353-6358

[94] J.D. Ingle, S.R. Crouch, Spectrochemical Analysis, Prentice Hall: Englewood Cliffs, New Jersey, 1988, pp. 372-381

[95] E. Fabre, C. Stenz, CO_2-laser-beam absorption by a dense plasma, Phys. Rev. Lett., 32 (1973) 823-826

[96] H. Lim, D. Jang, D. Kim, J.W. Lee, J.M. Lee, Correlation between particle removal and shock wave dynamics in the laser shock leaning process, J. Appl. Phys. 97 054903 (2005) 1-6

[97] W.D. Song, M.H. Hong, B. Lukyanchuk, T.C. Chong, Laser-induced cavitation bubbles for cleaning of solid surfaces, J. Appl. Phys. 95 (2004) 2952-2956

[98] W.T. Arkin, New topics in lasers and electro-optics, Nova Science, New York, 2006, pp.116

[99] W. Weaver, J.M. Gere, Matrix Analysis of Framed Structures, Springer-Verlag, New York, 1966, pp. 1-53

[100] K.H. Huebner, D.L. Dewhirst, D.E. Smith, T.G. Byrom, The Finite Element Method for Engineers, John Wiley & Sons, Hoboken, 2001, pp. 17-113

[101] H. Luo, S. Hanagud, An integral equation for changes in the structural dynamics characteristics of damaged structures, Int. J. Solids Struct., 34 (1997) 4557-4579

[102] C.F. Bohren, D.R. Huffman, Absorption and Scattering of Light by Small Particles, Wiley, New York, 1983, pp. 7

[103] A. Thom, C.J. Apelt, Field Computations in Engineering and Physics, D. Van Nostrand, London, 1961, pp. 1-121

[104] Y.W. Zheng, B.S. Luk'yanchuk, Y.F. Lu, W.D. Song, Z.H. Mai, Dry laser cleaning of particles from solid substrates: Experiments and theory, J. Appl. Phys., 90 5 (2001) 2135

[105] T. Weiland, Time Domain Electromagnetic Field Computation with Finite Difference Methods, Internat. J. Numer. Modelling. 9 (1996) 295-319

[106] J.R. Reitz, J.M. Frederick, Foundations of Electromagnetic Theory, Addison-Wesley, England, 1960, pp. 25-304

[107] J.D. Anderson, Computational Fluid Dynamics: The Basics with Applications, Science/Engineering/Math. McGraw-Hill Science, London, 1995, pp. 1-80

[108] J.L. Hess, A.M.O. Smith, Calculation of Potential Flow About Arbitrary Bodies, Prog. Aerosp. Sci, 8 (1967) 1-138

[109] T.M. Tritt, Thermal conductivity: theory, properties, and applications, Springer, Berlin, 2004, pp. 1-17

[110] R. Baierlein, Thermal physics, Cambridge University Press, Cambridge, 1999, pp. 244-378

[111] M.F. Chen, Y.H. Wang, W.T. Hsiao, Finite element analysis and verification of laser marking on eggshell, J. Mater. Process. Technol. 209 (2009) 470-476

[112] Z. Zhang, A. Bejan, Melting in an enclosure heated at constant rate, Int. J. Heat

Mass Tran, 32 (1989) 1063-1076

[113] C. Ho, R. Viskanta, Heat transfer during inward melting in a horizontal tube, Int. J. Heat Mass Tran, 27 (1984) 705-716

[114] A. Gadgil, D. Gobin, Analysis of two-dimensional melting in rectangular enclosures in presence of convection, J Heat Transf, 106 (1984) 20-26

[115] R.K. Singh, J. Narayan, Pulsed-laser evaporation technique for deposition of thin films: Physics and theoretical model, Phys. Rev. B 41 (1990) 8843-8859

[116] Y.P. Lee, Y.F. Lu, D.S.H. Chan, T.S. Low, M.S. Zhou, Steam Laser Cleaning of Plasma-Etch-Induced Polymers from Via Holes, Jpn. J. Appl. Phys. 37 (1998) 2524-2529

[117] D. Bauerle, Laser Processing and Chemistry, Springer, Berlin, 2000, pp.105-120

[118] V. Oliveira, R. Vilar, Finite element simulation of pulsed laser ablation of Titanium carbide, Appl. Surf. Sci 253 (2007) 7810-7814

[119] N.A. Vasantgadkar, U.V. Bhandarkar, S.S. Joshi, A finite element model to predict the ablation depth in pulsed laser ablation, Thin Solid Films 519 (2010) 1421-1430

[120] G. Pelosi, The finite-element method, Part I: R. L. Courant: Historical Corner, Antennas and Propagation Magazine, IEEE 49 (2007) 180-182

[121] R. Fang, D. Zhang, Z. Li, F. Yang, L. Li, X. Tan, M. Sun, Improved thermal model and its application in UV high-power pulsed laser ablation of metal target, Solid State Commun. 145 (2008) 556-560

[122] R.K. Singh, J. Viatella, Estimation of plasma absorption effects during pulsed

laser ablation of high-critical-temperature superconductors, J. Appl. Phys. 75 (1994) 1204-1206

[123] Z.B. Wang, W. Guo, L. Li, B. Luk'yanchuk, A. Khan, Z. Liu, Z.C. Chen, M.H. Hong, Optical virtual imaging at 50 nm lateral resolution with a white-light nanoscope, Nat. Commun. 2 (2011) 218

[124] T. Taubner, D. Korobkin, Y. Urzhumov, G. Shvets, R. Hillenbrand, Near-field microscopy through a SiC superlens, Science. 313 5793 (2006) 1595

[125] B.S. Luk'yanchuk, Y.W. Zhang, Y.F. Lu, Laser cleaning of solid surface: optical resonance and near-field effects, Proc. SPIE. 4065 (2000) 576

[126] M. Mosbacher, H.J. Munzer, J. Zimmermann, J. Solis, J. Boneberg, P. Leiderer, Optical field enhancement effects in laser-assisted particle removal, Appl. Phys. A. 72 (2001) 41-44

[127] D.R. Halfpenny, D.M. Kane, A quantitative analysis of single pulse ultraviolet dry laser cleaning, J. Appl. Phys. 86 (1999) 6641

[128] M. Mosbacher, N. Chaoui, J. Siegel, V. Dobler, J. Solis, J. Boneberg, C.N. Afonso, P. Leiderer, A comparison of ns and ps steam laser cleaning of Si surfaces, Appl. Phys. A. 69 (1999) S331-334

[129] Y.F. Lu, W.D. Song, K.D. Ye, M.H. Hong, D.M. Liu, D.S.H. Chan, T.S. Low, Removal of submicron particles from nickel-phosphorus surfaces by pulsed laser irradiation, Appl. Surf. Sci. 120 (1997) 317-322

[130] B. Oh, J.W. Lee, J.M. Lee, D. Kim, Numerical simulation of laser shock cleaning process for micro-scale particle removal, J. Adhes. Sci. Technol. 22 (2008)

635–650

[131] S. Yang, V.N. Astratov, Photonic nanojet-induced modes in chains of size-disordered microspheres with an attenuation of only 0.08 db per sphere, Appl. Phys. Lett. 92 26 (2008) 261111

[132] M. Archer, M. Christophersen, P.M. Fauchet, Electrical porous silicon chemical sensor for detection of organic solvents, Sensor Actuat B-Chem, 106 (2005) 347-357

[133] D.A. Hodges, H.G. Jackson, R. Saleh, Analysis and Design of Digital Integrated Circuits, McGraw-Hill, New York, 2003, pp. 35-230

[134] Elecric Site, link: http://gallery.hd.org/_c/electronics/_more2004/_more05/silicon-wafer-oblique-gold-background-1-DHD.jpg.html, last viewed: 14/10/2012

[135] A.C. Duncan, F. Rouais, S. Lazare, L. Bordenave, C. Baquey, Effect of laser surface microtopochemistry on endothelial cell growth, Colloid. Surface. B., 54 (2007) 150-159

[136] L. Yue, Z. Wang, L. Li, Material morphological characteristics in laser ablation of alpha case from Titanium alloy, Appl. Surf. Sci., 258 (2012) 8065-8071

[137] tweaktown website, link: http://www.tweaktown.com/reviews/4505/swiftech_h20_x20_edge_hd_water_cooling_kits_review/index6.html, last viewed: 14/10/2012

[138] L.A. Corathers, 2009 Minerals Yearbook, USGS, Reston, 2009, pp. 1-12

[139] M.G. Voronkov, Silicon era, Russ. J. Appl. Chem, 80 (2007) 2190

[140] M.T. Kelly, A.B. Bocarsly, Mechanisms of photoluminescent quenching of

oxidized porous siliconapplications to chemical sensing, Coord. Chem. Rev., 171 (1998) 251-259

[141] L.T. Canham, Silicon quantum wire array fabrication by electrochemical and chemical dissolution of wafers, Appl. Phys. Lett., 57 (1990) 1046

[142] M.T. Kelly, J.K.M. Chun, A.B. Bocarsly, High efficiency chemical etchant for the formation of luminescent porous silicon, Appl. Phys. Lett., 64 (1994) 1693

[143] N. Asada, H. Matsuki, K. Minami, M. Esashi, T. Univ, Silicon micromachined two-dimensional galvano optical scanner, IEEE Trans. Magn., 30 (1994) 4647-4649

[144] T. Walsh, Silly Putty, Andrews McMeel Publishing, Kansas City, 2005, pp. 90-120

[145] P.A. Laplante, Comprehensive dictionary of electrical engineering, CRC Press, Boca Raton, 2005, pp. 739-748

[146] K.E. Jones, R.J. Huber, K.W. Horch, R.A. Normann, A silicon-based, three-dimensional neural interface: manufacturing processes for an intracortical electrode array, IEEE Trans. Biomed. Eng., 38 (1991) 758-768

[147] S.D. Penn, G.M. Harry, A.M. Gretarsson, S.E. Kittelberger, P.R. Saulson, J.J. Schiller, J.R. Smith, S. Swords, High quality factor measured in fused silica, Rev. Sci. Intermed., 72 (2001) 3670

[148] L.M. Barker, Shock Wave Studies of PMMA, Fused Silica, and Sapphire, J. Appl. Phys., 41 (1970) 4208-4226

[149] F.J. Yang, Fused-silica narrow-bore microparticle-packed-column high-performance liquid chromatography, J. Chromatogr., A, 236 (1982) 265-277

[150] D. Lu, C.P. Wong, Materials for advanced packaging, Springer, Berlin, 2008, pp. 344-370

[151] W. Guo, Z.B. Wang, L. Li, Z. Liu, B. Luk'yanchuk, D.J. Whitehead, Chemical-assisted laser parallel nanostructuring of silicon in optical near fields, Nanotechnology 19 (2008) 455302

[152] G.Z. Chen, D.J. Fray, T.W. Farthing, Catholic deoxygenation of the alpha case on Titanium and alloys in molten calcium chloride, Metall. Mater. Trans. B. 32 (2001) 1041-1052

[153] A.D. McQuillan, M.K. McQuillan, Titanium, Butterworths Scientific Publications, London, 1956, pp.232-270

[154] D.R. Lide, CRC Hand book of chemistry and physics, CRC Press, Boca Raton, 2000, pp. 12-189

[155] H. Clemens, H. Kestler, Processing and applications of intermetallic γ-TiAl-based alloys, Adv. Eng. Mater. 2 (2000) 551-570

[156] R.R. Boyer, An overview on the use of Titanium in the aerospace industry, J. Mater. Sci. Eng., 213 (1996) 103-114

[157] R.R. Boyer, R.D. Briggs, The use of β Titanium alloys in the aerospace industry, J. Mater. Eng. Perform. 14 (2005) 681-685

[158] E.P. Lautenschlager, P. Monaghan, Titanium and Titanium alloys as dental materials, Int. Dent. J. 43 (1993) 245-253

[159] B. Cantor, P. Grant, H. Assender, Aerospace materials, CRC Press, Boca Raton, 2001, pp. 120-345

[160] S.Y. Sung, Y.J. Kim, Alpha-case formation mechanism on Titanium investment castings, Mater. Sci. Eng. A 405 (2005) 173-177

[161] W.C. Say, Y.Y Tsai, Surface characterization of cast Ti-6Al-4V in hydrofluoric-nitric pickling solutions, Surf. Coat. Technol. 176 (2003) 337-343

[162] C. Ohkubo, T. Hosoi, J. P. Ford, I. Watanabe, Effect of surface reaction layer on grindability of cast Titanium alloys, Dent. Mater. 22 (2006) 268-274

[163] M.C. Kong, D. Axinte, W. Voice, Aspects of material removal mechanism in plain waterjet milling on gamma Titanium aluminide, J. Mater. Process. Technol. 210 (2010) 573-584

[164] W.M. Steen, J. Mazumder, Laser material processing fourth edition, Springer, London, 2010

[165] Y.S. Tian, C.Z. Chen, S.T. Li, Q.H. Huo, Research progress on laser surface modification of Titanium alloys, Appl. Surf. Sci. 242 (2005) 177-184

[166] C. Langlade, A.B. Vannes, J.M. Krafft, J.R. Martin, Surface modification and tribological behaviour of Titanium and Titanium alloys after YAG-laser treatments, Surf. Coat. Technol. 100-101 (1998) 383

[167] T.M. Yue, J.K. Yu, Z. Mei, H.C. Man, Excimer laser surface treatment of Ti-6Al-4V alloy for corrosion resistance enhancement, Mater. Lett. 52 (2002) 206

[168] O.V. Overschede, S. Dinu, G. Guisbiers, F. Monteverde, C. Nouvellon, M. Wautelet, Excimer laser ablation of thin Titanium oxide films on glass, Appl. Surf. Sci. 252 (2005) 4722-4727

[169] G. Leggieri, A. Luches, M. Martino, A. Perrone, G. Majni, P. Mengucci, I.N.

Mihailescu, Laser reactive ablation deposition of Titanium carbide films, Thin Solid Films 258 (1995) 40- 45

[170] R. Teghil, L. D'Alessio, A. De Bonis, A. Galasso, P. Villani, A. Santagata, Femtosecond pulsed laser ablation and deposition of Titanium carbide, Thin Solid Films 515 (2006) 1411-1418

[171] E. Suzuki, High-resolution scanning electron microscopy of immunogold-labelled cells by the use of thin plasma coating of osmium, J. Microsc, 208 (2002) 153-157

[172] A. Antonovsky, The application of colour to sem imaging for increased definition". Micron Microsc Acta, 15 (1984) 77-84

[173] Y.N. Denisyuk, Photographic reconstruction of the optical properties of an object in its own scattered radiation field, Sov. Phys.-Dokl, 7 (1962) 543

[174] B.J. Chang, C. Rod, E. Alferness, E.N. Leith, Space-invariant achromatic grating interferometers: theory (TE), Appl. Opt., 14 (1975) 1592

[175] B. Cappella, G. Dietler, Force-distance Curves by Atomic Force Microscopy Surface, Science Reports 34 (1-3): 1–104, Elsevier, Amsterdam, 1999, pp. 10-78

[176] ANSYS website. [Online] Available from: http://www.ansys.com/

[177] O.L.A. Harrysson, O. Cansizoglu, D.J. Marcellin-Little, D.R. Cormier, H.A. West II, Direct metal fabrication of titanium implants with tailored materials and mechanical properties using electron beam melting technology, Materials Science Engineering C-Biomimetic, 28 (2008) 366-373

[178] CST website. [Online] Available from: http://www.cst.com/

[179] M. Sundar, D. Whitehead, P.T. Mativenga, L. Li, K.E. Cooke, Excimer laser decoating of chromium Titanium aluminium nitride to facilitate re-use of cutting tools, Opt. Laser. Technol. 41 (2009) 938-944

[180] I. Gurappa, Prediction of Titanium alloy component life by developing an oxidation model, J. Mater. Sci. Lett. 22 (2003) 771-774

[181] C. Prat, G.N. Costa, M. Autric, Characterization of the Behavior of Ceramic Materials Submitted to U. V. Laser Radiations, Proc. SPIE 2502 (1995) 638-641

[182] L. Bradley, L. Li, F.H. Stott, Flame-assisted laser surface treatment of refractory material for crack-free densification, Mater. Sci. Eng. A 278 (2000) 204-212

[183] S.T. Tu, Creep behavior of crack near bi-material interface characterized by integral parameters, J. Theor. Appl. Fracture. Mech, 38 (2002) 203-209

[184] M.R. Begley, B.N. Cox, R.M. McMeeking, The dependent crack growth in ceramic matrix composites with creeping fibers, Acta Metall. Mater. 43 (1995) 3927-3936

[185] S.Y. Sung, B.J. Choi, B.S. Han, H.J. Oh, Y.J. Kim, Evaluation of alpha-case in Titanium casting, J. Mater. Sci. Technol. 24 (2008) 70-74

[186] S.N. Patankar, T. M. Jen, Influence of alpha casting on superplastic deformation of Ti-6Al-4V, ASME J. Eng. Mater. Technol. 123 (2001) 144-147

[187] H.L. Du, P.K. Datta, D.B. Lewis, J.S. Burnell-Gray, Effort of alpha case formation on creep fracture properties of the high temperature Titanium alloys, Oxid. Met. 45 (1996) 507

[188] J. Lawrence, L. Li, J.T. Spencer, Ceramic tile grout removal and tile sealing

using high power lasers, Proceeding of ICALEO ’96: Laser Materials Processing, Detroit (1996) 138-148

[189] R. Boyer, G. Welsch, E.W. Collings, Materials Properties Handbook: Titanium Alloys, ASM International, Materials Park, OH, 1994

[190] W.J. Boettinger, M.E. Williams, S.R. Coriell, U.R. Kattner, B.A. Mueller, Alpha case thickness modeling in investment casting, Metall. Mater. Trans. B 31 (2000) 1419-1427

[191] Y.F. Lu, W.D. Song, M.H. Hong, Y.W. Zheng, T.C. Chong, Laser surface cleaning and potential applications in disk drive industry, Tribol. Int. 33 (2000) 329-335

[192] I.H. Malitson, Interspecimen comparison of the refractive index of fused silica, J. Opt. Soc. Am. 55 (1965) 1205-1208

[193] M.W. Chase, NIST-JANAF Thermo-Chemical Tables 4th edition, The American Chemical Society and the American Institute of Physics, Washington, 1996, pp.1881-1887

[194] E.D. Palik, Handbook of optical constants of solids, Academic Press, Boston, 1985, pp.571-602

[195] C.J. Glassbrenner, G.A. Slack, Thermal conductivity of silicon and germanium from 3 K to the melting point, Phys. Rev. 134-4A (1964) A1058-A1069

[196] Z.B. Wang, W. Guo, B.S. Luk'yanchuk, D.J. Whitehead, L. Li, Z. Liu, Optical near-field interaction between neighbouring micro/nano-particles, J. Laser Micro/Nanoeng. 3 (2008) 14-18

[197] L.Y. Yue, Z.B. Wang, L Li, Multiphysics modelling and simulation of dry laser cleaning of micro-slots with particle contaminants, J. Phys. D: Appl. Phys. 45 (2012) 135401

[198] W. Zapka, W. Ziemlich, W.P. Leung, A.C. Tam, Laser cleaning: laser-induced removal of particles from surfaces, Adv. Mater. Opt. Electron. 2 (1993) 63-70

[199] L. Poirier, P. Coulon, W. Williamson, P. Verin, Energy fluctuations in an excimer laser during photorefractive keratectomy, J Refract Corneal Surg. 10 (1994) S258-261

[200] J.W. Belcher, S. Olbert, Field line motion in classical electromagnetism, Am. J. Phys. 71 (2003) 220

[201] L. Magagnin, R. Maboudian, C. Carraro, Gold deposition by galvanic displacement on semiconductor surfaces: effect of substrate on adhesion, J. Phys. Chem. B 106 (2002) 401-407

[202] A. Khan, Z.B. Wang, M.A. Sheikh, D.J. Whitehead, L. Li, Parallel near-field optical micro/nanopatterning on curved surfaces by transported micro-particle lens arrays, J. Phys. D: Appl. Phys. 43 (2010) 305302

[203] A. Khan, Z.B. Wang, M.A. Sheikh, D.J. Whitehead, L. Li, Laser micro/nano patterning of hydrophobic surface by contact particle lens array, Appl. Surf. Sci. 258 2 (2011) 774-779

[204] A. Lipson, S.G. Lipson, H. Lipson, Optical physics 4th edition., Cambridge University Press, Cambridge, 2010, pp.559

[205] N.V. Karlov, N.A. Kirchenko, B.S. Luk'yanchuk, Laser thermochemistry:

fundamentals and applications.,Cambridge Intl Science Pub, Cambridge, 2000, pp.54-59

[206] Z.B. Wang, B.S. Luk'yanchuk, M.H. Hong, Y. Lin, T.C. Chong, Energy flow around a small particle investigated by classical Mie theory, Phys. Rev. B 70 3 (2004) 035418

[207] T.A. Nieminen, H. Rubinsztein-Dunlop, N.R. Heckenberg, Calculation and optical measurement of laser trapping forces on non-spherical particles, J. Quant. Spectrosc. Radiat. Transfer. 70 (2001) 627-637

[208] C.G. Xie, Y.Q. Li, Raman spectra and optical trapping of highly refractive and nontransparent particles, Appl. Phys. Lett. 81 (2002) 951-953

[209] M.J. de Boer, J.G.E. Gardeniers, H.V. Jansen, E. Smulders, M.J. Gilde, G. Roelofs, J.N. Sasserath, M. Elwenspoek, Guidelines for etching silicon MEMS structures using fluorine high-density plasmas at cryogenic temperatures, J. Microelectromech. Syst., 11 (2002) 385–401

[210] J. K. Bhardwaj, H. Ashraf, Advanced silicon etching using high density plasma, Proc. SPIE 2639 (1995) 224–233

[211] C. Yang, K. Leong, Influences of substrate wettability and liquid viscosity on isothermal spreading of liquid droplets on solid surfaces, Exp. Fluids 33 (2002) 728-731

[212] J.G. Korvink, O. Paul, MEMS: A Practical Guide to Design, Analysis, and Applications, Birkhauser, Basel, 2006, pp. 567-667

[213] M.N. Ozisik, Heat Conduction, John Wiley & Sons, New York, 1980, pp. 1-37

[214] ANSYS Inc, Modelling and Meshing Guides, ANSYS Inc., USA, 1998

[215] R. D. Birkhoff, L. R. Painter, J. M. Heller, Optical and dielectric functions of liquid glycerol from gas photoionization measurements, J. Chem. Phys. 69 (1978) 4185-4188

[216] J.C. Conde, P. Gonzalez, F. Lusquinos, S. Chiussi, J. Serra, B. Leon, Analytical and numerical calculations of the temperature distribution in Si and Ge targets irradiated by excimer lasers, Appl. Surf. Sci. 248 (2005) 455–460